

2  
MIX

NGR-16-002-029

Numerical calculation of flow fields about rectangular wings  
of finite thickness in supersonic flow

by

Jerald Milo Vogel

An Abstract of

A Dissertation Submitted to the  
Graduate Faculty in Partial Fulfillment of  
The Requirements for the Degree of  
DOCTOR OF PHILOSOPHY

Approved:

E. W. Anderson

John Henry  
In Charge of Major Work

R. B. Brown

A. E. Bengler  
For the Major Departments

Charlotte E. Rodenick  
For the Graduate College

Iowa State University  
Ames, Iowa

1973

(NASA-CR-130985) NUMERICAL CALCULATION OF  
FLOW FIELDS ABOUT RECTANGULAR WINGS OF  
FINITE THICKNESS IN SUPERSONIC FLOW  
Ph.D. (Iowa State Univ. of Science and  
Technology) 181 p HC \$11.25

N73-18269

CSCS 20D

G3/12

Unclas  
17175

Numerical calculation of flow fields about rectangular wings  
of finite thickness in supersonic flow

Jerald Milo Vogel

Under the supervision of Dr. E. W. Anderson  
From the Department of Aerospace Engineering and  
Dr. George Serovy from the Department of Mechanical Engineering  
Iowa State University

The inviscid flow fields about a three-dimensional rectangular wing of finite thickness at angle of attack with a subsonic tip in a supersonic flow are determined by applying a second order finite difference technique to the gas dynamic equations of motion in their conservative form. The analysis includes a comparison of the second order technique with a current third order method.

The principal objective of the study is to apply a current finite difference technique to the equations governing the supersonic flow past a wing to obtain the variation in the gas dynamic variables throughout the immediate flow field. The study is separated into two parts. The first part deals with the comparison of the second order MacCormack technique and the third order Rusanov technique. The second part is the actual implementation of the numerical method to obtain the flow field about a rectangular wing with a 7.5 degree half-angle double-wedge cross section and a double-cone tip at a Mach number of 2 at 0 and 4 degrees angle of attack.

The results obtained in the application of the MacCormack and

Rusanov techniques to the modified Burgers' equation and the gas dynamic equations governing the supersonic flow past a two-dimensional wedge indicate that the second order method by MacCormack is as good as Rusanov's technique in terms of flow field resolution and better in terms of computer storage requirements and run times.

The flow field about the rectangular wing is separated into three regions consisting of the forebody, the afterbody and the wing wake. Solutions for the forebody are obtained using conical flow techniques while the afterbody and the wing wake regions are treated as initial value problems. The numerical solutions are compared in the two-dimensional regions with known exact solutions.

Numerical calculation of flow fields about rectangular wings  
of finite thickness in supersonic flow

by

Jerald Milo Vogel

A Dissertation Submitted to the  
Graduate Faculty in Partial Fulfillment of  
The Requirements for the Degree of  
DOCTOR OF PHILOSOPHY

Majors: Aerospace Engineering  
Mechanical Engineering

Approved:

*B. W. Anderson*

*J. J. Jones*  
In Charge of Major Work

*R. R. Bussing*

*A. E. Boyles*  
For the Major Departments

*Charlotte E. Rodenbeck*  
For the Graduate College

Iowa State University  
Ames, Iowa

1973

## TABLE OF CONTENTS

	Page
NOMENCLATURE	v
INTRODUCTION	1
DIFFERENCING METHODS	5
Introduction	5
Accuracy	6
Stability Criteria	7
MacCormack Technique	11
Rusanov's Technique	13
SOLUTION OF THE MODIFIED BURGERS' EQUATION	16
Introduction	16
Stability Analysis	19
Numerical Solutions	20
TWO-DIMENSIONAL WEDGE FLOW FIELDS	32
Introduction	32
Steady Equations of Motion	34
Exact Solution	36
Wedge Coordinate System and Resulting Grid	36
Numerical Solution Technique	37
Numerical Solutions	42
THE RECTANGULAR CONE-TIPPED WING	49
Introduction	49
Equations of Motion	52
Numerical Technique	55
Stability Considerations	57

	Page
Region I Flow Field Analysis	58
Forebody geometry and coordinate systems	58
Forebody flow equations of motion	63
Evaluation of gas dynamic variables from conservative variables	64
Initial and boundary conditions	66
Choice of grid system	74
Solution technique	77
Forebody numerical solutions	79
Region II Flow Field Analysis	98
Afterbody geometry and coordinate systems	98
Afterbody equations of motion	101
Evaluation of the gas dynamic variables from conservative variables	102
Boundary conditions	103
Initial data	104
Choice of grid system	105
Solution technique	106
Afterbody numerical solutions	108
Region III Flow Field Analysis	138
Afterbody geometry, coordinate system and equations of motion	138
Initial and boundary conditions	138
Grid system and solution technique	139
Numerical solutions	141
RECOMMENDATIONS FOR FURTHER STUDY	147
REFERENCES	149
ACKNOWLEDGMENTS	152
APPENDIX A	153
Eigenvalue Evaluation for Cartesian System	153
Forebody Eigenvalues	155
Afterbody Eigenvalues	162

	Page
APPENDIX B - FLOW EQUATION TRANSFORMATIONS	166
Introduction	166
Forebody Equations of Motion	166
Afterbody Equations of Motion	170

## NOMENCLATURE

A, B, C	Coefficient matrices of the inviscid equations of motion in the Cartesian frame
A', B', C'	Coefficient matrices of the inviscid equations of motion in the $(\xi, \gamma, \phi)$ and $(\xi, \theta, \phi)$ frames
c	Speed of sound
$\bar{E}$	X-dependent conservative variables
$\bar{E}'$	$\xi$ -dependent conservative variables
$\bar{E}_0$	Constant
$\bar{F}$	Y-dependent conservative variables
$\bar{F}'$	$\gamma$ or $\theta$ -dependent conservative variables
$\bar{G}$	Z-dependent conservative variables
$\bar{G}'$	$\phi$ -dependent conservative variables
$\bar{H}, \bar{H}'$	Conservative variables
I	Unit matrix
i	Imaginary constant ( $\sqrt{-1.0}$ )
$\hat{i}_q$	Unit vector along streamline
$\hat{i}_r$	Unit vector in radial direction
j, k	Grid indices
$k_x$	Constant
M	Mach number
$\hat{n}$	Unit normal vector
p	Pressure
Q	Differential operator
q	Total velocity

t	Time
U	Vector of dependent variables
u, v, w	Velocity components in x, y and z directions
x, y, z	Independent variables in the Cartesian frame
$\alpha$	Angle of attack
$\beta$	Shock angle
$\gamma$	Ratio of specific heats
$\delta$	Stability parameter
$\lambda_j$	Eigenvalues
$\nu$	$\Delta t / \Delta x$ c
$(\xi, \gamma, \phi)$	Independent variables for body oriented coordinate systems
$(\xi, \theta, \phi)$	
$\rho$	Density

## Subscripts:

c	Corrected value or cone body conditions
j	Mesh point location in the y, $\gamma$ or $\theta$ directions
k	Mesh point location in the z or $\phi$ directions
max	Maximum
w	Conditions on the wedge
$\infty$	Free stream conditions

## Superscripts:

n	Time or x step location
---	-------------------------

## INTRODUCTION

The aerodynamic analysis of the flow fields about aircraft capable of operating in the supersonic regime for extended periods of time is a formidable task. The complex geometry of such vehicles in conjunction with the difficulty of solving the equations governing the aerodynamics preclude the possibility of obtaining exact solutions for the associated flow fields. These fundamental difficulties have prompted the development of numerous approximate methods for analyzing fluid flows. One of the most common of the simplifying assumptions used is that the flow may be separated into a viscous boundary layer flow and an outer inviscid flow which effectively determines the body pressure. This report is concerned with the calculation of the outer inviscid flow about a rectangular wing moving at supersonic speeds.

The inviscid equations of motion governing the flow generated by a wing moving at supersonic speeds form a set of hyperbolic differential equations. Since they are hyperbolic, the equations can be solved (at least conceptually) by techniques applicable to initial value problems. Up to the present only two such techniques which provide exact solutions have been applied to inviscid supersonic flow problems. The first technique involves the method of characteristics (1). This method has been successfully applied to numerous supersonic flow problems. Unfortunately, the application of this method is a complex task due to the geometric problems introduced by body shape, and difficulties in determining the

coordinate system or systems required and the inherent way in which a characteristics method works. The second method involves the use of shock-capturing finite difference approximations of the equations of motion and the solution of the resulting approximate equations at each grid or mesh point. This attack provides a solution for the inviscid flow throughout the flow field. The technique used advances the initial data through the fixed mesh, applying boundary conditions only at the body and in the free stream. Shock and expansion waves form and decay automatically without special treatments of any kind. On the other hand, the characteristics method utilizes logical numerical procedures to isolate shock waves and requires the application of the Rankine-Hugoniot shock relations across them to identify their strength and position.

The acceptance of the shock-capturing numerical techniques is becoming more universal as these techniques are improved. The early problems associated with the precise location of the shocks and the tendency of the techniques to produce spurious oscillations in the magnitudes of the dependent variables in the neighborhood of the shock are gradually being overcome. Numerical calculations of inviscid flows based upon the full Eulerian equations have been carried out for a variety of supersonic problems using several finite difference techniques. The techniques have generally been first, second and, more recently, third-order. Numerous authors have applied the Lax <sup>(1)</sup> first-order method to fluid flow problems. Notable among the results obtained by these investigators are the

solutions for the time dependent blunt body problems obtained by Bohachevsky and Mates<sup>(2)</sup> and Bohachevsky and Rubin<sup>(3)</sup> and the non-equilibrium gas dynamic calculations of DeJarnette<sup>(4)</sup>. While the Lax method provides reasonable results for very small mesh sizes, second-order methods are being used with increasing frequency. Kutler<sup>(5)</sup> has recently applied a version of the second-order Lax-Wendroff method developed by MacCormack<sup>(6)</sup> to study flow about sonic-edged, conical, wing-body combinations at angle of attack. Results of his work show excellent agreement with conical flow solutions calculated using other methods and with available experimental data. More recently, a third-order method developed simultaneously by Rusanov<sup>(7)</sup> and Burstein and Murin<sup>(8)</sup> gives improved shock and flow field resolution in certain cases.

This study is concerned with applications of the second-order MacCormack<sup>(6)</sup> technique and the more recently developed third-order Rusanov<sup>(7)</sup> technique to some simple nonlinear problems leading to solutions of the full Eulerian equations for flow about a rectangular wing moving supersonically. The material presented is separated into four major sections. The first section is an analysis of the differencing techniques under consideration as well as a discussion of the theoretical stability criterion based on amplification matrix theory. The second section is concerned with solutions of a one dimensional partial differential equation, the modified Burger's equation. Such solutions aid in understanding the MacCormack and Rusanov differencing techniques and their

application to nonlinear hyperbolic systems. The third section is concerned with the application of the two techniques to a more realistic flow problem, the supersonic two dimensional wedge flow field, in an attempt to determine the technique best suited for the rectangular wing problem. The fourth and final section presents the numerical solutions for the flow fields about and in the wake of a rectangular, not-so-thin wing in a supersonic flow field at angle of attack.

## DIFFERENCING METHODS

## Introduction

In recent years there has been an ever increasing use of finite difference methods in the reduction of continuous systems in order to obtain solutions to complex flow problems. The dominant influencing factor in the development of the numerical techniques has been the advent of the high-speed computing machinery required to process data at many points in a solution field.

To utilize a finite difference method one must first degenerate the continuous domain of interest to a discrete set of points generally termed the grid. The partial differential equations of motion governing the flow field are then differenced in some prescribed fashion. This results in a set of finite difference equations which must be solved at each point in the grid subject to certain boundary conditions applied at the edge of the grid.

Although the techniques appear to be elementary in nature and simple to apply one must be concerned with the accuracy, convergence and stability characteristics of the techniques. For the flow fields that contain shock waves one must be concerned with the ability of the finite difference technique to develop apparent discontinuities at the proper locations without producing excessive fluctuations in the magnitudes of the dependent variables near the discontinuities. In summary, improperly applied numerical methods may lead to extremely erroneous results.

Kutler<sup>(5)</sup> recently investigated a series of second-order finite difference techniques including Lax-Wendroff<sup>(9)</sup> methods and other somewhat similar methods developed by Leith<sup>(10)</sup>, Fromm<sup>(11)</sup>, Richtmeyer<sup>(12)</sup>, Burstein<sup>(13)</sup>, Strang<sup>(14)</sup>, Gourlay and Morris<sup>(15)</sup>, and MacCormack<sup>(6)</sup> as well as the classic first-order technique by Lax<sup>(1)</sup>. The results of the investigation indicate that in terms of ease of programming, storage space requirements, length of computing time and shock resolution and stability the method by MacCormack is superior and, as a result, is here to be considered for the study of the rectangular wing problem.

A second technique, developed by Rusanov<sup>(7)</sup> and Burstein and Murin<sup>(8)</sup>, will be considered to see if the more recently developed third order technique performs enough better so as to warrant its use in the rectangular wing solution.

The following three sections present brief discussions of accuracy, stability and the finite difference techniques under consideration.

#### Accuracy

In general the errors associated with finite difference solutions may be separated into two basic types. The first type of error is termed truncation error and is a measure of the degree to which the finite difference equations actually represent the continuous system of equations. Truncation error may be viewed in terms of a set of "modified partial differential equations" which

is the set of equations the finite difference formulation actually represents (see Ref. 16, p. 38). In this investigation the "modified equations" are studied for each differencing technique in the section of the report containing the technique descriptions.

The second type of error is termed round-off error which is sometimes referred to as computational error. Such errors are a result of the discrete equations being solved exactly only up to a certain number of digits depending upon the particular machine used to obtain the solution.

The grid point spacing effects both types of errors but in different fashions. That is, while decreasing the grid point spacing will generally decrease the truncation error, the resulting increase in required solution steps will tend to increase the computational errors. Hence, one cannot always increase accuracy by decreasing the mesh size.

#### Stability Criteria

One problem encountered in the application of finite difference schemes involves the numerical instabilities which result in error amplification. Unstable numerical schemes allow the growth of error to the extent that the true solution is "masked" yielding highly useless data. Hence, it is very desirable to have a means of predicting the parameters and their bounds which cause numerical schemes to result in instability.

The stability analysis used in this paper is that outlined by

Richtmeyer and Morton<sup>(17)</sup> which was also utilized by Kutler<sup>(5)</sup>. Four restrictive conditions must be applied in utilizing the technique. The governing equations must be locally linearized, the coefficients must be constant, the solution must be smooth and the boundary conditions must be ignored. Hence, the analysis is good only for regions removed from the boundaries and which are devoid of discontinuities. However, experience has shown that instabilities generally manifest themselves initially in the form of small amplitude, short wave length oscillations superimposed on a smooth solution in a narrow region of the solution field. Hence, the restrictions imposed by the stability theory may not be as prohibitive as they first appear.

Consider the system of partial differential equations in conservative form given by

$$\bar{E}_t + \bar{F}_x = 0 \quad (1)$$

where  $\bar{E}$  and  $\bar{F}$  are conservative variable vectors. This set of equations can be written in the form

$$\bar{E}_t + \bar{A} \bar{E}_x = 0 \quad (2)$$

where  $\bar{A}$  is a matrix containing the Jacobian elements of  $F$  with respect to  $E$ .

If the  $\bar{A}$  matrix is constant one may obtain the exact solution by means of the Fourier series method yielding

$$\bar{E} = \bar{E}_0 e^{-ik_x At} e^{ik_x x} \quad (3)$$

where  $\bar{E}_0$  is a constant vector and  $k_x$  is an arbitrary constant.

To apply the stability analysis to the numerical technique one introduces a row of errors along a  $t = \text{constant}$  line and observes the manner in which the differencing technique propagates the errors in time. The errors may be represented by a discrete Fourier series of the form

$$\sum_k \bar{E}_k e^{i\beta_k j\Delta x} \quad (4)$$

Usually, only the effects of one term ( $e^{i\beta j\Delta x}$ ) of the series is evaluated and a linear superposition process is utilized to evaluate the total error effects. If, for a fixed mesh, the error increases without bound as  $n\Delta t \rightarrow \infty$  the technique is termed stepwise unstable.

To illustrate the concept, consider the following difference scheme as applied to Equation (2):

$$\bar{E}_j^{n+1} = \bar{E}_j^n - \frac{\Delta t}{\Delta x} \frac{A}{2} (\bar{E}_{j+1}^n - \bar{E}_{j-1}^n) \quad (5)$$

with the boundary condition

$$\bar{E}_j^0 = e^{i\beta j\Delta x} \quad (6)$$

The use of a separation of variables technique leads to a solution of the form

$$\bar{E}_j^n = \bar{E}_1(n\Delta t) e^{i\beta j\Delta x} \quad (7)$$

Substitution of Equation (7) into the difference equations (5) yields

$$\bar{E}_j^{n+1} = \bar{E}_j^n \left[ I - \frac{\nu \bar{A}}{2} (e^{i\beta \Delta x} - e^{-i\beta \Delta x}) \right] = \bar{G} \bar{E}_j^n \quad (8)$$

where  $I$  is the identity matrix and  $\nu$  is the mesh ratio.

The matrix  $\bar{G}$  in Equation (8) is termed the amplification matrix and the solution, given by Lomax<sup>(8)</sup>, is

$$E_j^n = \sum_j \bar{c}_j (\lambda_j)^n \quad (9)$$

where  $n$  is an exponent and the  $\lambda_j$  represent the eigenvalues of the amplification matrix.

For the solution given by Equation (9) to remain bounded as  $n \rightarrow \infty$  the eigenvalues of  $\bar{G}$  must be less than or equal to unity. Hence, the stability criterion is given by

$$|\lambda_j| \leq 1 \quad (10)$$

To simplify the example under consideration assume that the set of conservative variables  $\bar{E}$  contains one member. Then the amplification matrix reduces to

$$G = 1 - \frac{\nu A}{2} (e^{i\beta \Delta x} - e^{-i\beta \Delta x}) \quad (11)$$

In view of Equations (10) and (11) the stability requirement is that

$$1 + \nu^2 A^2 \sin^2(\beta \Delta x) \leq 1 \quad (12)$$

It is noted here that the stability criterion yields stable values for the mesh ratio  $\nu$ . The results of Equation (12) indicate

that the difference scheme under consideration is unstable for any mesh ratio.

### MacCormack Technique

MacCormack has constructed a second order predictor-corrector sequence for use in solving systems of partial differential equations in conservative form. When applied to Equation (1), MacCormack's technique yields

$$\begin{aligned}\tilde{E}_j^{n+1} &= E_j^n - \frac{\Delta t}{\Delta x} [F_{j+1}^n - F_j^n] \\ E_j^{n+1} &= \frac{1}{2} \left[ E_j^n + \tilde{E}_j^{n+1} - \frac{\Delta t}{\Delta x} (\tilde{F}_j^{n+1} - \tilde{F}_{j-1}^{n+1}) \right]\end{aligned}\tag{13}$$

The tilde that appears over certain of the variables denotes the predicted value of that particular variable.

To investigate the accuracy of the technique the modified partial differential equation is developed for a system of the form given by Equation (2) with  $A = c = \text{constant}$  and  $E = u$  which is the linear wave equation.

$$u_t + cu_x = 0\tag{14}$$

The resulting difference equations reduce to

$$\begin{aligned}\tilde{u}_j^{n+1} &= u_j^n - \nu (u_{j+1}^n - u_j^n) \\ u_j^{n+1} &= \frac{1}{2} \left[ u_j^n + \tilde{u}_j^{n+1} - \nu (\tilde{u}_j^{n+1} - \tilde{u}_{j-1}^{n+1}) \right]\end{aligned}\tag{15}$$

The modified equation, which is the equation actually represented by Equation (13), is of the form

$$u_t + cu_x = Qu \quad (16)$$

where  $Q$  is some differential operator. To evaluate  $Q$  one first combines the predictor and corrector equations yielding

$$u_j^{n+1} = (1-\nu^2)u_j^n + \frac{\nu(\nu-1)}{2}u_{j+1}^n + \frac{\nu(\nu+1)}{2}u_{j-1}^n \quad (17)$$

Each term is then expanded in a Taylor series about the point  $(n\Delta t, j\Delta x)$ . Partial derivatives with respect to time that are second order and higher are eliminated using Equation (16). For MacCormack's technique Equation (14) reduces to

$$u_t + cu_x = -c\frac{\Delta x^2}{6}(1-\nu^2)u_{xxx} - \frac{c\Delta x^3}{8}(\nu-\nu^3)u_{xxxx} + \dots \quad (18)$$

The  $Qu$  term is represented by the right side of Equation (18).

It is noted that to second order the modified equation is exactly the linear wave equation as it should be since the technique is second order. The lowest order dispersive error and dissipative error is given by the first and second terms respectively on the right side of Equation (18).

An interesting point to observe is that when  $\nu = \pm 1$  the error terms in Equation (18) all become zero resulting in an exact solution. This condition is referred to as the "shift condition" by Kutler and Lomax<sup>(19)</sup> who have shown that satisfying this condition as best possible in the nonlinear case generally yields good shock

capturing characteristics.

The limits on  $\nu$  for which the computational errors do not grow in an unbounded fashion may be determined by means of the previously discussed amplification matrix theory. For the linear wave equation the amplification matrix, which has but one element, is given by

$$G = 1 - \nu^2 + \nu^2 \cos(\beta \Delta x) - i\nu \sin(\beta \Delta x) \quad (19)$$

If the magnitude of the amplification factor,  $G$ , is not to exceed unity then  $\nu$ , commonly termed the Courant number, must not be permitted to exceed unity. Hence, the stability bound on the mesh size is given by

$$\nu = c \frac{\Delta t}{\Delta x} \leq 1 \quad (20)$$

In view of Equation (18) the shift condition is the maximum stable Courant number.

#### Rusanov's Technique

Recent improvements in high-speed computers has resulted in increased interest in higher order differencing methods to improve flow field resolution. One of the more recent is a third-order method developed simultaneously by Rusanov<sup>(7)</sup> and Burstein and Murin<sup>(8)</sup>. This technique, based on the Runge-Kutta method, utilizes a three-level predictor-corrector sequence which, when applied to Equation (1), is given by

$$\begin{aligned}
E_{j+\frac{1}{2}}^{(1)} &= \frac{1}{2} (E_{j+1}^n + E_j^n) - \frac{1}{3} \frac{\Delta t}{\Delta x} (F_{j+1}^n - F_j^n) \\
E_j^{(2)} &= E_j^n - \frac{2}{3} \frac{\Delta t}{\Delta x} (F_{j+1}^{(1)} - F_{j-\frac{1}{2}}^{(1)}) \\
E_j^{n+1} &= E_j^n - \frac{1}{24} \frac{\Delta t}{\Delta x} \left[ -2F_{j+2}^n + 7(F_{j+1}^n - F_{j-1}^n) + 2F_{j-2}^n \right] \\
&\quad - \frac{3}{8} \frac{\Delta t}{\Delta x} (F_{j+1}^{(2)} - F_{j-1}^{(2)}) \\
&\quad - \frac{\delta}{24} \left[ E_{j+2}^n - 4(E_{j+1}^n + E_{j-1}^n) + 6E_j^n + E_{j-2}^n \right]
\end{aligned} \tag{21}$$

The last term in the third level equation is a stabilizing term without which the system would be unconditionally unstable for all values of  $\nu$ .

Application of Rusanov's technique to the linear wave equation given by Equation (13) yields the following modified partial differential equation:

$$\begin{aligned}
u_t + cu_x &= -c \frac{\Delta x^3}{24} \left( \frac{\delta}{\nu} - 4\nu + \nu^3 \right) u_{xxxx} \\
&\quad - c \frac{\Delta x^4}{120} (5\delta - 4 - 15\nu^2 + 4\nu^4) u_{xxxxx} + \dots + \dots
\end{aligned} \tag{22}$$

It is readily apparent from the modified equation that to third order the linear wave equation is solved exactly as could be expected since Rusanov's technique is third-order. The lowest order error term which contains the fourth derivative is dissipative in nature with the next higher order term being dispersive. It is also noted that for  $\delta = 3$  and  $\nu = 1$  the error terms shown on the right

side of Equation (21) vanish. Kutler and Lomax<sup>(19)</sup> have shown that under these conditions the shift condition is satisfied yielding an exact solution.

In so far as stability is concerned Rusanov<sup>(7)</sup> has shown that the stability criteria are given by

$$\begin{aligned} \nu &= c \frac{\Delta t}{\Delta x} \leq 1 \\ 4\nu^2 - \nu^4 &\leq \delta \leq 3 \end{aligned} \tag{23}$$

which indicates that the shift condition also satisfies the stability requirement. It would appear that when one operates at mesh ratios less than unity the value of  $\delta$  should be set to most nearly satisfy the shift condition, which is a difficult requirement to meet.

## SOLUTION OF THE MODIFIED BURGERS' EQUATION

## Introduction

A major problem encountered in the application of finite difference techniques is the effect of eigenvalue variation throughout the flow field. Stability analyses have shown that eigenvalue magnitudes determine stability bounds which ultimately dictate acceptable grid mesh ratios. In addition, the modified partial differential equations are used to predict the best grid mesh ratios from an accuracy viewpoint. From previous work it has been noted that for best results one should operate as closely as possible to the upper stability bound corresponding to a Courant number of unity. Utilizing a fixed coordinate system in which the mesh ratios are constant to determine a flow field in which the eigenvalues are non-constant precludes the possibility of operating at the best Courant number throughout the flow field. Hence, it is quite desirable to use a finite difference technique capable of good flow field resolution through a wide range of Courant numbers.

An investigation of the two numerical techniques under consideration is presented in this section in an attempt to evaluate their behavior when applied using a variety of off-design Courant numbers. Particular attention is given to the spreading of discontinuities and oscillations of the solution near points of rapid change of the dependent variables.

The hyperbolic form of the equation introduced by J. M. Burgers

is a valuable aid in studying the ability of a given numerical method to produce a solution to a nonlinear equation<sup>(20)</sup>. The modified Burger's equation in conservative form is given by

$$\frac{\partial u}{\partial t} + \frac{\partial}{\partial x} \left( \frac{u^2}{2} \right) = 0 \quad (24)$$

Kutler has successfully used this equation as an analog of the inviscid Euler equations and studied the solutions produced by various first- and second-order methods<sup>(5)</sup>. Shocks and rarefactions which occur in the gas-dynamic solutions were simulated by introducing discontinuities in the initial data.

A similar procedure is followed in this section to compare MacCormack's technique, which Kutler found to be a superior second-order method, with the more recent third-order technique developed by Rusanov. In order to accomplish this, two discontinuities of different magnitudes are introduced in the initial data simulating shocks of different strengths with different propagation rates.

In particular, the problem is to determine the solution of the modified Burger's equation subject to the initial conditions shown in Figure 1 which are

$$\begin{aligned} u &= 0 & x &\geq x_2 \\ u &= u_2 & x_2 &> x > x_1 \\ u &= u_1 & x &\leq x_1 \end{aligned} \quad (25)$$

where

$$u_1 > u_2$$

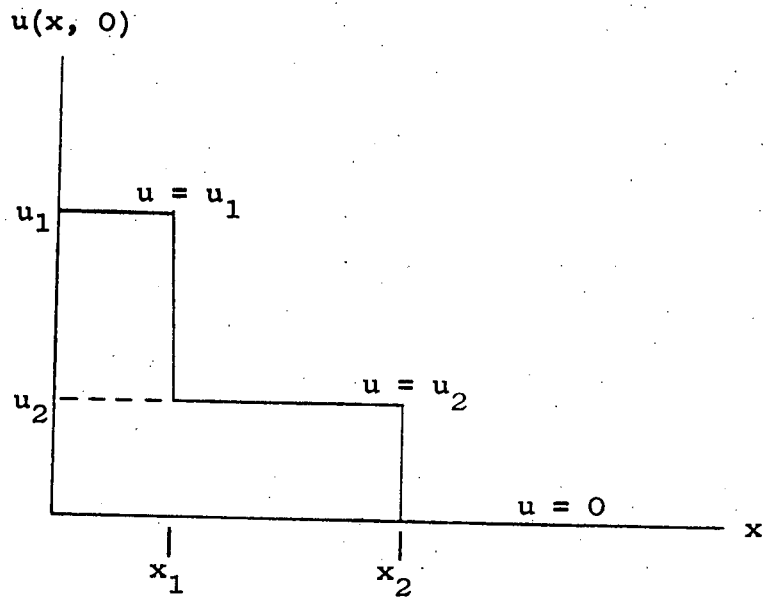


Figure 1. Initial conditions for Burger's equation

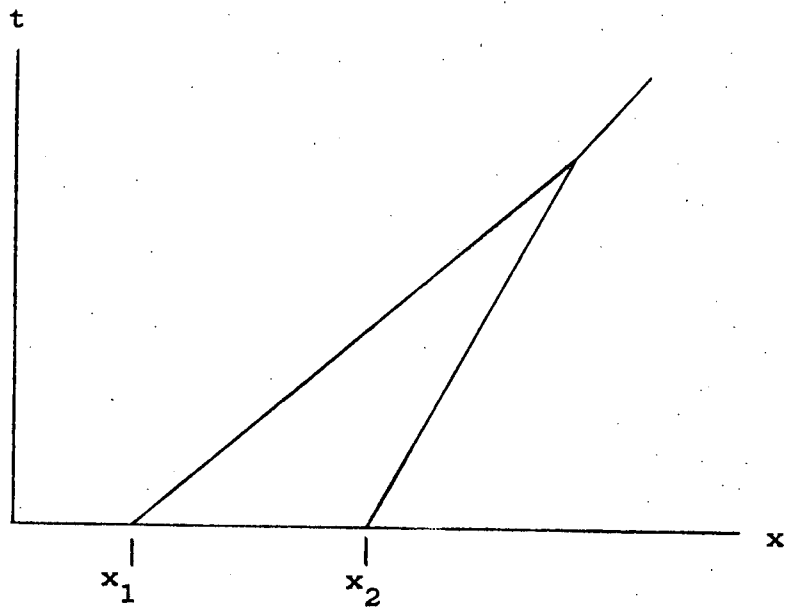


Figure 2. Space-time solution for overtaking discontinuities

Since this problem represents the intersection of two discontinuities, the exact solution is presented in two regions. The first region is prior to the intersection of the discontinuities and the second is after the intersection (Figure 2). The exact solutions in these regions are

$$\begin{array}{ll}
 \text{Region 1} & \\
 u(x, t) = 0 & \frac{x - x_2}{t} > \frac{u_2}{2} \\
 u(x, t) = u_2 & x_1 + \frac{u_1 + u_2}{2} t \leq x \leq x_2 + \frac{u_2 t}{2} \\
 u(x, t) = u_1 & \frac{x - x_1}{t} < \frac{u_1 + u_2}{2}
 \end{array} \tag{26}$$

$$\begin{array}{ll}
 \text{Region 2} & \\
 u(x, t) = 0 & \frac{x}{t} > \frac{u_1}{2} \\
 u(x, t) = u_1 & \frac{x}{t} \leq \frac{u_1}{2}
 \end{array}$$

### Stability Analysis

Next a stability analysis based on amplification matrix theory is performed on Equation (24) to determine the bounds on the mesh ratio  $\Delta t / \Delta x$  for which the numerical techniques are stable.

Equation (24) can be written in the form of Equation (2) with  $E = u$  and  $A = u$  yielding an expression in the form

$$u_t + u u_x = 0 \tag{27}$$

which is similar to the linear wave equation with the wave speed equal to the quantity  $u$ .

In view of Equations (20) and (23) the stable range of mesh ratios for both the MacCormack and Rusanov methods is given by

$$u \frac{\Delta t}{\Delta x} \leq 1 \quad (28)$$

For those points in the solution field where  $\Delta t/\Delta x$  numerically exceeds the reciprocal of  $u$  one can expect an instability to exist. Numerical solutions are usually obtained by using fixed intervals in time and space ( $\Delta t$ ,  $\Delta x$ ). Hence, one must search the field to determine the maximum of the eigenvalue,  $u$ , for this value will determine the largest stable  $\Delta t/\Delta x$ . That is, for stable solutions using a fixed mesh ratio the stability criterion is given by

$$\frac{\Delta t}{\Delta x} \leq \frac{1}{u_{\max}} \quad (29)$$

It is noted here that in more complex problems the maximum eigenvalues cannot always be determined until the numerical process is under way. Hence, it is not an unusual procedure to change the mesh ratios as the numerical process continues.

#### Numerical Solutions

Two double-shock geometries were considered for each numerical technique. In one case  $u_2 = 3$  and  $u_1 = 5$  whereas in the other case  $u_2 = 1$  and  $u_1 = 5$ . They are termed the 5-3-0 and the 5-1-0 problems respectively. In both cases the discontinuities, called

waves, were located at  $x_2 = 15$  and  $x_1 = 36$  and were contained within one interval. A total of 100 intervals was used in the  $x$  direction with the interval size  $\Delta x$  equal to unity.

The integrations in time were allowed to proceed for a total of 60 steps, a sufficient time interval to allow the faster moving wave to overtake the slower. The time interval for the integration was chosen to be the maximum allowable consistent with the criterion given in Equation (28). Under these circumstances the large amplitude wave is always being computed at the maximum Courant number which, according to the linear analysis, should yield the best possible solution. For the 5-3-0 and 5-1-0 cases the smaller amplitude waves are being computed at suboptimal Courant numbers of 0.6 and 0.2 respectively.

The dependent variable is held constant at both ends of the spatial grid which provides boundary conditions for the system. The integration is terminated well before the waves intersect the boundary.

The 5-3-0 double-shock problem is solved first. Figures 3, 4 and 5 represent solutions using Rusanov's technique with a Courant number of unity and a stability parameter,  $\delta$ , of 3, 2 and 1 respectively. Figure 6 represents a solution using the MacCormack technique with a Courant number of unity. Figure 3 indicates that at  $\nu = 1$  and  $\delta = 3$  a stable solution exists throughout the field. The large amplitude wave is being computed at the optimum conditions while the small amplitude wave is being computed at a

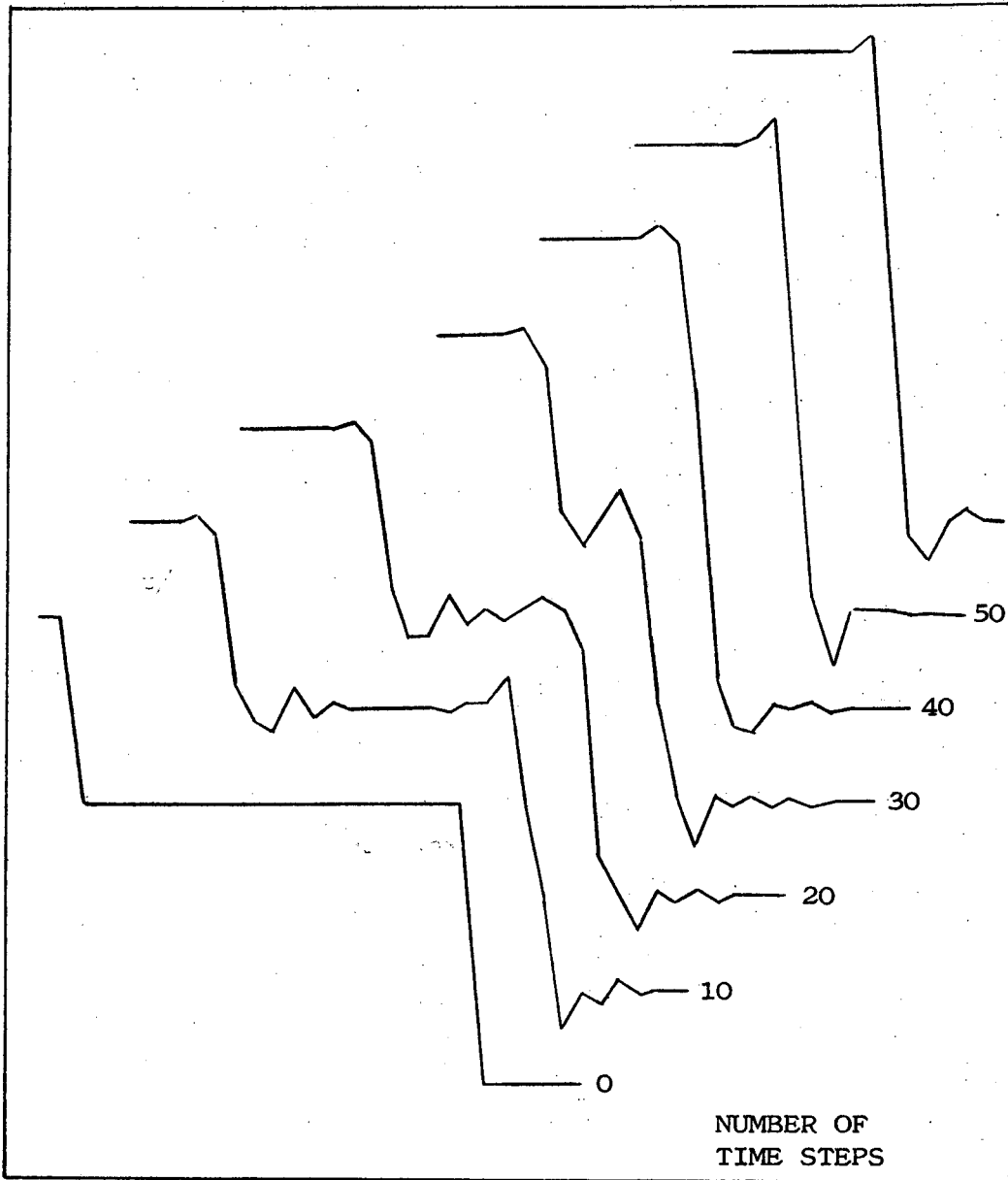


Figure 3. Burger's equation solution, Rusanov technique.  
5-3-0 case for  $\delta = 3.0$  and Courant number = 1

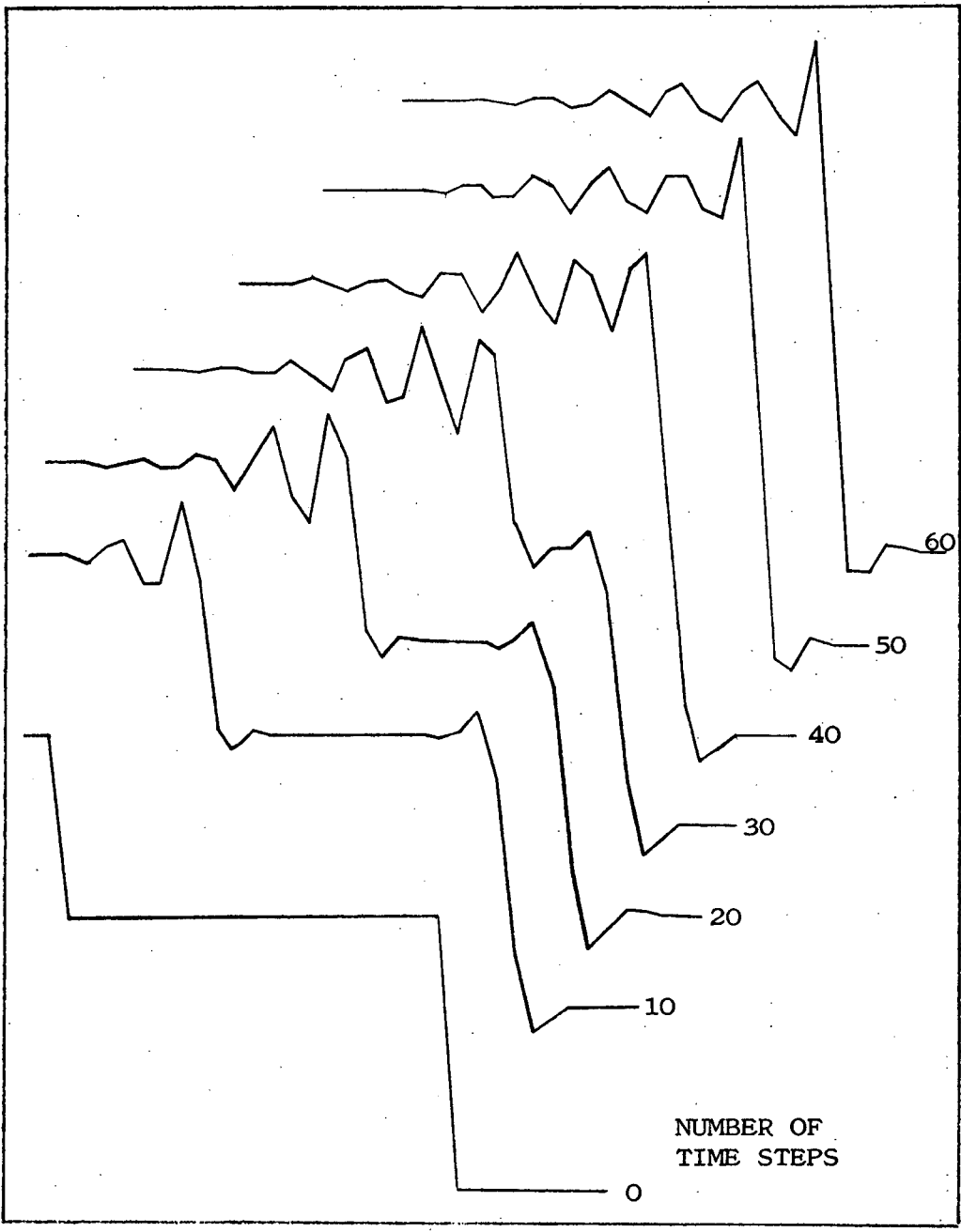


Figure 4. Burger's equation solution, Rusanov technique. 5-3-0 case for  $\delta = 2.0$  and Courant number = 1

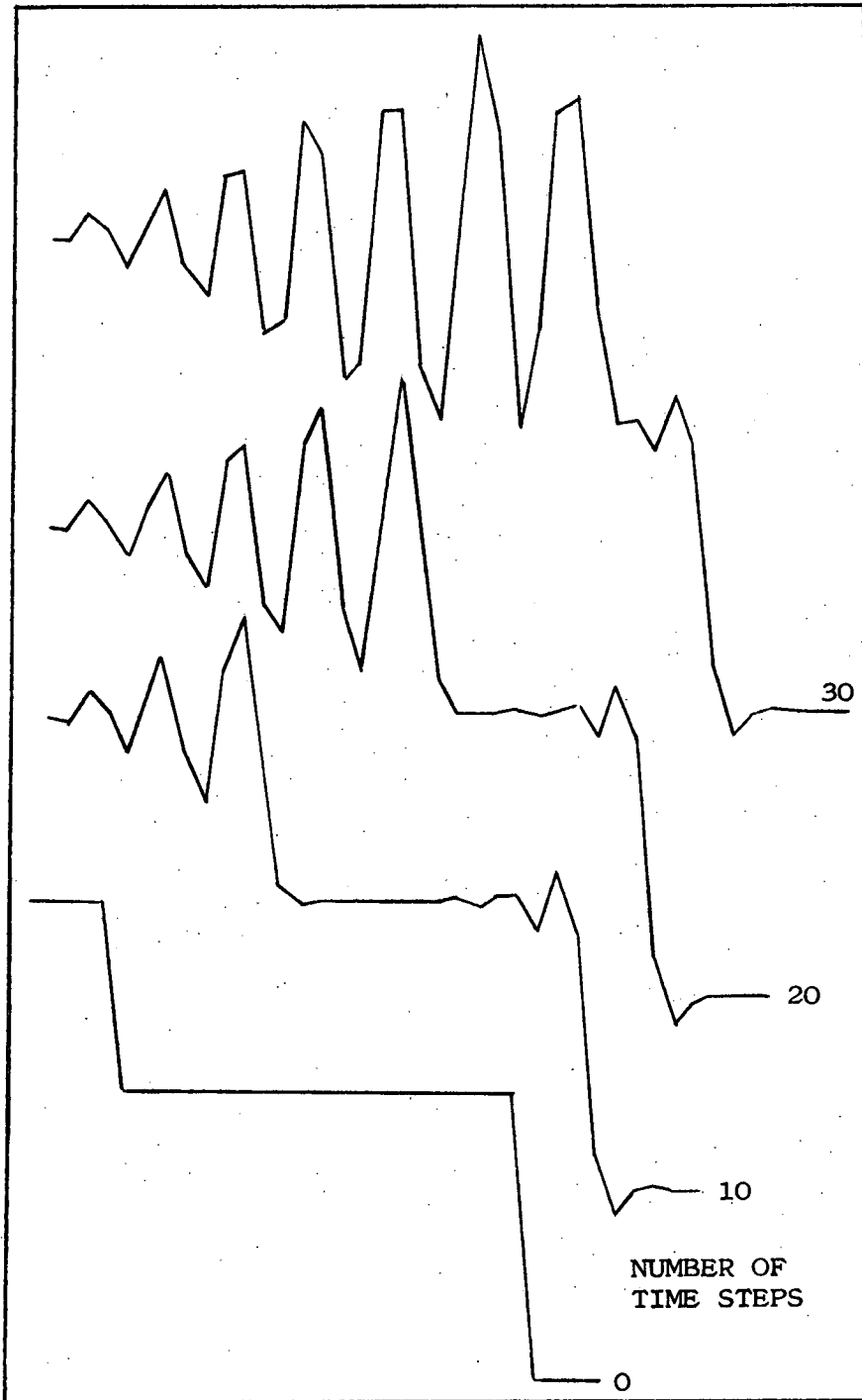


Figure 5. Burger's equation solution, Rusanov technique.  
5-3-0 case for  $\delta = 1.0$  and Courant number = 1

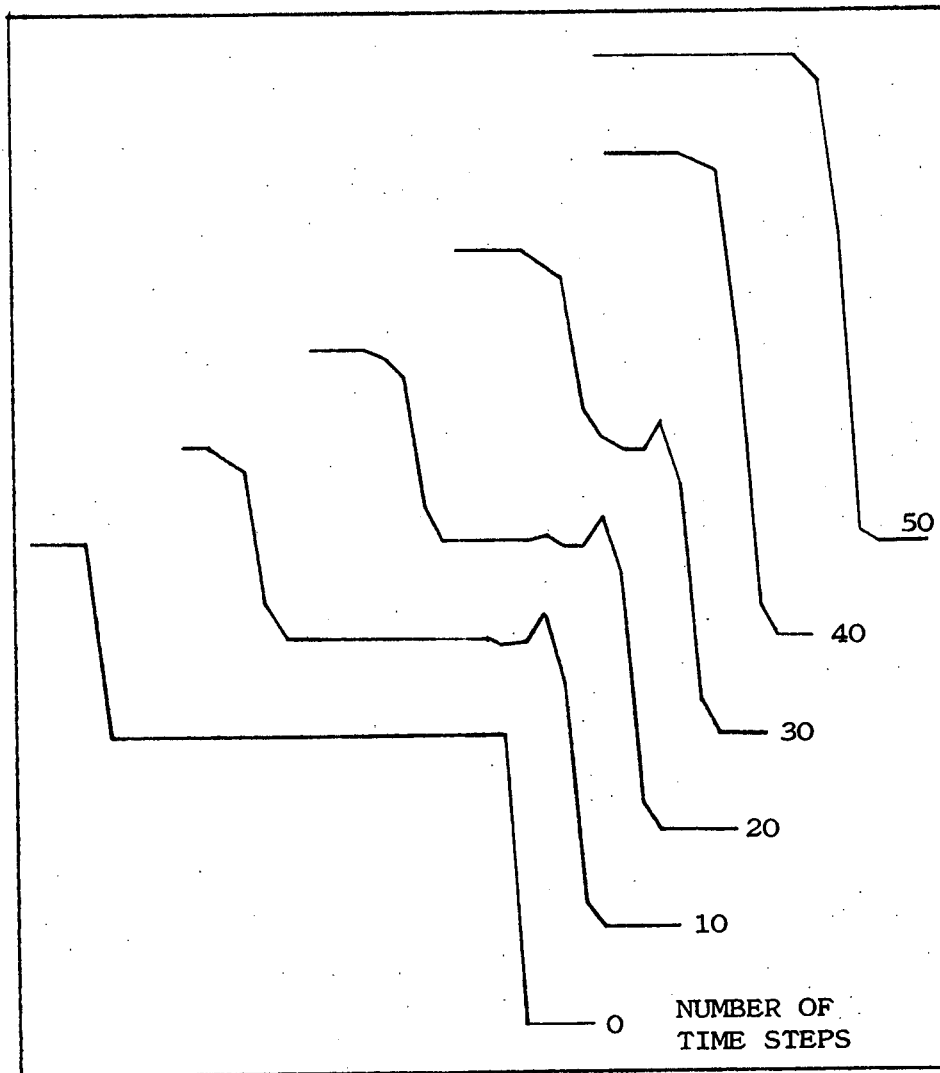


Figure 6. Burger's equation solution, MacCormack technique.  
5-3-0 case for Courant number = 1

suboptimal Courant number of 0.6. The magnitude of the stability parameter,  $\delta$ , falls within the stable range throughout the field. As predicted, the large wave resolution is very good with few oscillations occurring at the discontinuity and, at the same time, the discontinuity is confined to one interval. The smaller amplitude wave, however, is not as well behaved. The off-design Courant number at this point in the solution field causes undesirable oscillations to occur at the discontinuity as a result of the dispersive terms in the modified equation. The spreading of the discontinuity caused by the dissipative terms in the modified equation is not extremely significant at this Courant number since the discontinuity remains captured in essentially one interval. Figure 4 shows the results for  $\nu = 1$  and  $\delta = 2$ . For the large wave  $\delta$  is in the unstable range according to the linear theory. Although it appears that the actual numerical solution is stable an excessive number of large amplitude oscillations occur yielding a highly undesirable solution. For the lower amplitude wave the  $\delta$  value is in the stable range. The oscillations at the discontinuity are fewer than the previous solution indicating that perhaps the stability parameter should be set at less than the maximum value for the best results at off-design Courant numbers. In both cases the discontinuities remain isolated between essentially two grid points. Figure 5 indicates a solution for which  $\nu = 1$  and  $\delta = 1$ . For the large amplitude wave the value of  $\delta$  is far outside the stability range and, as a result, an instability occurs at this point in the solution

field. For the small amplitude wave the  $\delta$  parameter is slightly outside the linear stability range yielding a solution with excessive oscillations but apparently marginally stable. Figure 6 shows the MacCormack solution at a Courant number of 1.0 for the large wave and a Courant number of 0.6 for the small wave. Essentially no oscillations occur at the large wave while even at the off-design Courant number very few oscillations occur at the small wave. Both discontinuities remain isolated between two grid points.

Figures 7, 8 and 9 represent a Rusanov solution to the 5-1-0 problem with  $\nu = 1$  and for values of  $\delta$  of 3, 2 and 1 respectively. The same general trends occur with the addition of substantial amounts of discontinuity spreading at the lower wave which is being computed at a Courant number of 0.2. Figure 10 shows the MacCormack solution which contains, overall, fewer oscillation problems and a lesser amount of discontinuity spreading.

On the basis of the information obtained from the solution of Burger's equation it appears that it is desirable to use the MacCormack technique rather than the Rusanov technique. Shock resolution and over- and under-shoot characteristics are better over the range of eigenvalues considered. At the lower Courant numbers the shock spreading with the MacCormack technique appears to be less severe than that resulting from the use of the Rusanov technique. In addition, the computer storage and computation time requirements are significantly lower for the MacCormack technique.

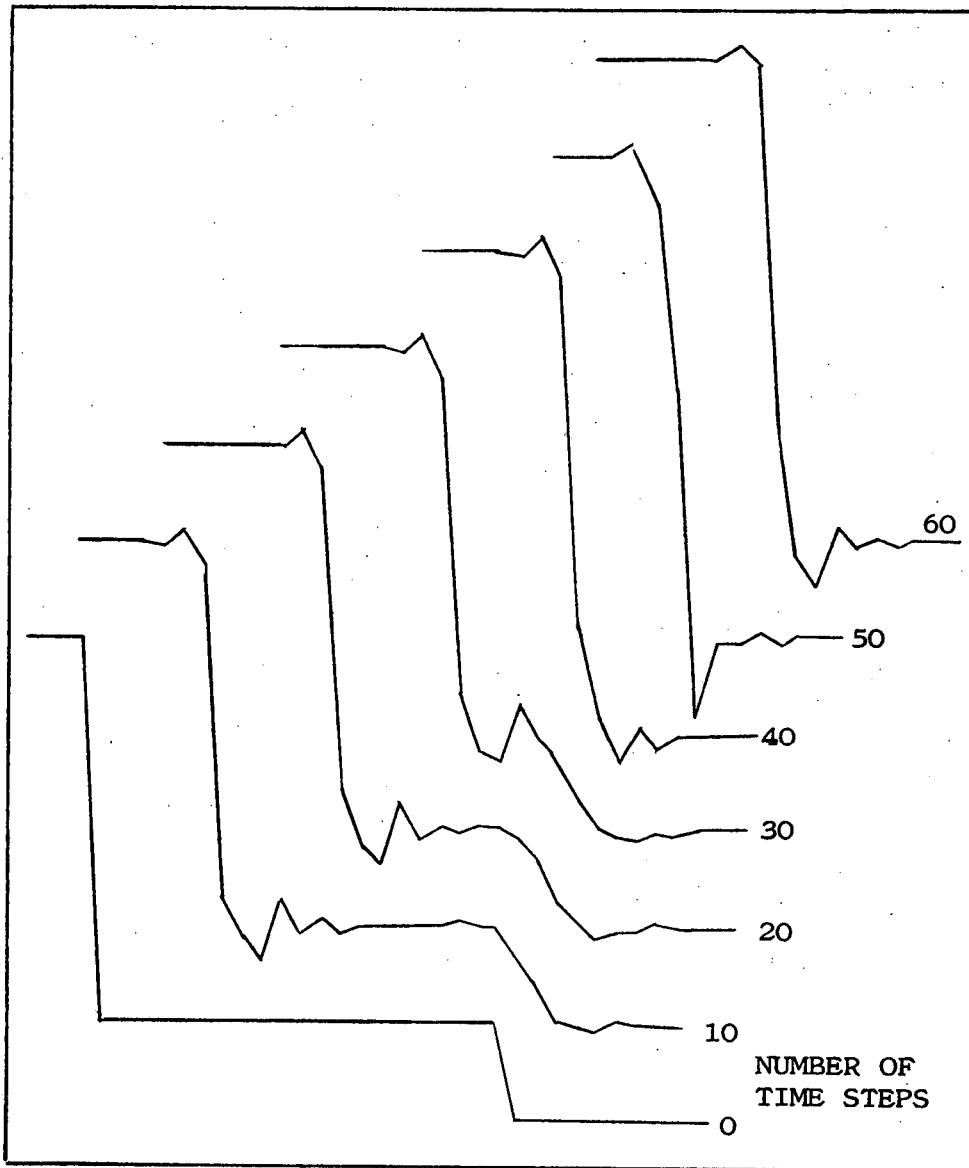


Figure 7. Burger's equation solution, Rusanov technique.  
5-1-0 case for  $\delta = 3.0$  and Courant number = 1

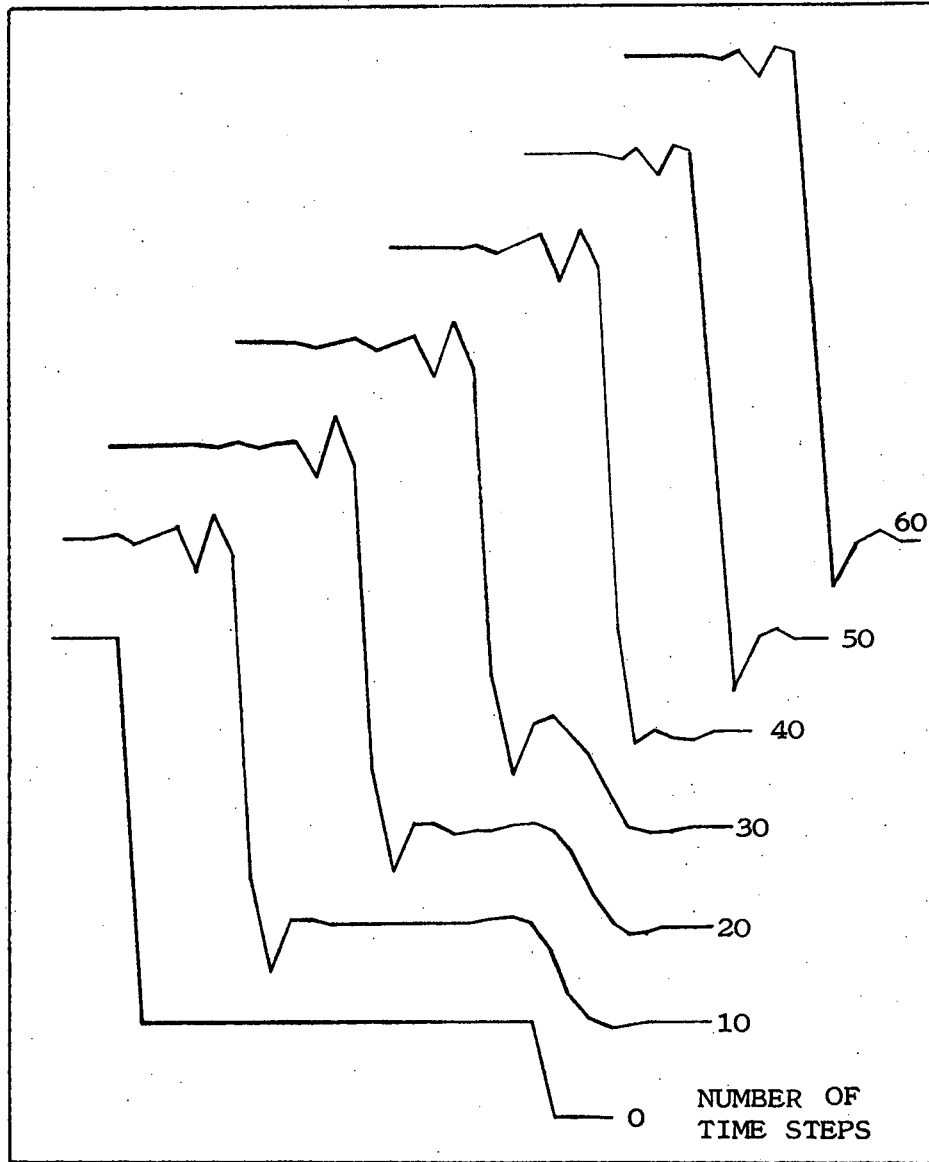


Figure 8. Burger's equation solution, Rusanov technique.  
5-1-0 case for  $\delta = 2.0$  and Courant number = 1

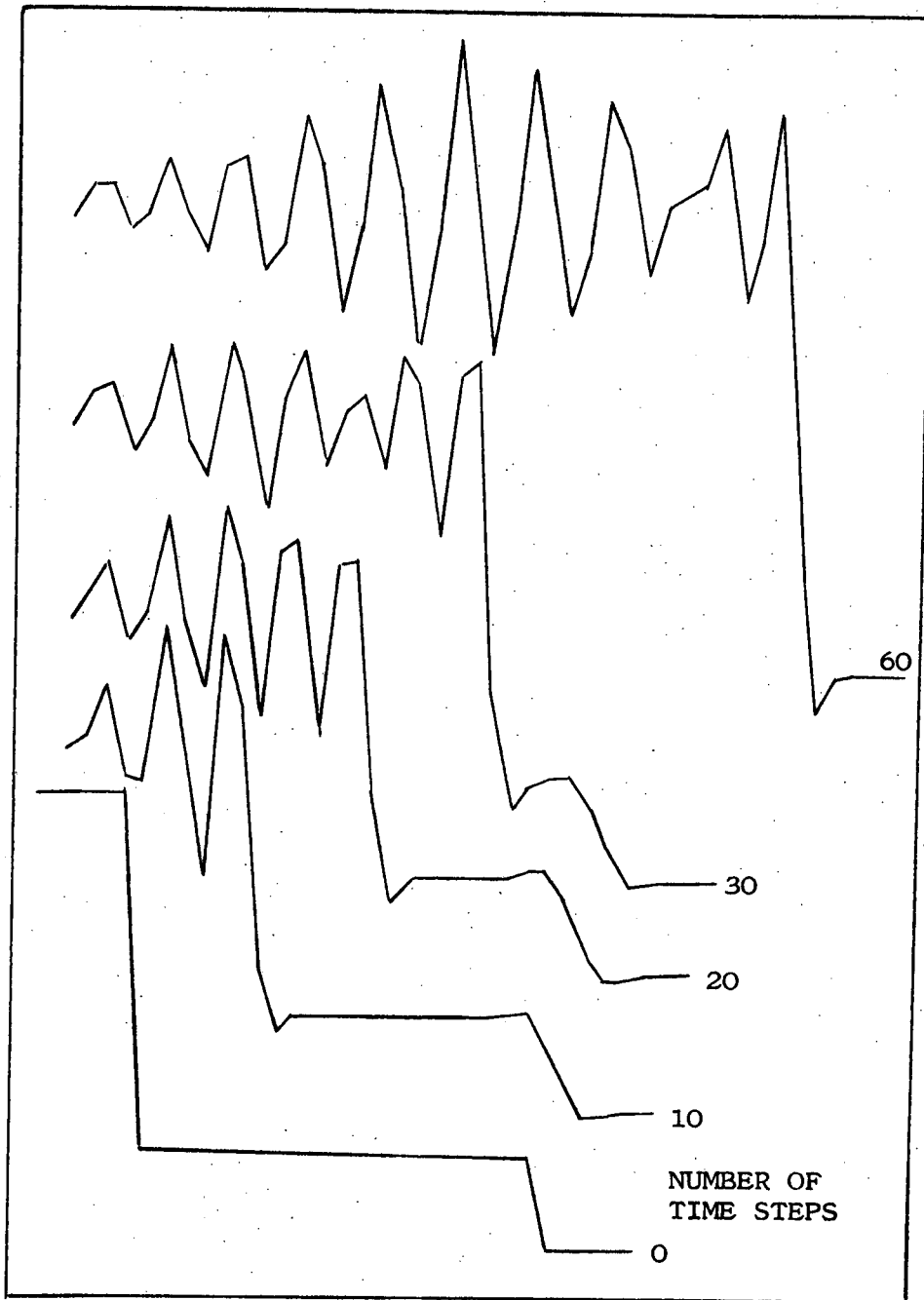


Figure 9. Burger's equation solution, Rusanov technique.  
5-1-0 case for  $\delta = 1.0$  and Courant number = 1

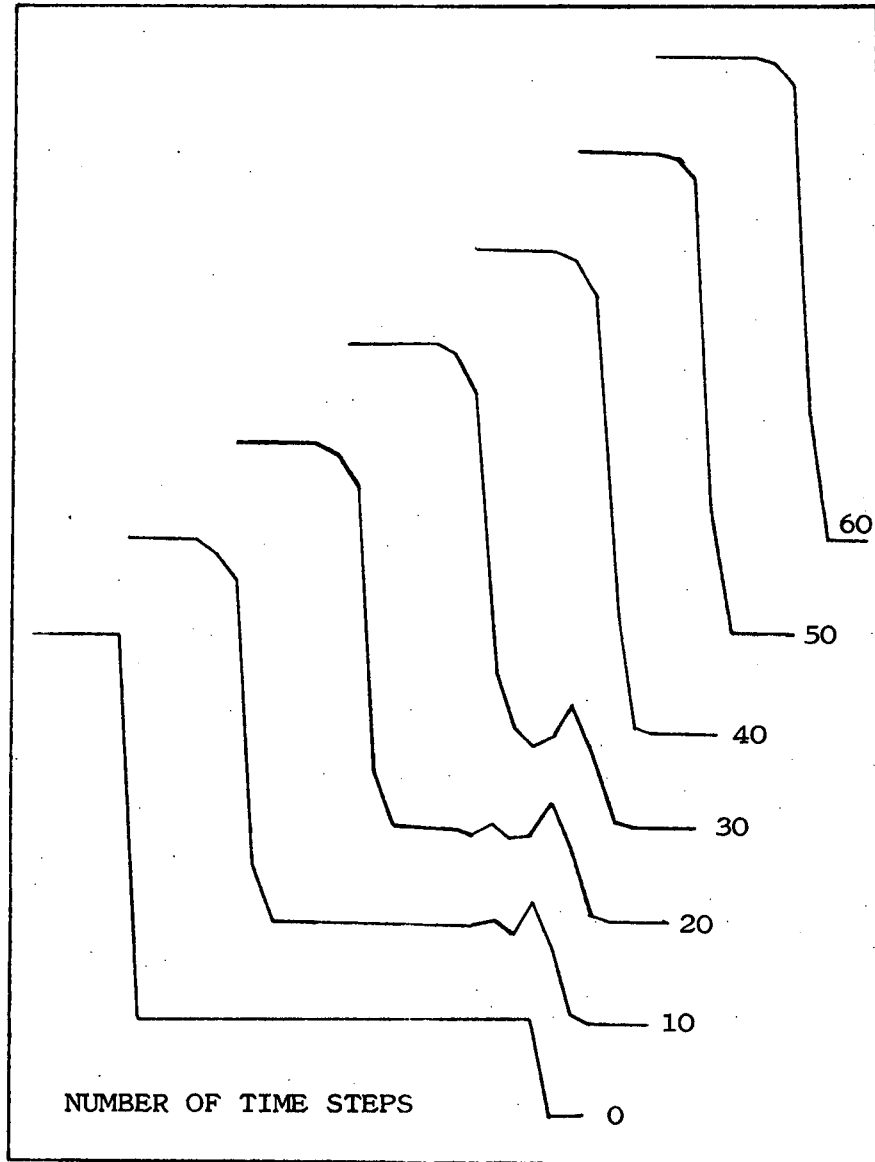


Figure 10. Burger's equation solution, MacCormack technique.  
5-1-0 case for Courant number = 1

## TWO-DIMENSIONAL WEDGE FLOW FIELDS

## Introduction

To further develop the comparison between the numerical techniques under consideration a study of the two-dimensional wedge in supersonic flow is undertaken. The equations of motion governing the flow about a two-dimensional wedge with the same half-angle as is encountered at the leading edge of the three-dimensional rectangular wing are solved at a Mach number of 2 using both numerical techniques. Then a comparison with available exact solutions is made to evaluate the performance of the techniques. Of particular interest is the capability of the techniques to develop crisp shocks in the proper locations as well as minimize the number of oscillations of the dependent variables in the neighborhood of the shock.

Three different approaches may be used to obtain a numerical solution of the wedge equations of motion.

In the first approach the complete unsteady equations of motion are integrated subject to boundary conditions dictated by the wedge geometry. Since the equations are hyperbolic in the time variable, the problem generated is of the initial value type. The integration of these equations in time proceeds from an appropriate set of initial data and is terminated once the flow variables reach a steady state condition.

The second approach is one used by Kutler<sup>(5)</sup>. The full-blown equations of motion are reduced to a set of steady equations by

setting all time derivatives equal to zero which would be the situation in the case of the steady state solution. The resulting equations are hyperbolic with respect to the x-coordinate (the coordinate most nearly aligned with the flow direction) as long as the x-component of velocity remains locally supersonic. Again, the system reduces to an initial value problem and can be integrated in the x-direction starting from an appropriate set of initial data and subject to boundary conditions dictated by the wedge geometry. Since the flow is conical in nature the flow variables in the solution are constant along rays from the origin, a condition which serves as the convergence criterion in the numerical process. It is readily apparent that the x-coordinate in the steady equations is quite analagous to the time coordinate in the set of time dependent equations.

The third approach is one that has been used by Anderson and Vogel<sup>(21)</sup>. The full-blown equations of motion are transformed from a Cartesian coordinate system to a polar coordinate system in which one of the coordinates ( $r$ ) is the distance along a ray from the origin. Again, the set of equations is hyperbolic in time. Since the flow is conical, the steady state values of the  $r$  derivatives are initially set equal to zero yielding a simple set of hyperbolic equations containing one less independent variable than in the case of the full-blown set. The equations are integrated in time starting from an appropriate set of initial data. The solution is realized when the dependent variables no longer change

with time.

In general, approaches 2 and 3 require less computer storage and computation time than is the case in approach 1, since the equations of motion contain one less independent variable than those of approach 1. However, approach 1 is probably more versatile since it is not dependent upon the conical flow requirement.

Approach 2 is adopted for the investigation undertaken in this paper. The numerical solutions for the two-dimensional wedge as well as the leading edge of the rectangular wing are obtained through numerical integration of the steady equations.

#### Steady Equations of Motion

The two-dimensional wedge flow equations of motion in a Cartesian body-oriented coordinate system for a steady, inviscid, nonheat-conducting and adiabatic flow are given by<sup>(5)</sup>.

$$\begin{aligned} \frac{\partial(\rho u)}{\partial x} + \frac{\partial(\rho v)}{\partial y} &= 0 \\ \frac{\partial(p + \rho u^2)}{\partial x} + \frac{\partial(\rho uv)}{\partial y} &= 0 \\ \frac{\partial(\rho uv)}{\partial x} + \frac{\partial(p + \rho v^2)}{\partial y} &= 0 \\ p &= \frac{\rho}{\gamma} \left[ 1 + \frac{\gamma-1}{2} (u^2 + v^2) \right] \end{aligned} \tag{30}$$

These equations are the continuity equation, x- and y-direction momentum equations and the integrated form of the energy equation which is usually referred to as Bernoulli's equation. The dependent

variables ( $\rho$ ,  $u$ ,  $v$ ,  $p$ ) in the equations are in a dimensionless form. The nondimensionalizing parameters for the pressure, density and the velocity components are gamma times the free stream stagnation pressure, the stagnation density and the stagnation speed of sound respectively.

Three partial differential equations of motion are in the conservative form

$$\frac{\partial \bar{E}}{\partial x} + \frac{\partial \bar{F}}{\partial y} = 0 \quad (31)$$

where  $\bar{E}$  is a vector whose elements are conservative variables given by

$$\bar{E} = \left\{ \begin{array}{l} \rho u \\ p + \rho u^2 \\ \rho uv \end{array} \right\} \quad (32)$$

and  $\bar{F}$  is a vector whose elements are conservative variables given by

$$\bar{F} = \left\{ \begin{array}{l} \rho v \\ \rho uv \\ p + \rho v^2 \end{array} \right\} \quad (33)$$

## Exact Solution

The exact solution to the two-dimensional supersonic wedge is clearly presented in the text written by Liepmann and Roshko<sup>(22)</sup>.

The flow field over the wedge surface behind the shock is uniform and is in the direction of the wedge surface. The wedge surface pressure is given by

$$\frac{P_w - P_\infty}{P_\infty} = \frac{2\gamma}{\gamma+1} (M_\infty^2 \sin^2 \beta - 1) \quad (34)$$

and the shock angle can be determined using the equation

$$\tan \theta = 2 \cot \beta \frac{M_\infty^2 \sin^2 \beta - 1}{M_\infty^2 (\gamma + \cos^2 \beta) + 2} \quad (35)$$

Two values of shock angle ( $\beta$ ) satisfy the equation. The smallest value, the proper solution, represents the weak solution for attached shocks.

## Wedge Coordinate System and Resulting Grid

The Cartesian coordinate system used for the wedge flow field analysis is aligned such that the x-axis is in the direction of the wedge surface with the y-axis normal to the surface. Hence, the wedge surface is a constant-coordinate surface, a highly desirable situation with regard to boundary conditions. Application of boundary conditions for body surfaces in nonaligned coordinate systems can be extremely difficult and, at times, may present stability problems.

The grid system for the numerical techniques generated by the coordinate system is shown in Figure 11. Since only the upper surface flow field is to be considered the lower wedge surface can be ignored. The existence of the sublayer is a result of the application of boundary conditions and is discussed later. It is also noted that for this coordinate system the free stream velocity vector is canted with respect to the x-axis.

A second coordinate system used in the two-dimensional wedge analysis but not presented in this section is depicted in Figure 12. The system is termed a "semi-polar" system. As with the Cartesian system, the wedge surface is a constant-coordinate surface.

#### Numerical Solution Technique

The integration in the Cartesian system is initiated using free stream values of the flow variables at each grid point in the y-direction along the  $x = 1$  line. This is commonly termed an impulsive start. The integration in the x-direction continues until the  $x = 2$  line is reached. At this point in the numerical process Kutler's stepback procedure is implemented<sup>(5)</sup>. This allows the integration to be re-started at  $x = 1$  with updated initial data taken from the  $x = 2$  line. In Figure 13 it is noted that grid points numbered 2, 4, 6, ..., m along the  $x = 2$  line are on the same rays from the origin as the grid points 2, 3, 4, ...  $m/2 + 1$  along the  $x = 1$  line. Since the flow is conical, data may be shifted along the rays from the  $x = 2$  to the

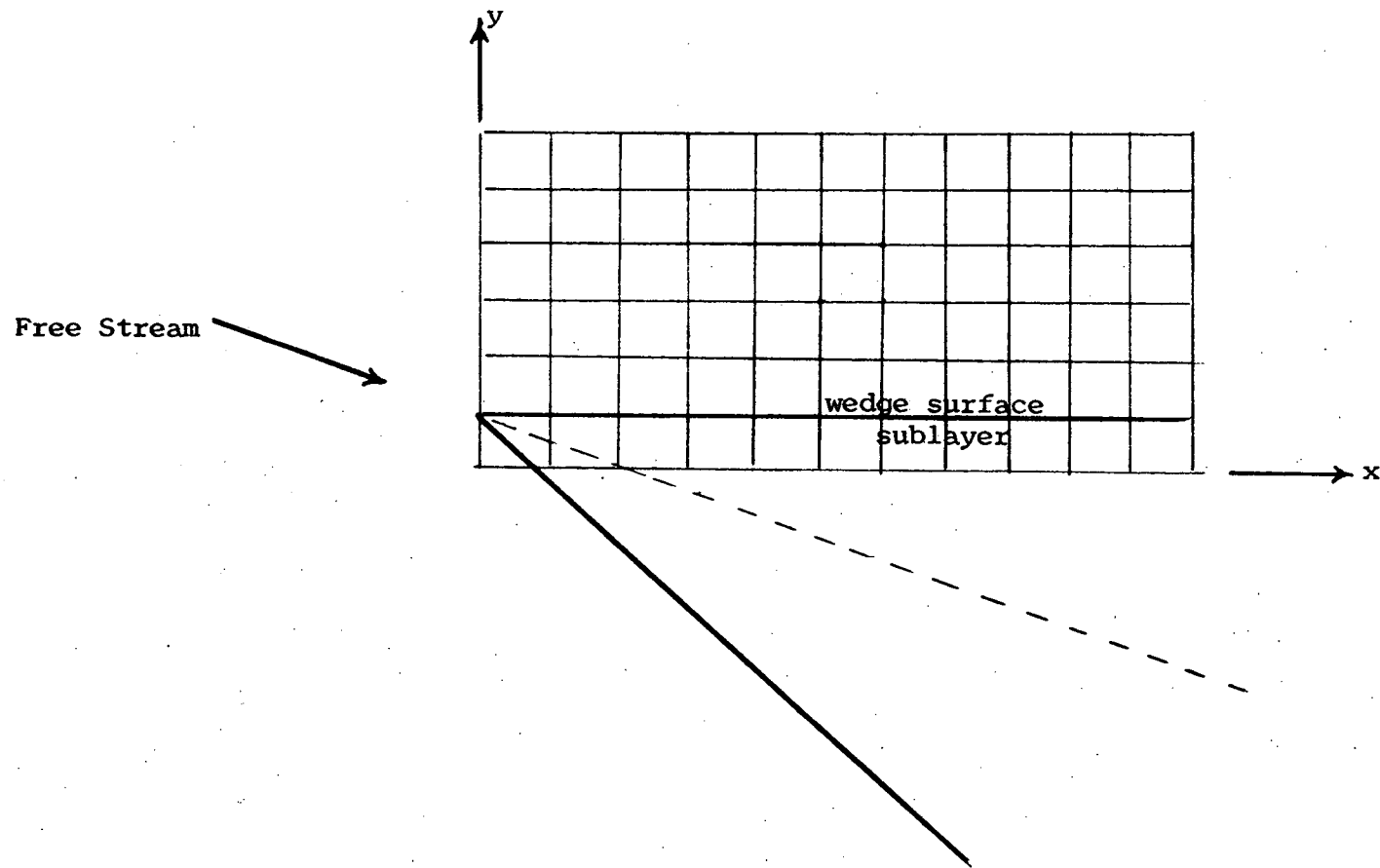


Figure 11. Coordinate system and grid system for 2-D wedge

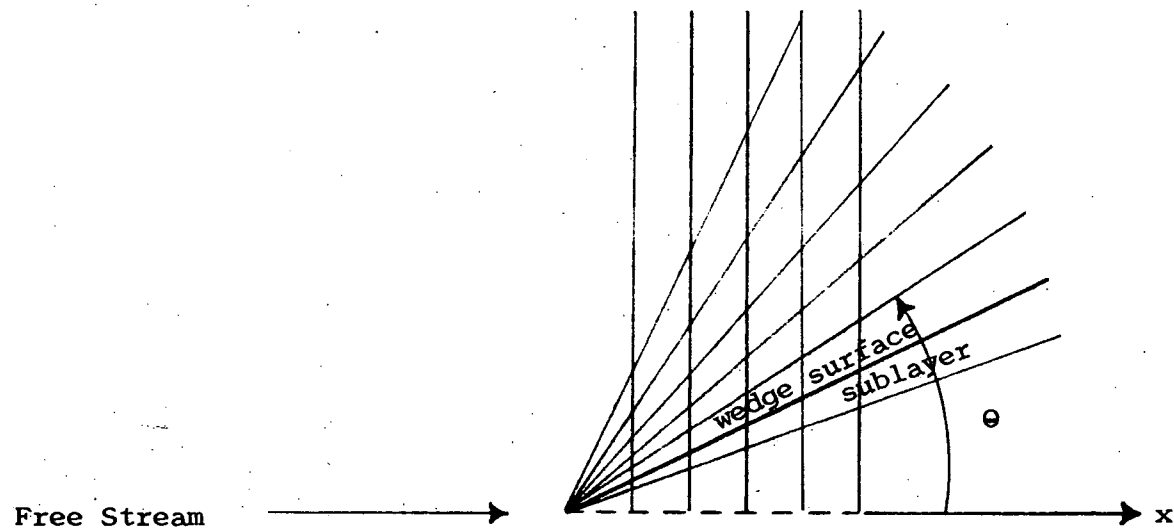


Figure 12. Coordinate system and grid system for 2-D wedge

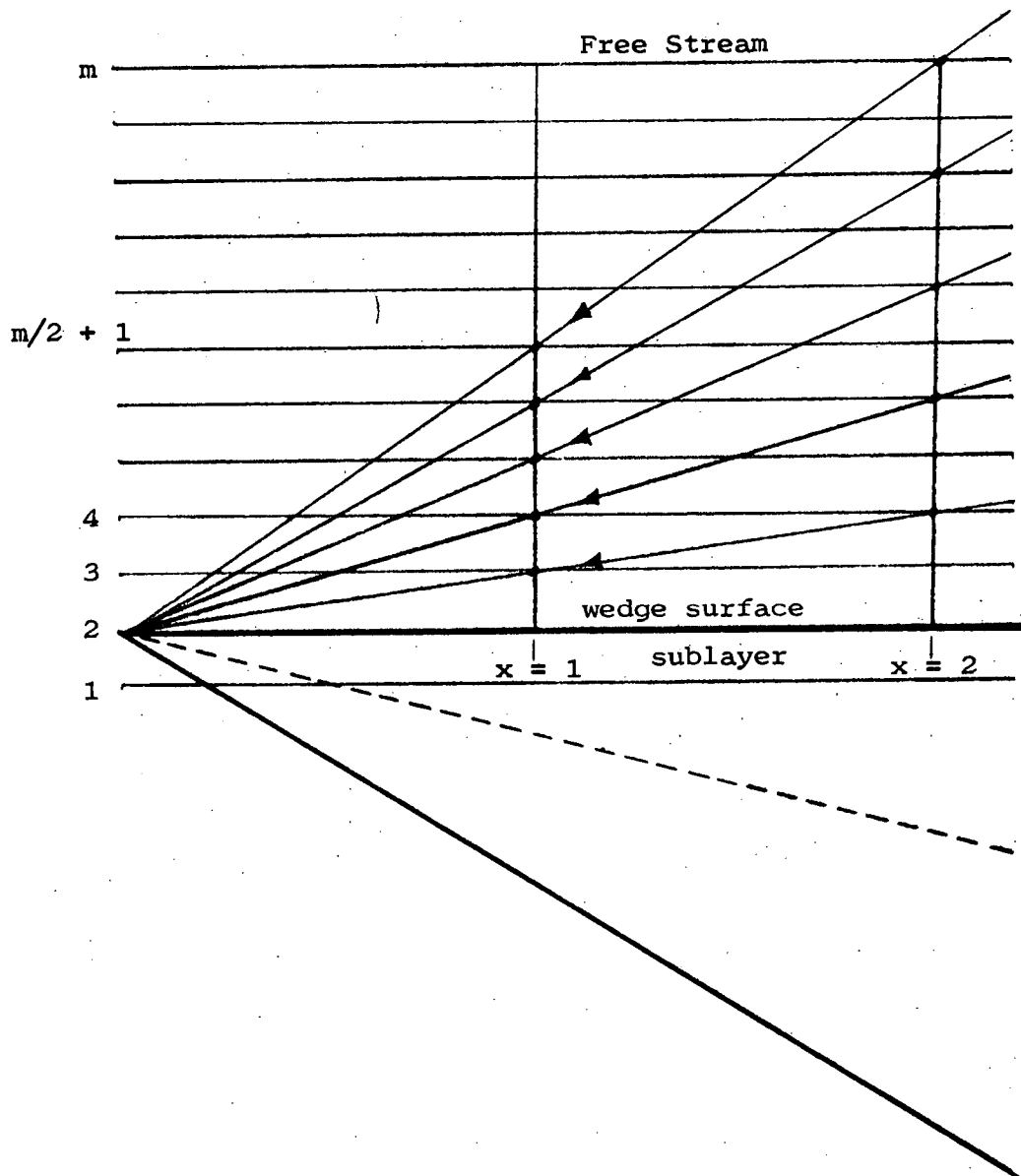


Figure 13. Kutler's stepback procedure

$x = 1$  grid points generating new initial data. For the scheme to work properly the grid points  $m/2, \dots, m$  must be outside the shock wave in the free stream. Solution convergence occurs when the initial data generated by successive stepbacks becomes constant.

It is noted that for the semi-polar system depicted in Figure 12 the stepback procedure becomes somewhat meaningless since the corresponding grid points at all  $x = \text{constant}$  stations lie on rays from the origin. Hence, the integration can proceed in the  $x$ -direction until no change occurs in the dependent variables along the rays.

Boundary conditions must be specified at the outer grid points and at the sublayer grid points since these are not integrated points. The dependent variables at the outer grid points are more easily handled. The grid is set up so that the outer edge is always in the free stream resulting in known constant boundary data. The grid points along the sublayer present a more difficult problem. The normal velocity component at the surface of the wedge must vanish since flow cannot pass through the surface. To satisfy this condition the normal velocity component is treated as an odd function at the body surface. That is, the sublayer value of the normal velocity component is set equal to the negative of the normal velocity component one layer above the surface. The values of the remaining dependent variables along the sublayer are evaluated using the reflection technique as used by Bohachevsky and Rubin<sup>(3)</sup>. The basic assumption used in this technique is that the normal derivatives

of the dependent variables vanish on the surface. Hence, the variables are treated as even functions on the wedge. That is, the dependent variables along the sublayer are set equal to their values one mesh point above the body. In view of the exact solution the reflection technique is exact for wedge flow in that the normal derivatives are zero.

### Numerical Solutions

Equations (30) were integrated using the Iowa State University IBM 360-65 computer system for both Rusanov's and MacCormack's methods for a wedge with a  $7.5^\circ$  half-angle at a Mach number of 2. Two mesh ratios ( $\Delta x/\Delta y$ ) were used. One at 1.272 which is near the experimental maximum for stability as determined by Kutler and the other at 1.0<sup>(5)</sup>. Three values of the stability parameter,  $\delta$ , associated with the Rusanov technique at a mesh ratio of 1.0 were used to assess the effect of  $\delta$  on the solution. In all cases the grid points in the y-direction consisted of a total of 30 mesh points.

Figure 14 shows the pressure distribution normal to the wedge surface using Rusanov's method at the lower mesh ratio of 1.0 for  $\delta$  values of 1.0, 2.0 and 3.0. The solution for a  $\delta$  of 1.0 is distinctly inferior to those obtained for  $\delta$  values of 2.0 and 3.0. This is a result of the excessive overshoots and undershoots in the vicinity of the shock. The solution for  $\delta = 2.0$  appears to yield a crisper shock than the solution for  $\delta = 3.0$  as well as lower

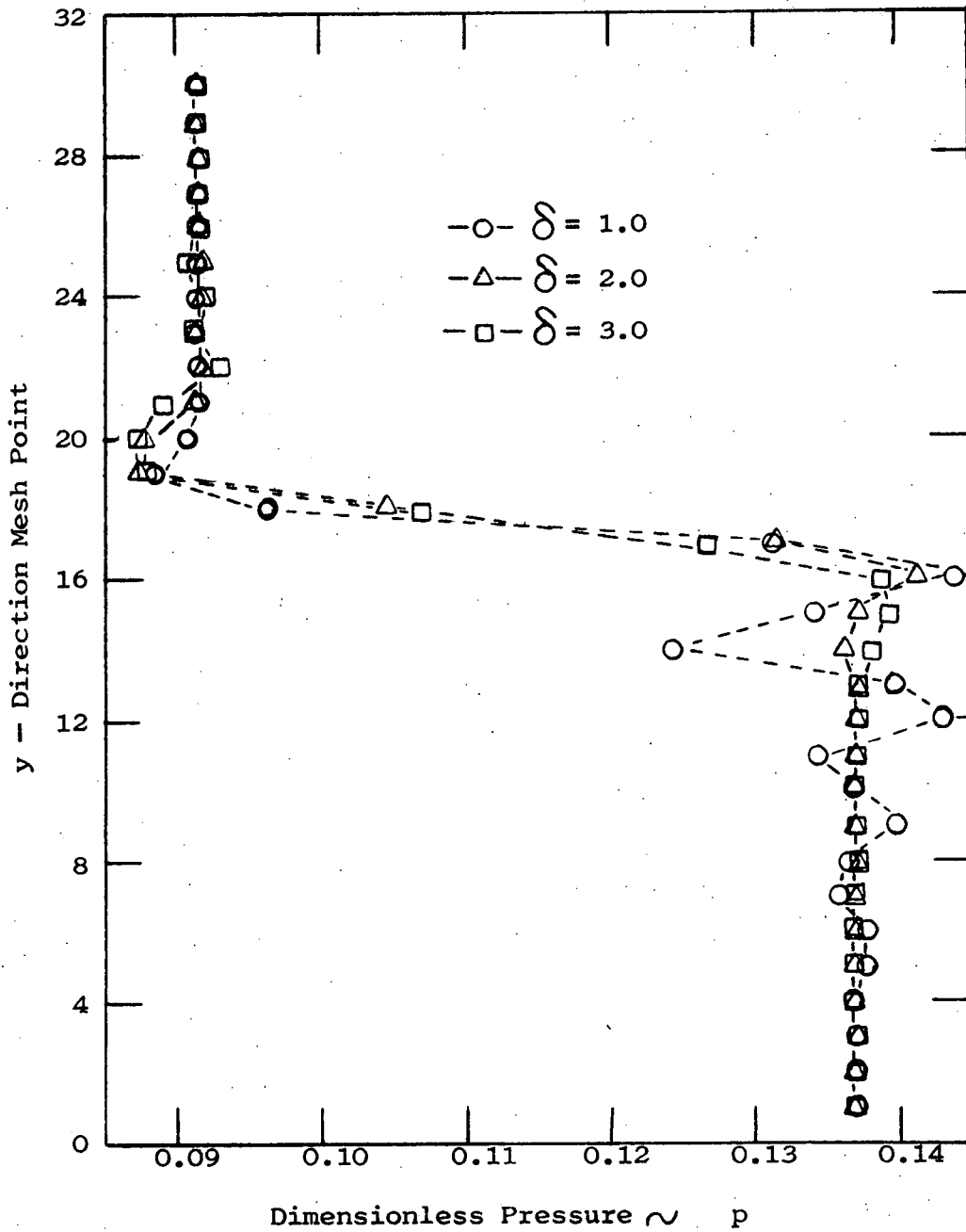


Figure 14. Pressure distribution in a direction normal to wedge surface. Rusanov technique for a two-dimensional wedge with half-angle  $7.5^\circ$  at a Mach number of 2 for  $\Delta x/\Delta y = 1.0$ .  $x = 1.0$

amplitude oscillations in the free stream after the shock is encountered.

Figure 15 shows a similar pressure distribution using the MacCormack technique for  $\Delta x/\Delta y = 1.0$ . Although there is some overshoot from the shock layer side, the behavior for the free stream side is very good with no oscillations occurring.

Figures 16 and 17 show the pressure distributions for the Rusanov and MacCormack methods, respectively, at the higher mesh ratio near the experimental stability bound. The Rusanov stability parameter,  $\delta$ , was set equal to 3.0 which, according to linear stability theory, is the only stable value when the maximum mesh ratio is used. The MacCormack technique develops a crisp shock with few oscillations as the shock is encountered on either side. The Rusanov solution, on the other hand, develops a fairly crisp shock but exhibits excessive oscillations on the free stream side of the shock. While decreasing the value of  $\delta$  improves the flow field behavior in the free stream, the shock layer portion of the solution becomes less well behaved in this case.

In all cases, the shock is properly located and the magnitudes of the dependent variables are correct.

There is about a 30 per cent savings in computation time as well as a substantial decrease in storage requirements using the MacCormack technique. Based on these criteria as well as the results discussed above, it would appear that the MacCormack technique is superior for solving the two-dimensional wedge flow problem in

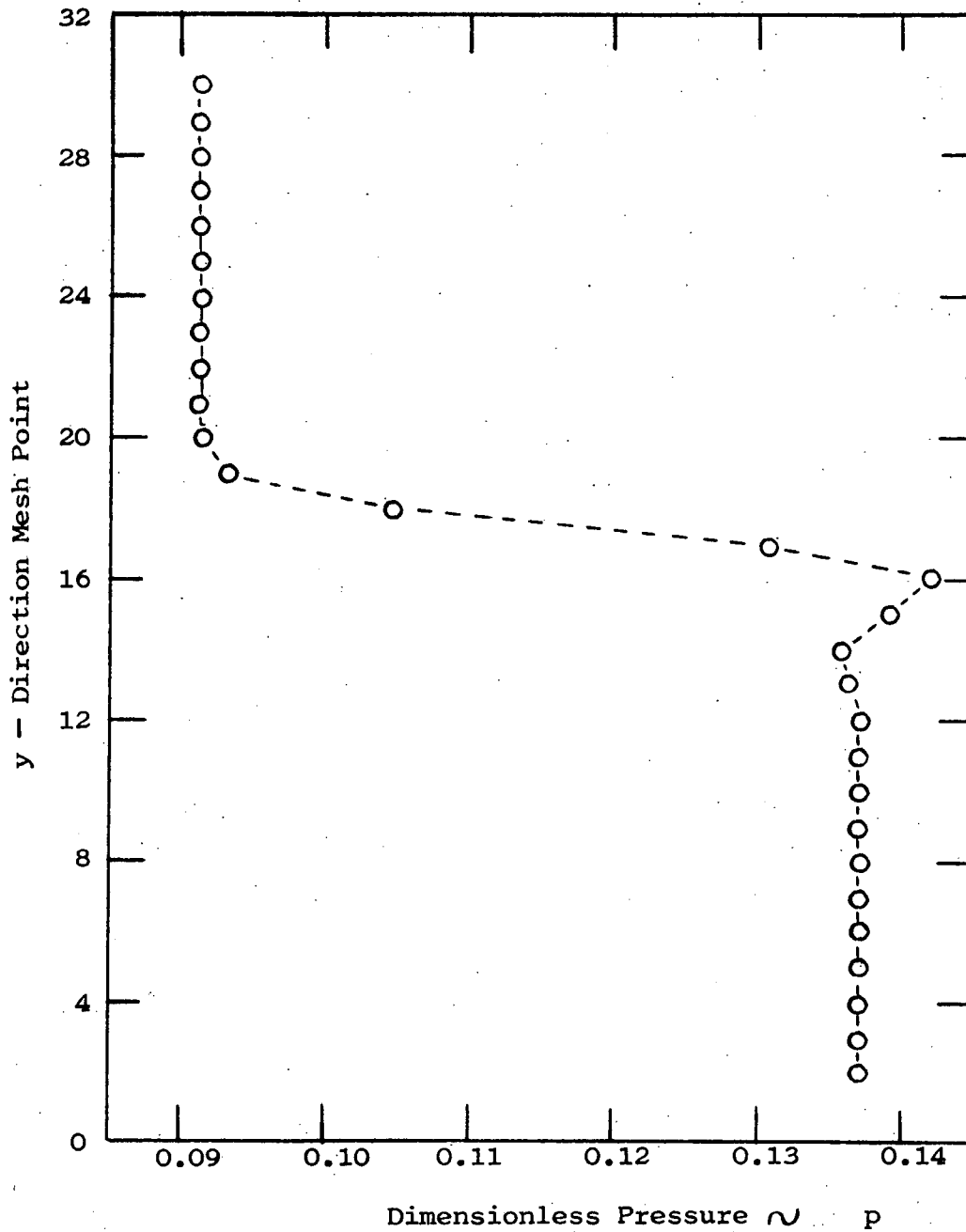


Figure 15. Pressure distribution in a direction normal to wedge surface. MacCormack technique for a two-dimensional wedge with half-angle  $7.5^\circ$  at a Mach number of 2 for  $\Delta x/\Delta y = 1.0$ .  $x = 1.0$

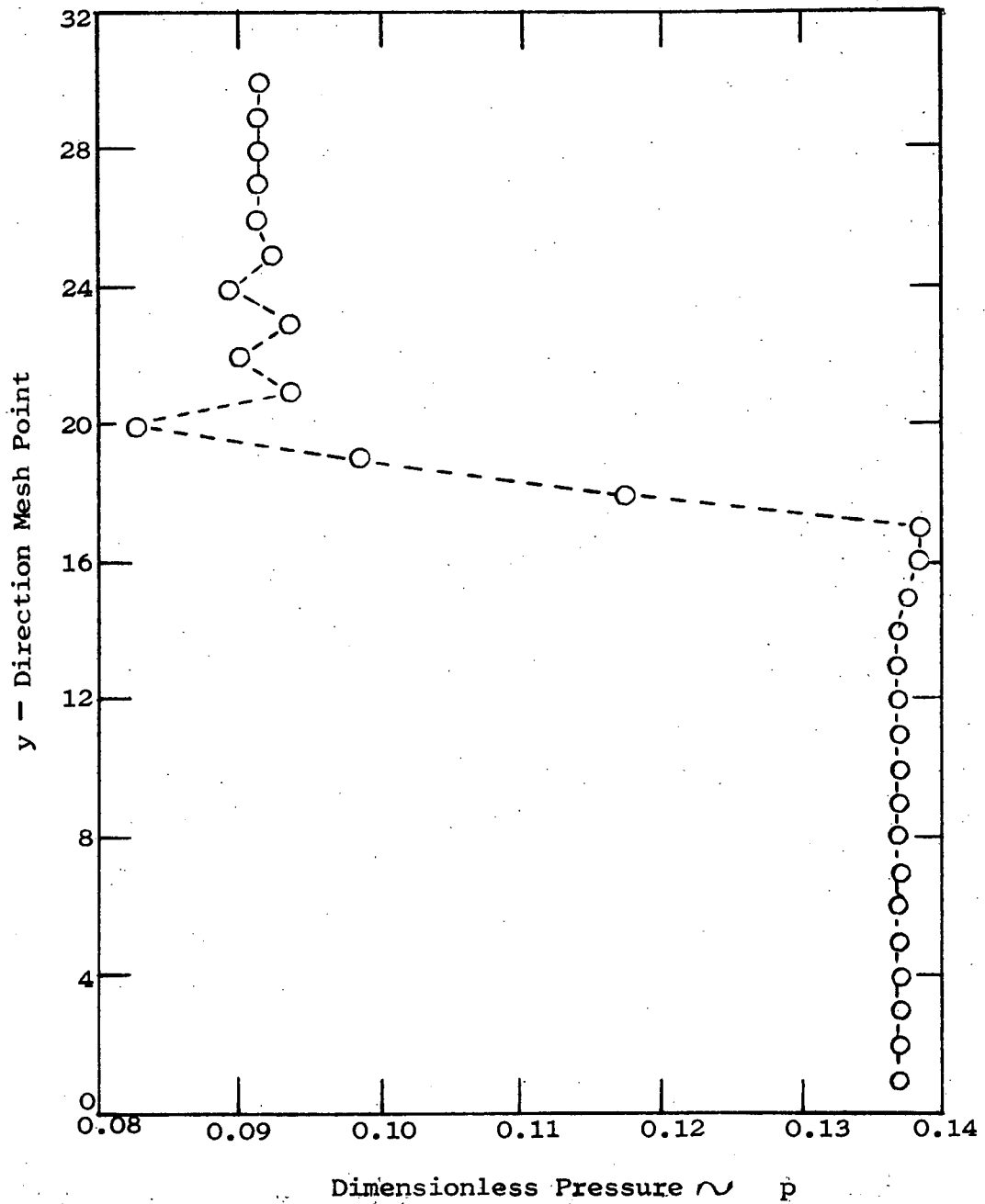


Figure 16. Pressure distribution in a direction normal to wedge surface. Rusanov technique for a two-dimensional wedge with half-angle  $7.5^\circ$  at a Mach number of 2 for  $\Delta x/\Delta y = 1.272$  and  $\delta = 3.0$ .  $x = 1.0$

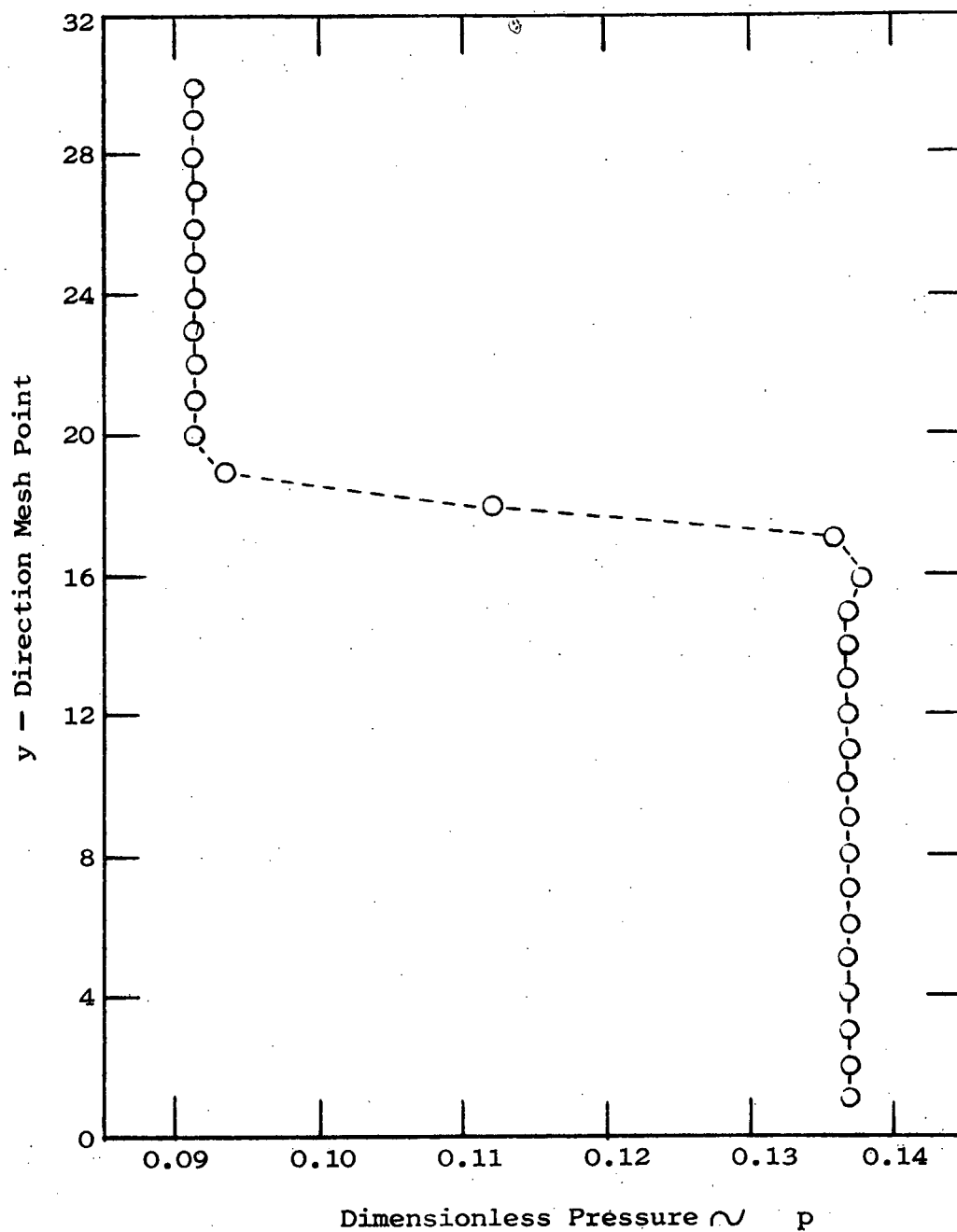


Figure 17. Pressure distribution in a direction normal to wedge surface. MacCormack technique for a two-dimensional wedge with half-angle  $7.5^\circ$  at a Mach number of 2 for  $\Delta x/\Delta y = 1.272$ .  $x = 1.0$

the range of Mach numbers and wedge angles examined here.

Additional experiments were performed using the semi-polar coordinate system described earlier. Although these solutions are not discussed here, they proved to be satisfactory. The major difference noted was that computation times required to reach a solution were longer.

## THE RECTANGULAR CONE-TIPPED WING

## Introduction

The primary objective of this investigation is to develop, by means of finite difference techniques, the flow field about a body in supersonic flight. Kutler and Lomax<sup>(23)</sup> have already investigated a variety of wings, bodies and their combinations including two-dimensional wedges, two-dimensional and axisymmetric-nonconical bodies, cones, planar delta wings and delta wings with dihedral mounted on conical bodies. The latter two studies were restricted to supersonic leading edges. His results obtained using shock capturing finite difference techniques agree well with the method of characteristics solutions and available experimental data.

The body considered in this paper is a three-dimensional rectangular wing with a symmetric double wedge cross section to which is attached a double cone tip as shown in Figure 18. The cone half-angle is chosen to be less than that of the tip Mach cone yielding a subsonic tip. Hence, the upper and lower surfaces are not independent as they are in the case of supersonic edges.

The flow field about the body can be separated into three distinct regions as indicated in Figure 19.

Region I contains the forebody flow field which begins at the cone-wedge vertex and ends at the mid-chord point. The wing aspect ratio and free stream Mach number are chosen such that the Mach

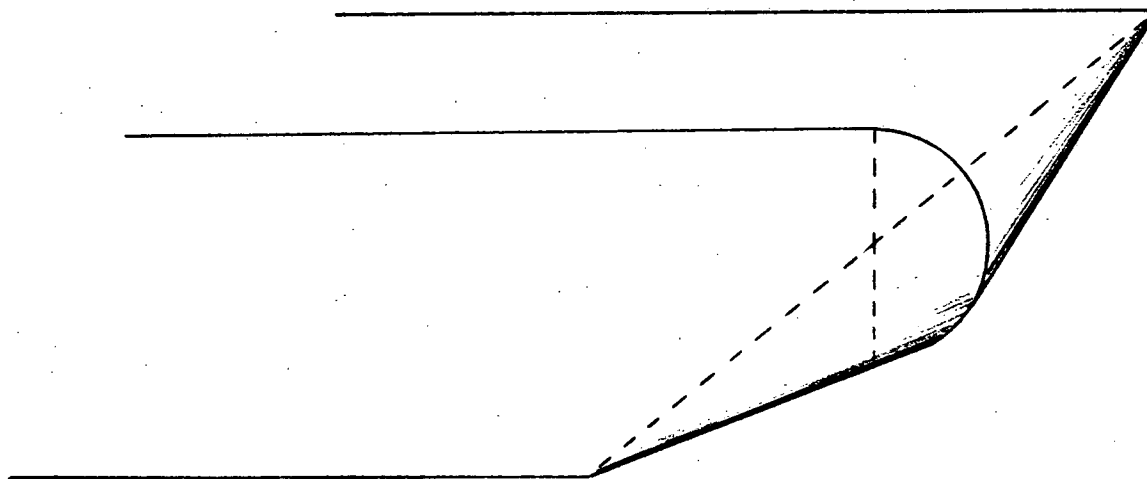


Figure 18. Symmetric double wedge rectangular wing with double cone tip

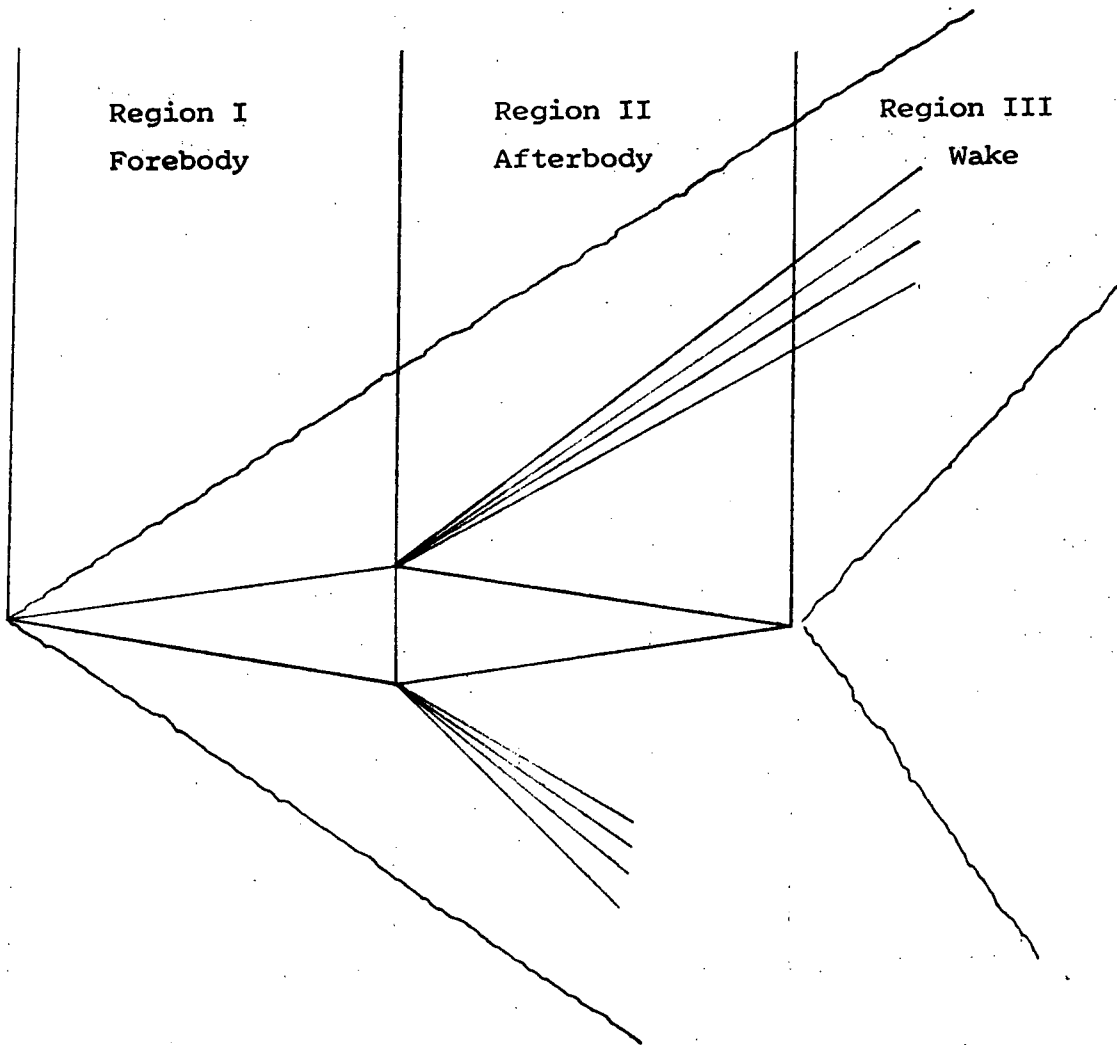


Figure 19. End view of 3-D rectangular wing showing the three regions of the flow field

cones from the wing tips do not intersect on the forebody. Hence, the flow in this region is entirely conical. That is, flow variables along rays from the vertex of the cone are constant. The flow field solution is generated using conical flow methods similar to those discussed in the section on 2-D wedges.

Region II contains the afterbody which begins at the mid-chord point and ends at the aft cone-wedge vertex. The partial differential equations governing the flow in this region represent an initial value problem that is solved using initial data generated in the forebody solution. That is, the flow variable magnitudes in the plane containing the base of the forebody are the initial data for the afterbody.

Region III contains the wake behind the wing which begins at the aft cone-wedge vertex and extends downstream indefinitely. Again, the problem in this region reduces to an initial value problem with initial data generated using the afterbody solution.

The sections that follow contain discussions of the problems and the solutions associated with each of the three regions. Discussion topics include equations of motion, coordinate systems, stability, boundary conditions, solution techniques and results.

### Equations of Motion

The basic flow equations that govern a supersonic flow are given by the conservation of mass, energy and momentum. The first two equations are scalar while the last is a three-component vector

equation yielding a total of five scalar equations of motion. For a steady, inviscid, nonheat-conducting and adiabatic flow these equations in vector notation are given by, respectively

$$\begin{aligned}\nabla \cdot (\rho \bar{q}) &= 0 \\ \bar{q} \cdot \nabla H_t &= 0 \\ \nabla (q^2/2) + (\nabla \times \bar{q}) \times \bar{q} + \nabla p/\rho &= 0\end{aligned}\tag{36}$$

For a Cartesian coordinate system Equations (36) may be written in the scalar form as follows:

Conservation of mass

$$(\rho u)_x + (\rho v)_y + (\rho w)_z = 0$$

x-direction momentum

$$(p + \rho u^2)_x + (\rho uv)_y + (\rho uw)_z = 0$$

y-direction momentum

$$(\rho uv)_x + (p + \rho v^2)_y + (\rho vw)_z = 0$$

z-direction momentum

$$(\rho uw)_x + (\rho vw)_y + (p + \rho w^2)_z = 0$$

Energy equation

$$p = \frac{\rho}{\gamma} \left[ 1 - \frac{\gamma-1}{2} (u^2 + v^2 + w^2) \right]$$

The dependent variables ( $p$ ,  $\rho$ ,  $u$ ,  $v$ ,  $w$ ) in Equations (37) are in a dimensionless form. The nondimensionalizing parameters for the pressure, density and velocity components are gamma times the free

stream stagnation pressure, the stagnation density and the stagnation speed of sound, respectively.

It is noted that only four of Equations (37) are partial differential equations. The fifth equation, the energy equation, is used in its integrated form to simplify the integration procedure.

Equations (37) and equivalent equations in other coordinate systems can be written in the general form

$$\bar{E}_x + \bar{F}_y + \bar{G}_z + \bar{H} = 0 \quad (38)$$

where  $\bar{E}$ ,  $\bar{F}$  and  $\bar{G}$  are vectors whose elements are conservative variables given by

$$\bar{E} = \left\{ \begin{array}{l} \rho u \\ p + \rho u^2 \\ \rho uv \\ \rho uw \end{array} \right\} \quad (39)$$

$$\bar{F} = \left\{ \begin{array}{l} \rho v \\ \rho uv \\ p + \rho v^2 \\ \rho vw \end{array} \right\} \quad (40)$$

$$\bar{G} = \left\{ \begin{array}{l} \rho w \\ \rho uw \\ \rho vw \\ p + \rho w^2 \end{array} \right\} \quad (41)$$

The vector  $\bar{H}$  represents the non-homogeneous portion of Equation (38) and is identically zero for the Cartesian form of the equation of motion. However, it is nonzero in the equations of motion associated with the forebody and afterbody flow because the Cartesian system is not employed in these regions, only in the wake region. The coordinate systems and associated equations of motion for regions other than the wake are developed and discussed in subsequent sections.

### Numerical Technique

Based on the analyses in previous sections concerning the modified Burger's equation and the two-dimensional wedge flow solutions, the MacCormack technique was chosen over the Rusanov technique. The criteria used to make the comparison were solution time and computer storage requirements as well as flow field resolution. Over the range of eigenvalues considered the MacCormack technique produced crisp shocks with few oscillations on either side of the shock, generally better than the Rusanov technique. Solution times were, on the average, thirty per cent less with a substantial decrease in the computer storage requirement.

The conclusions reached thus far may be somewhat misleading in that there appear to be situations in which the Rusanov technique is quite superior to that of MacCormack. Anderson and Vogel<sup>(21)</sup> have investigated the shock reflection problem in which a shock wave intersects a flat surface resulting in a second reflected shock. The equations of motion governing the flow are the normal fluid flow

equations discussed in this paper. One encounters a wide variation in eigenvalue magnitudes throughout the flow field in this situation. Hence, utilizing a constant mesh ratio in applying the numerical technique causes a portion of the solution to be developed at a very low effective Courant number. In those cases where the eigenvalues vary as much as a factor of ten, Rusanov's technique produces distinctly superior solutions. However, no reflected shocks are encountered in the rectangular wing problem and, as a result, such severe eigenvalue variations do not occur throughout the flow field.

The MacCormack predictor-corrector equations as applied to Equations (38) are given by

$$\begin{aligned} \tilde{E}_{j,k}^{n+1} &= E_{j,k}^n - \frac{\Delta x}{\Delta y} (F_{j+1,k}^n - F_{j,k}^n) \\ &\quad - \frac{\Delta x}{\Delta y} (G_{j,k+1}^n - G_{j,k}^n) - H_{j,k}^n \Delta x \\ E_{j,k}^{n+1} &= \frac{1}{2} \left[ E_{j,k}^n + \tilde{E}_{j,k}^{n+1} - \frac{\Delta x}{\Delta y} (\tilde{F}_{j,k}^{n+1} - \tilde{F}_{j-1,k}^{n+1}) \right. \\ &\quad \left. - \frac{\Delta x}{\Delta z} (\tilde{G}_{j,k}^{n+1} - \tilde{G}_{j,k-1}^{n+1}) - \tilde{H}_{j,k}^{n+1} \Delta x \right] \end{aligned} \quad (42)$$

The tilde that appears over certain of the variables denotes the predicted value of that particular variable whereas  $n$ ,  $j$  and  $k$  are the indicies associated with the  $x$ ,  $y$  and  $z$  directions respectively and serve to define the location of the grid points throughout the flow field.

### Stability Considerations

The quality of solutions obtained using Equations (42) depend to a great extent upon the magnitudes of the mesh ratios  $\Delta x/\Delta y$  and  $\Delta x/\Delta z$ . Operation at mesh ratios outside the stable range leads to divergence whereas values well below the maximum stable values lead to poor flow field resolution in the neighborhood of the shock. Hence, it is quite desirable to have a priori knowledge of stable ranges of the mesh ratios in setting up the flow field grid.

Kutler and Lomax<sup>(23)</sup> present criteria based on amplification matrix theory to theoretically predict stability bounds in multi-dimensional problems. To utilize the analysis one must know the eigenvalues of the coefficient matrices of the gas-dynamic equations of motion. In his work Kutler<sup>(5)</sup> developed the coefficient matrices for the equations of motion in a Cartesian system and determined the associated eigenvalues. For convenience, his work is outlined in Appendix A. The stable ranges for the mesh ratios are given by

$$\frac{\Delta x}{\Delta y} \leq \frac{1}{|\lambda_{A_{\max}}|}$$

$$\frac{\Delta x}{\Delta z} \leq \frac{1}{|\lambda_{B_{\max}}|}$$
(43)

where  $\lambda_{A_{\max}}$  and  $\lambda_{B_{\max}}$  represent the maximum eigenvalues of the

A and B matrices respectively. One can obtain approximate values for the maximum eigenvalues to be used in conjunction with Equations (43) to set up a grid in which the mesh ratios are near their maximum value yielding near-optimum numerical results.

### Region I Flow Field Analysis

#### Forebody geometry and coordinate systems

That portion of the body contained between the leading edge of the wing and the shoulder at mid-chord constitutes the forebody. The geometry of the forebody and the associated Cartesian coordinate system are depicted in Figure 20. As noted in Figure 20, the forebody can be separated into two parts. The first part, the wing proper, consists of a wedge with half-angle  $\theta_w$  while the second part, the wing tip, consists of a half-cone having the same half-angle  $\theta_c$  as the wedge. Hence, a smooth transition is made from the wedge to the cone with no discontinuities in surface slope. Since the wing is not cambered, the forebody cross section is symmetric with respect to the chord plane.

The Cartesian coordinate system associated with the forebody has the origin at the apex of the cone. The y-axis is perpendicular to the plane of symmetry, the x-axis is in the chord plane (the plane of symmetry) and the z-axis extends along the span of the wing. The positive directions are as shown in Figure 20.

It has been noted earlier that a coordinate system in which the body can be described by a constant coordinate surface is highly

desirable. For the forebody this is most easily accomplished using two systems, one for the wing proper and one for the half-cone.

The coordinate system used to describe the half-cone and the corresponding flow field region is shown in Figure 21. The coordinate  $\phi$  defines the angle between the interface plane (the plane containing the intersection of the wedge and cone) and the cone meridian plane containing the point  $(\xi, \theta, \phi)$ . The coordinate  $\theta$  defines the angle between the cone axis and the radius to the point of interest. The coordinate  $\xi$  is simply the x position of the point.

The coordinate system associated with the forebody wing proper and corresponding flow field is shown in Figure 22. Only the upper half of the body is shown. The coordinate  $\phi$  represents the angle between the interface plane and the plane normal to the chord plane and containing the radius to the point  $(\xi, \theta, \phi)$ . The coordinate  $\theta$  represents the angle between the chord plane and the projection of the radius on the interface plane. The coordinate  $\xi$  is the x position of the point.

The grid system generated by the coordinate system is defined by the intersection of a set of  $\phi = \text{constant}$  planes, a set of  $\theta = \text{constant}$  surfaces, one of which defines the body, and a  $\xi = \text{constant}$  plane. The grid in a typical  $\xi = \text{constant}$  plane is depicted in Figure 23. The grid points associated with the wedge in the interface plane are identical with those of the half-cone. It is noted here that corresponding grid points in successive  $\xi = \text{constant}$  planes lie along rays from the common origin of the coordinate

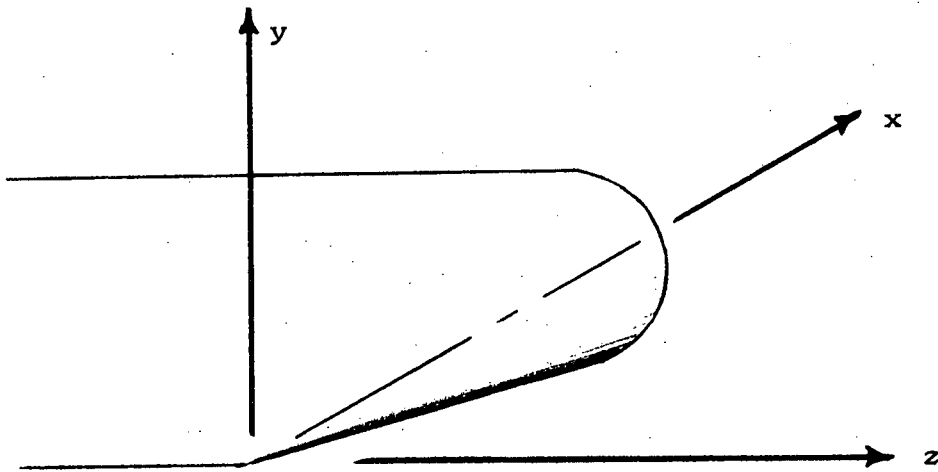


Figure 20. Wing forebody geometry

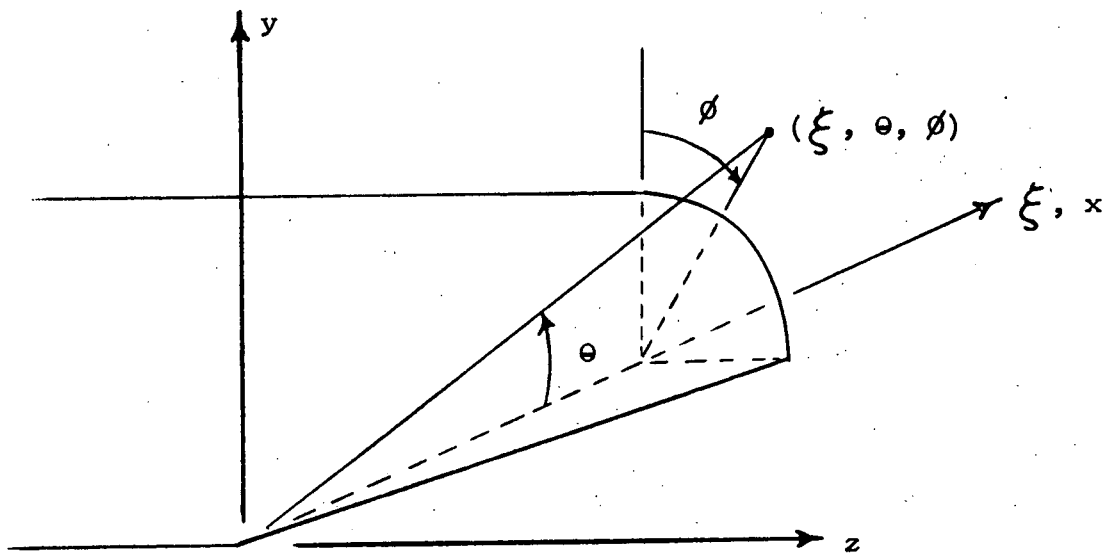


Figure 21. Coordinate system used to describe half-cone and corresponding flow field region

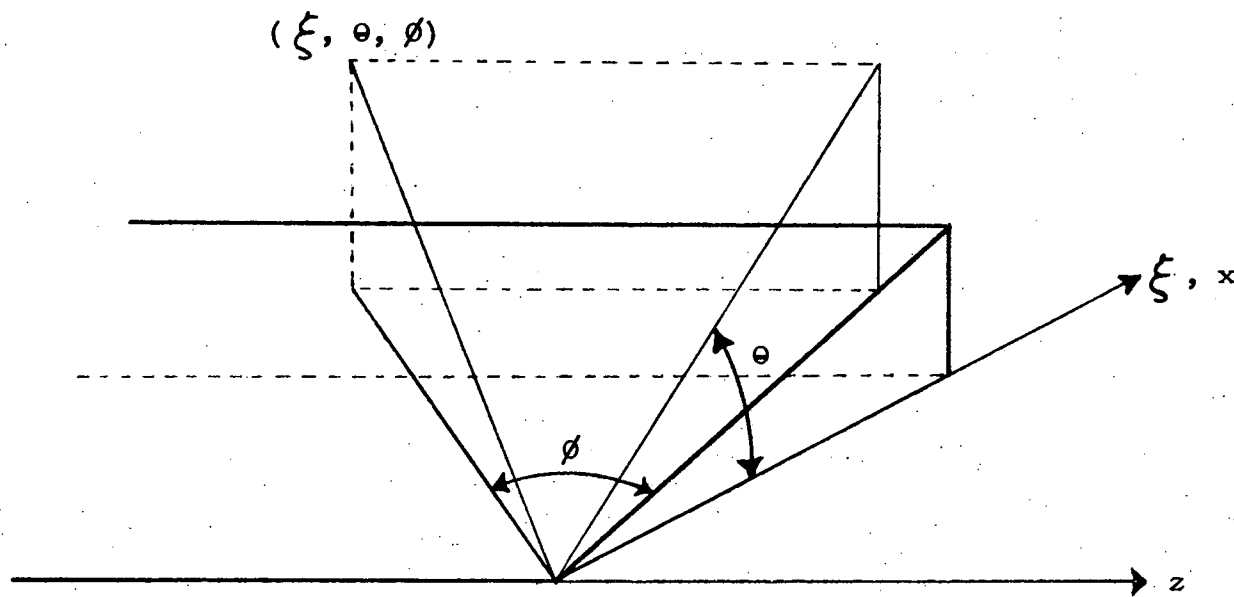


Figure 22. Coordinate system used to describe the wing proper of the forebody and corresponding flow field region

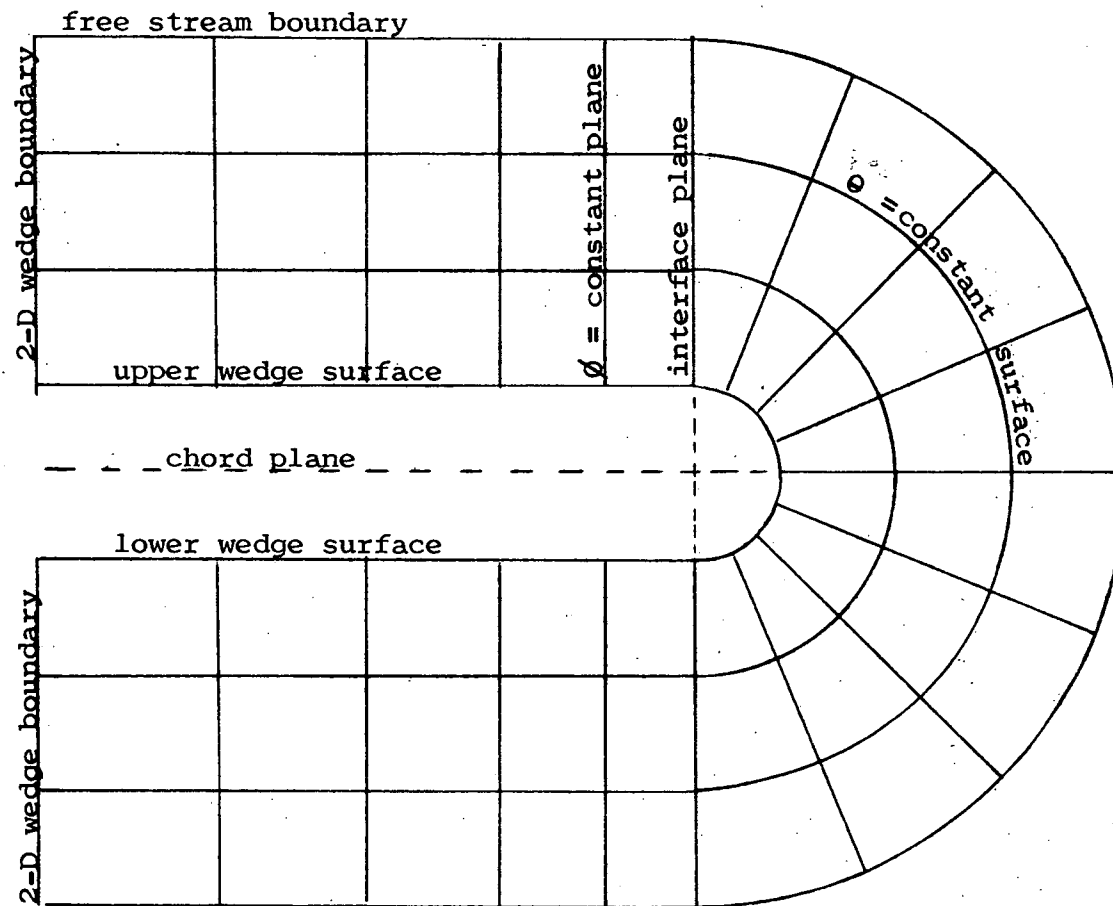


Figure 23. Grid system in a  $\xi = \text{constant}$  plane generated by the coordinate systems associated with the forebody

systems. Hence, the stepback procedure becomes somewhat trivial in the forebody solutions.

#### Forebody flow equations of motion

To obtain flow field solutions in Region I the flow equations must be transformed from their Cartesian form given in Equations (37) to the new systems described in Figures 21 and 22. The mechanics of the transformations are presented in Appendix B.

The transformed equations of motion for both the wedge proper and the half-cone for the forebody region as given by Equations (B4) and (B5) are of the general conservative form

$$\bar{E}'_{\xi} + \bar{F}'_{\theta} + \bar{G}'_{\phi} + \bar{H}' = 0 \quad (44)$$

The conservative variable vectors  $\bar{E}'$ ,  $\bar{F}'$ , and  $\bar{G}'$  as well as the nonhomogeneous term  $\bar{H}'$  for the wedge proper are given by

$$\bar{E}' = \xi \bar{E} \quad (45)$$

$$\bar{F}' = -\sin\theta \cos\theta \bar{E} + \cos^2\theta \bar{F} \quad (46)$$

$$\bar{G}' = -\sin\phi \cos\phi \bar{E} + \cos^2\phi \bar{G} \quad (47)$$

$$\begin{aligned} \bar{H}' = & (-2\sin^2\theta - \sin^2\phi + \cos^2\phi)\bar{E} \\ & + 2\sin\theta \cos\theta \bar{F} + 2\sin\phi \cos\phi \bar{G} \end{aligned} \quad (48)$$

and for the half-cone are given by

$$\bar{E}' = \xi \tan\theta \bar{E} \quad (49)$$

$$\bar{F}' = -\bar{E}\sin^2\theta + \bar{F}\sin\theta\cos\theta\cos\phi + \bar{G}\sin\theta\cos\theta\sin\phi \quad (50)$$

$$\bar{G}' = -\bar{F}\sin\phi + \bar{G}\cos\phi \quad (51)$$

$$\begin{aligned} \bar{H}' = & (2\sin\theta\cos\theta - \tan\theta)\bar{E} \\ & + 2\bar{F}\cos\phi\sin^2\theta + 2\bar{G}\sin^2\theta\sin\phi \end{aligned} \quad (52)$$

where the vectors  $\bar{E}$ ,  $\bar{F}$  and  $\bar{G}$  are the conservative variables associated with the standard Cartesian form of the equations of motion and are defined in Equations (39), (40) and (41).

The scalar components of Equations (44) represent the conservation of mass and the x, y and z direction momentum equations. The energy equation is not included in this set since it is used in the integrated form as given by the last of Equations (37).

#### Evaluation of gas dynamic variables from conservative variables

In the integration process, the set of predictor-corrector equations developed by MacCormack are used to determine only the numerical values associated with the scalar components of the vector  $\bar{E}'$ . Each time that  $\bar{E}'$  is updated along the integration path in the  $\xi$ -direction the remaining conservative vectors  $\bar{F}'$  and  $\bar{G}'$  as well as the nonhomogeneous term  $\bar{H}'$  must be numerically evaluated. Since  $\bar{F}'$ ,  $\bar{G}'$  and  $\bar{H}'$  are functions of  $p$ ,  $\rho$ ,  $u$ ,  $v$ ,  $w$  one must extricate from  $\bar{E}'$  the gas dynamic variables.

In the coordinate systems used to describe the various regions of the wing and surrounding flow field the variables  $\bar{E}'$  are simple functions of only the Cartesian counterpart  $\bar{E}$ . Hence, it is

convenient to evaluate the gas dynamic variables using a two-step process. In the first step the scalar components of  $\bar{E}$  are evaluated. Secondly, the gas dynamic variables are evaluated using the inverse of the relationships  $E(p, \rho, u, v, w)$  and the integrated form of the energy equation. The explicit forms for the variables  $p, \rho, u, v$  and  $w$  are developed in the following work.

In view of Equation (39) the scalar components of  $\bar{E}$  are given by

$$E_1 = \rho u \quad (53)$$

$$E_2 = p + \rho u^2 \quad (54)$$

$$E_3 = \rho uv \quad (55)$$

$$E_4 = \rho uw \quad (56)$$

Dividing Equations (55) and (56) by (53) yields

$$v = E_3/E_1 \quad (57)$$

$$w = E_4/E_1 \quad (58)$$

Combining Equations (53), (54) and the last of Equations (37), the energy equation, yields

$$u = \frac{\gamma \frac{E_2}{E_1} \pm \left[ \left( \frac{\gamma E_2}{E_1} \right)^2 + 4 \left[ \left( \frac{\gamma+1}{2} \right) \left( \frac{\gamma-1}{2} v^2 + \frac{\gamma-1}{2} w^2 - 1 \right) \right] \right]^{\frac{1}{2}}}{(\gamma+1)} \quad (59)$$

The positive sign is used since flow is supersonic throughout the flow field. Equation (53) may then be used to evaluate density as follows,

$$\rho = E_1/u \quad (60)$$

and the energy equation for pressure

$$p = \frac{\rho}{\gamma} \left( 1 - \frac{\gamma-1}{2} q^2 \right) \quad (61)$$

The relationships between  $\bar{E}$  and  $\bar{E}'$  for the wedge proper and the half-cone in the forebody region are given by Equations (45) and (49) respectively.

#### Initial and boundary conditions

In the application of MacCormack's technique the grid points existing on the boundaries of the grid system depicted in Figure 23 are not integrated points. Hence, a set of boundary conditions must be developed to specify the values of the gas dynamic variables along the upper and lower two-dimensional wedge boundaries, the outer free stream boundary and the upper and lower wing surfaces.

The conditions along the outer free stream boundary are most easily specified since the grid is always made large enough that the outermost grid points always lie outside the shock in the free stream. Thus, the gas dynamic variables at these locations retain their constant free stream values.

The upper and lower two-dimensional wedge boundaries are placed toward the center of the wing well outside the Mach cones

emanating from the half-cone vertices of the wing tips. Hence, these grid points exist in the two-dimensional wedge regions of the wing flow field for which exact solutions are known. The gas dynamic variables along these boundaries are frozen at the two-dimensional wedge flow values dictated by the exact solution. The dimensionless shock layer pressure is given by Equation (34), the dimensionless density is given by<sup>(22)</sup>

$$\frac{\rho_w}{\rho_\infty} = \frac{(\gamma+1) M_\infty^2 \sin^2 \beta'}{(\gamma-1) M_\infty^2 \sin^2 \beta' + 2} \quad (62)$$

and the dimensionless rectangular velocity components are given by

$$\frac{u_w}{q_\infty} = \frac{(\gamma-1) M_\infty^2 \sin^2 \beta' + 2}{(\gamma+1) M_\infty^2 \sin \beta'} \quad (63)$$

$$\frac{v_w}{q_\infty} = \frac{u_w}{q_\infty} \tan \theta_w \quad (64)$$

$$w_w = 0 \quad (65)$$

where  $\beta' = \beta_{\text{upper}} + \alpha$  for the upper surface and  $\beta' = \beta_{\text{lower}} - \alpha$  for the lower surface (see Figure 24). Equation (35) defines the shock wave location for the upper and lower surfaces in the two-dimensional regions with  $\theta = \theta_w - \alpha$  and  $\theta = \theta_w + \alpha$  for the upper and lower surfaces respectively.

The boundary conditions that must be specified along the surface of the wing in each  $\xi = \text{constant}$  plane are somewhat more

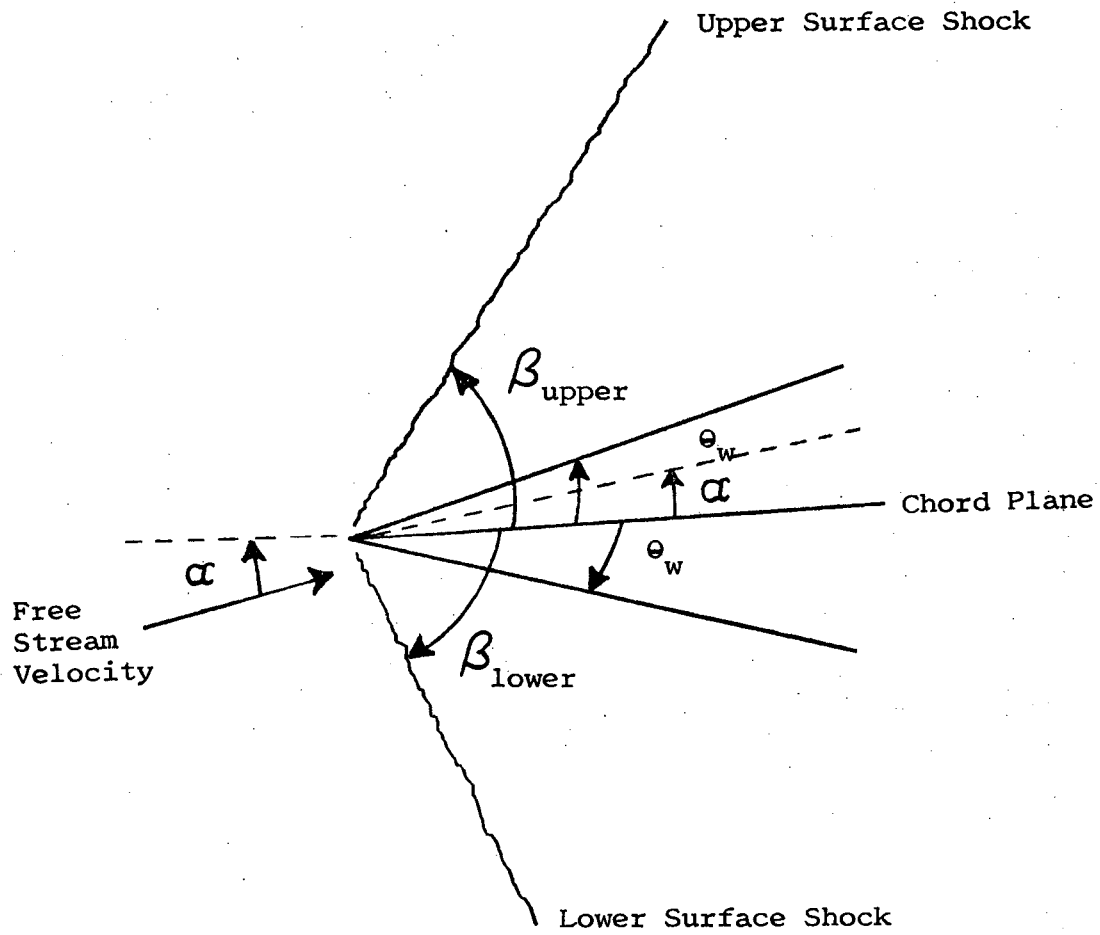


Figure 24. Forebody wedge cross section in two-dimensional flow region showing upper and lower surface shock waves and associated geometry

complex. Although a variety of techniques has been developed many of the procedures are fairly difficult to implement and sometimes quite costly in terms of computing times. Also some yield questionable results.

Abbett<sup>(24)</sup> has reviewed and compared many of the procedures currently in use for calculation of surface boundary points. Included in the survey are reflection techniques, explicit and implicit differencing using one-sided derivative approximations, characteristics techniques and techniques utilizing extrapolation from interior points to the boundary. In addition, Abbett<sup>(24)</sup> has developed a new scheme in conjunction with MacCormack's differencing technique to evaluate the gas dynamic variables along the wall. The method is analytically simple, easy to incorporate, computationally fast and satisfies an entropy condition on the body surface that the other techniques do not. Although the basic Abbett technique does not appear to give good results for bodies having high curvature, a slight modification yields a very usable scheme which is applied in this study. The following paragraphs include an explanation of the basic Abbett technique as well as the required modifications.

The basic Abbett boundary condition scheme is a two-step predictor-corrector sequence in which the prediction step consists of the original MacCormack predictor. All gas dynamic variables on the body are evaluated in this step. In general, the predicted velocity at the body will not be parallel to the surface. The corrector step, then, consists of an application of a simple

isentropic flow expansion or compression, whichever is necessary, to turn the flow parallel to the surface. Then the body pressure is corrected by the amount dictated by the expansion or compression angle and the body density is determined using the surface entropy value as well as the corrected pressure. The modulus of the velocity on the body surface is corrected by using the energy equation.

The angle ( $\delta$ ) through which the flow must be turned after the predictor step to align the flow with the surface is given by

$$\delta = \sin^{-1} \frac{\bar{q}_p \cdot \hat{n}}{\bar{q}_p} \quad (66)$$

where the subscript p denotes predicted value and  $\hat{n}$  is the unit vector normal to the surface.

Now that the turning angle for the expansion or compression has been evaluated, the corrected pressure may be determined using a truncated form of the Prandtl-Meyer function<sup>(25)</sup> given by

$$\frac{P_c}{P_p} = 1 - \frac{\gamma M^2}{\sqrt{M^2-1}} \delta + \gamma M^2 \left[ \frac{(\gamma+1)M^4 - 4(M^2-1)}{4(M^2-1)^2} \right] \delta^2 \quad (67)$$

The subscript c denotes corrected value and the parameter M denotes the predicted value for surface Mach number. It is noted here that for positive  $\delta$  quantities the flow must be expanded and for negative values the flow must be compressed.

Since the surface entropy is known and constant the body density may be corrected using

$$\rho_c = \bar{\rho} (p_c / \bar{p})^{1/\gamma} \quad (68)$$

where the barred quantities are known constants.

The corrected velocity modulus from the energy equation is given by

$$|\bar{q}_c| = \left[ \left( \frac{2}{\gamma-1} \right) \left( 1 - \frac{\gamma p_c}{\rho_c} \right) \right]^{1/2} \quad (69)$$

whereas the proper velocity direction is defined by means of the unit vector

$$\hat{i}_q = \frac{\bar{q}_p - (\bar{q}_p \cdot \hat{n}) \hat{n}}{|\bar{q}_p - (\bar{q}_p \cdot \hat{n}) \hat{n}|} \quad (70)$$

Equation (70) is developed by removing the normal component of the predicted velocity and normalizing the resulting vector which effectively defines a unit vector parallel to the surface. The combination of Equations (69) and (70) yields the corrected velocity

$$\bar{q}_c = |\bar{q}_c| \hat{i}_q \quad (71)$$

from which the rectangular components  $u_c$ ,  $v_c$  and  $w_c$  may be determined.

Ferri<sup>(26)</sup> has shown that for conical flow the entropy along a streamline remains constant. Hence, the body entropy can be defined once the body streamline is identified. Since the streamlines that wet the body surface emanate from the two-dimensional regions outside the tip Mach cone, the entropy values can be obtained from the exact

2-D wedge solutions. For the angle-of-attack case the upper and lower surface shock waves in the 2-D regions are of different strengths yielding different body entropies for the upper and lower surfaces. Ferri<sup>(26)</sup> also shows that vortical singularities can, in fact, occur at those points in the flow field where both the normal velocity component (normal to the radius from the origin) and the crossflow velocity component vanish. Since the normal component of velocity is zero everywhere on the body surface a vortical singularity on the body can occur only where crossflow stagnates. Hence, to apply Equation (68) one simply uses upper surface 2-D values of  $\bar{p}$  and  $\bar{\rho}$  along the upper surface 3-D region until the crossflow stagnation point is reached. Then the lower surface 2-D values must be used.

For bodies having high curvature the prediction step in the basic Abbett technique appears to misalign the flow on the body surface. The Abbett corrector then continuously compresses (shock layer region) or expands (expansion region) the flow throughout the integration process resulting in very large or near zero body pressures respectively. To remedy the situation the reflection technique is used after the prediction step to produce more realistic body flow variables for the Abbett correction step.

A sublayer is added to the grid system. This yields a set of mesh points below the body surface as depicted in Figure 23. The sublayer values of the flow variables are estimated by treating the normal velocity component as an odd function and the radial and

crossflow components as well as the pressure and density as even functions at the body surface. The normal, radial and crossflow scalar velocity components are given by

$$\begin{aligned}
 q_n &= \bar{q} \cdot \hat{n} \\
 q_r &= \bar{q} \cdot \hat{i}_r \\
 q_c &= \bar{q} - \bar{q}_n - \bar{q}_r
 \end{aligned}
 \tag{72}$$

respectively, where  $\hat{i}_r$  is the unit vector in the radial direction. The resulting equations defining the sublayer flow variables are given by

$$\begin{aligned}
 p_1 &= p_3 \\
 \rho_1 &= \rho_3 \\
 q_{n_1} &= -q_{n_3} \\
 q_{r_1} &= q_{r_3} \\
 q_{c_1} &= q_{c_3}
 \end{aligned}
 \tag{73}$$

where subscripts 1 and 3 denote sublayer and superlayer values respectively.

Once the sublayer values are known the body surface grid points may then be evaluated using the MacCormack corrector. The resulting body flow variables are used as inputs to the Abbett boundary condition routine which satisfies the body entropy condition.

The integration procedure is started impulsively. That is, the gas dynamic variables at the interior grid points are initially set at free stream values. Although different initial data may be used to initiate the integration the impulsive start seems to be quite convenient. As the integration proceeds from one  $\xi$  plane to the next, the shock wave moves from the body surface out into the flow field to its proper location.

#### Choice of grid system

In view of the stability and accuracy considerations presented earlier the forebody grid should be chosen such that the mesh ratios  $\Delta\xi/\Delta\theta$  and  $\Delta\xi/\Delta\phi$  are near their upper bounds for stability on both the wedge proper and the tip half-cone. Failure to do so may yield poor solutions in portions of the flow field. Of greatest importance is the  $\Delta\xi/\Delta\theta$  ratio since the shock wave is encountered in the  $\theta$  direction. In previous work dealing with the 2-D wedge solutions it was noted that the most disastrous effects of suboptimal Courant number operation occur in the vicinity of the shock. One can expect both a smeared shock and severe oscillations in the neighborhood of the shock. Hence, the grid work is constructed such that the ratio  $\Delta\xi/\Delta\theta$  is always near the maximum value for stability. The Mach numbers and angles of attack used in this study are such that no rapid expansions and, as a result, possible recompression shocks are encountered in the  $\phi$  direction. Therefore, the increment  $\Delta\phi$  is chosen such that the ratio  $\Delta\xi/\Delta\phi$  is as close to its maximum value as possible without having either too few or

an excessive number of grid points. The latter case leads to lengthy computation times.

An estimate of the maximum mesh ratios and, as a result, the proper grid spacing can be made using the criteria given by Equations (43). Hence, the eigenvalues of the coefficient matrices of the gas dynamic equations of motion in the forebody coordinate system must be evaluated. The development of the expressions for the forebody eigenvalues is presented in Appendix A.

The gas dynamic equations of motion for the forebody are given by Equations (A11) where the coefficient matrices  $A'$  and  $B'$  are defined in Equations (A12) - (A15). The five eigenvalues associated with each of the coefficient matrices are given by Equations (A16) - (A23).

The eigenvalues were determined numerically at all grid points in various preliminary solutions for a Mach number of 2 and angles of attack of 0 and 4 degrees. In all cases observed the triple repeated eigenvalues were the smallest. Thus, the largest of the eigenvalues given by Equations (A17), (A19), (A21) and (A23) represent the maximum for the corresponding matrices. For the wedge proper the maximum eigenvalues for the  $A'$  and  $B'$  matrices were near unity and for the tip half-cone 1.0 and 6.5 respectively.

Since the eigenvalues of  $A'$  for both the wedge proper and the cone tip have approximately the same maximum magnitude the corresponding  $\Delta\theta$  increments for maximum stable values of the ratio  $\Delta\xi/\Delta\theta$  for both regions are very nearly the same. Therefore,

using a common  $\Delta\theta$  in both regions is quite desirable from the stability viewpoint and certainly makes the computational process much simpler.

On the other hand, in view of the maximum eigenvalues of the  $B'$  matrices, the  $\Delta\phi$  increments for maximum stable values of the ratio  $\Delta\xi/\Delta\phi$  should be near  $\Delta\theta$  and 6.5 times  $\Delta\theta$  for the wedge and cone tip regions respectively.

The number of grid points in the  $\theta$  direction was set at 20 with the  $\Delta\theta$  increment chosen such that approximately 7 points are on the free stream side of the shock wave in the 2-D region of the flow field. The remaining grid points are in the shock layer region and sublayer.

The  $\Delta\phi$  increments for the upper and lower wedge regions were chosen such that 10 grid points exist in each  $\theta = \text{constant}$  plane. At least 4 are outside the tip Mach cone and, as a result, in the 2-D region of the flow field. The  $\Delta\phi$  increment for the cone tip region is chosen such that 13 grid points exist in each  $\theta = \text{constant}$  plane, 2 of which are common to the upper and lower wedge regions.

The resulting computational plane grid system, similar to that depicted in Figure 23, has dimensions 20 by 31 which allowed reasonable solution convergence times. The numerical values associated with the  $\Delta\theta$  and  $\Delta\phi$  are given in Table 1 for the two conditions investigated.

It is noted upon examination of the numerical values for

Table 1. Computational plane grid spacing for the forebody flow region

	Upper wedge		Cone tip		Lower wedge	
	$\alpha = 0^\circ$	$\alpha = 4^\circ$	$\alpha = 0^\circ$	$\alpha = 4^\circ$	$\alpha = 0^\circ$	$\alpha = 4^\circ$
$\Delta\phi$ (radians)	0.1165	0.1046	0.2618	0.2618	0.1165	0.1301
$\Delta\theta$ (radians)	0.04434	0.04470	0.04434	0.04470	0.04434	0.04470

the angular increments that the conditions for maximizing the mesh ratios are nearly satisfied. The worst violation occurs in the  $\Delta\phi$  increment for the upper and lower regions which are about 2.5 times larger than the desired values. Decreasing the increments to their proper values, however, would require excessive grid points from a computation time viewpoint. Since no shock waves are encountered in the  $\phi$  direction, operation at the lower mesh ratios in these regions should not be prohibitive.

#### Solution technique

The integration is initiated in the  $\xi = 1$  plane and proceeds 20 steps in the  $\xi$  direction at which place the solution is checked for convergence. If convergence has not been achieved the process is repeated until a solution is established. The increment  $\Delta\xi$  is

chosen as large as possible without exceeding the stability bound which is determined experimentally by simply increasing  $\Delta\xi$  until divergence occurs.

In each  $\xi = \text{constant}$  plane (see Figure 23) the integration proceeds from the body surface to the free stream boundary and from the upper 2-D wedge boundary spanwise along the wing, around the cone tip and to the lower surface 2-D wedge boundary.

Care must be taken in the integration process at the grid points in the wedge-cone interface planes since the equations of motion for the wedge proper and cone are not the same. Since the MacCormack predictor uses forward differences, the cone equations are used for the prediction step in the upper surface interface plane while the wedge equations are used in the lower surface interface plane. On the other hand, the opposite is true for the corrector step since the corrector utilizes backward differences.

To insure that the predictor differences are always forward and the corrector differences backward the integration steps must always be in the positive directions. In view of the integration process described above, the positive directions for the y and z axes must be reversed in the lower surface wedge region. The only effect this has in the integration process is the reversal of signs associated with the v and w velocity components.

### Forebody numerical solutions

One wing configuration is considered in this study with a forebody wedge half-angle of 7.5 degrees and, as a result, a 7.5 degree tip cone half-angle. The wing chord length is set at 2 units.

The flow fields for a free stream Mach number of 2 are evaluated at angles of attack of 0 and 4 degrees. The 0 degree case is used as a check to see if the numerical technique develops the proper flow field symmetry associated with the upper and lower surface flow regions.

Flow field solutions for both the 0 and 4 degree angles of attack cases were obtained using the grid spacing defined in Table 1. In both cases the near maximum integration step size was used. It was determined by means of a trial and error process. Successively larger increments  $\Delta\xi$  were tried until divergence occurred. The resulting  $\Delta\xi$  increments for the 0 and 4 degree cases were 0.04434 and 0.040 respectively. Table 2 shows the corresponding mesh ratios  $\Delta\xi/\Delta\phi$  and  $\Delta\xi/\Delta\theta$  used to obtain the solutions in the various regions of the forebody flow field. Also tabulated are the theoretical maximums based on the linear one-dimensional theory.

It is noted that the ratio  $\Delta\xi/\Delta\theta$  is always within 80 per cent of the predicted maximum. This procedure should yield a reasonable solution in the shock vicinity. In the cross flow direction the linear stability bound is exceeded in the cone region while on both the upper and lower wedge surfaces the ratio  $\Delta\xi/\Delta\phi$  is between 30 and 40 per cent of the predicted maximum. As expected,

Table 2. Theoretical and experimental mesh ratios used in the forebody solution

	$\Delta\xi/\Delta\theta$			$\Delta\xi/\Delta\epsilon$		
	Theoretical maximum	Value used	Per cent of theoretical maximum	Theoretical maximum	Value used	Per cent of theoretical maximum
$\alpha = 0^\circ$						
Upper wedge	1.017	0.3805	37.4	1.039	1.0	96.25
Tip cone	0.1571	0.1693	107.8	1.110	1.0	90.1
Lower wedge	1.017	0.3805	37.4	1.039	1.0	96.25
$\alpha = 4^\circ$						
Upper wedge	0.9793	0.3825	39.1	1.088	0.895	82.3
Tip cone	0.1250	0.1526	122.1	1.111	0.895	80.6
Lower wedge	0.9430	0.3075	32.61	1.057	0.895	84.7

increasing the increment  $\Delta\xi$  causes instabilities in the crossflow direction in the cone region.

The  $\alpha = 0^\circ$  normal pressure distributions (normal to the wing chord plane) at various spanwise points in the mid-chord plane are shown in Figures 25 and 26 for the upper and lower wedge regions respectively. Figures 27 and 28 depict normal pressure distributions in various meridian planes about the tip cone. The index parameter  $k$  defines the angular location of the  $\phi = \text{constant}$  planes in all regions. Figure 29 shows the relative location of the planes corresponding to the 31  $k$  values. The index parameter  $j$  defines the angular location of the  $\theta = \text{constant}$  surfaces common to all regions. Table 3 lists the numerical values for  $\theta$  and  $\phi$  in all regions for both angles of attack considered.

The distributions appear to be smooth with the bow shock appearing in each distribution. It is quite well defined and usually contained in one to two intervals. As noted in Figure 30, the shock wave lies nearer the wing surface in the cone region. In the 2-D wedge region the bow shock is at an angle of 36.71 degrees with respect to the wedge center line which decreases to 30.5 degrees in the cone region at the plane of symmetry ( $k = 16$ ). The shock strength decreases from the wedge region to the cone region.

The spanwise distribution of pressure along the body surface is shown in Figure 31. The body pressures decrease from the 2-D upper wedge value of 0.137 to a near constant value of about 0.1145 around the cone surface then increases again to 0.137 at the lower

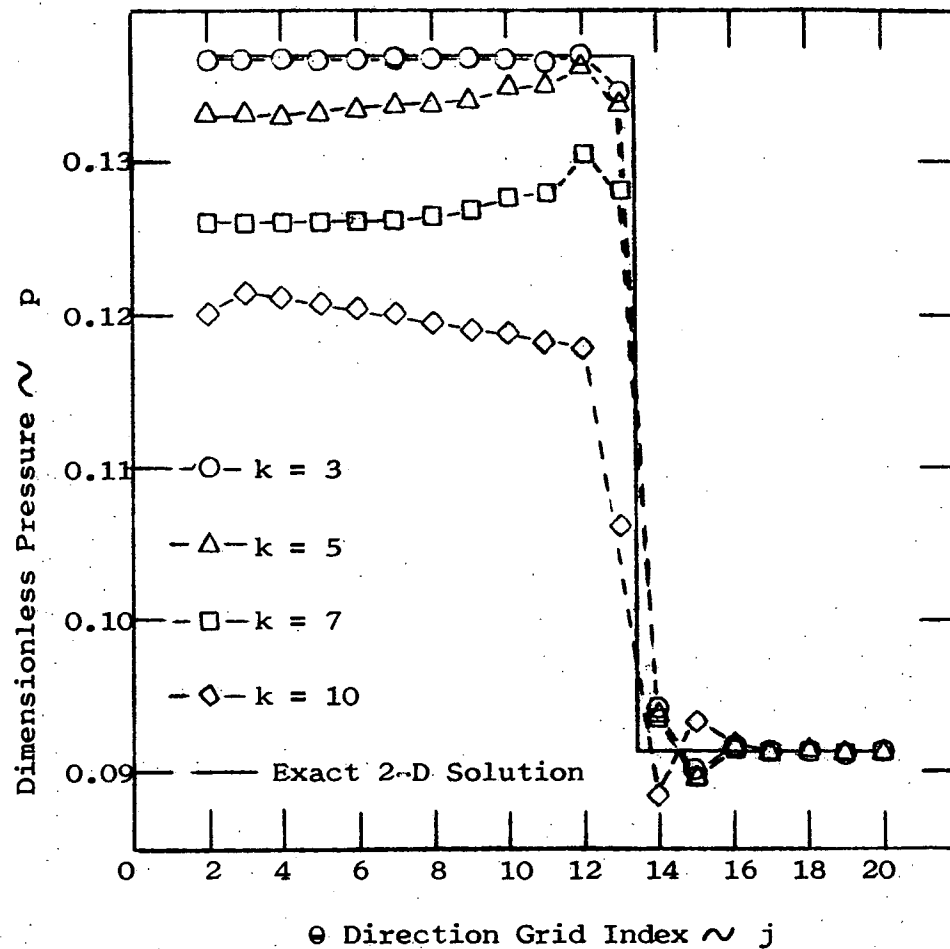


Figure 25. Forebody upper wedge region normal pressure distributions for the  $\alpha = 0^\circ$  case

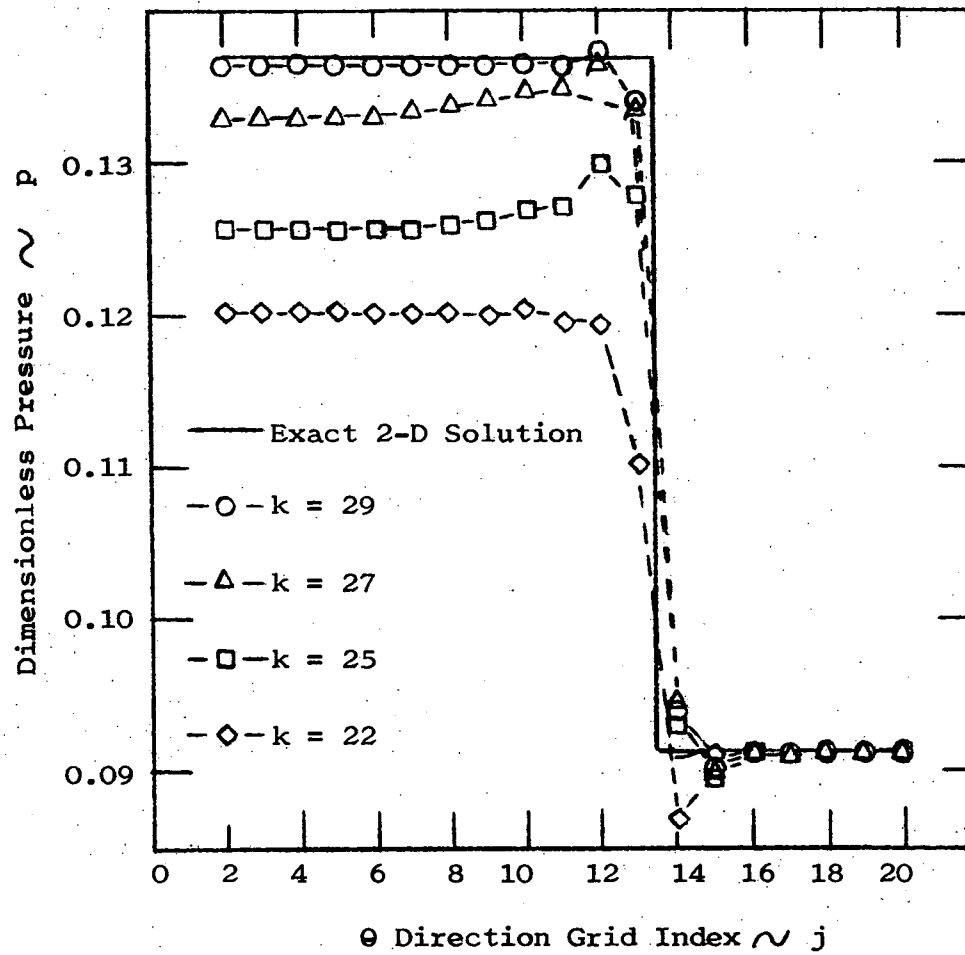


Figure 26. Forebody lower wedge region normal pressure distributions for the  $\alpha = 0^\circ$  case

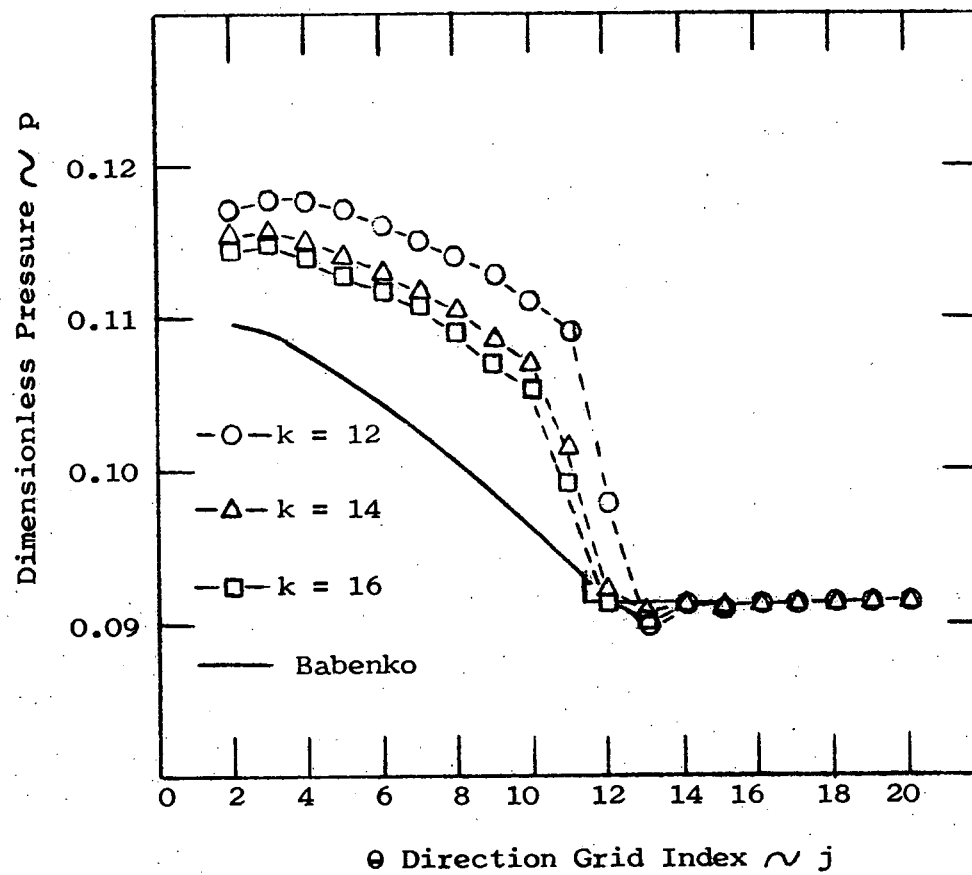


Figure 27. Forebody upper cone region normal pressure distributions for the  $\alpha = 0^\circ$  case

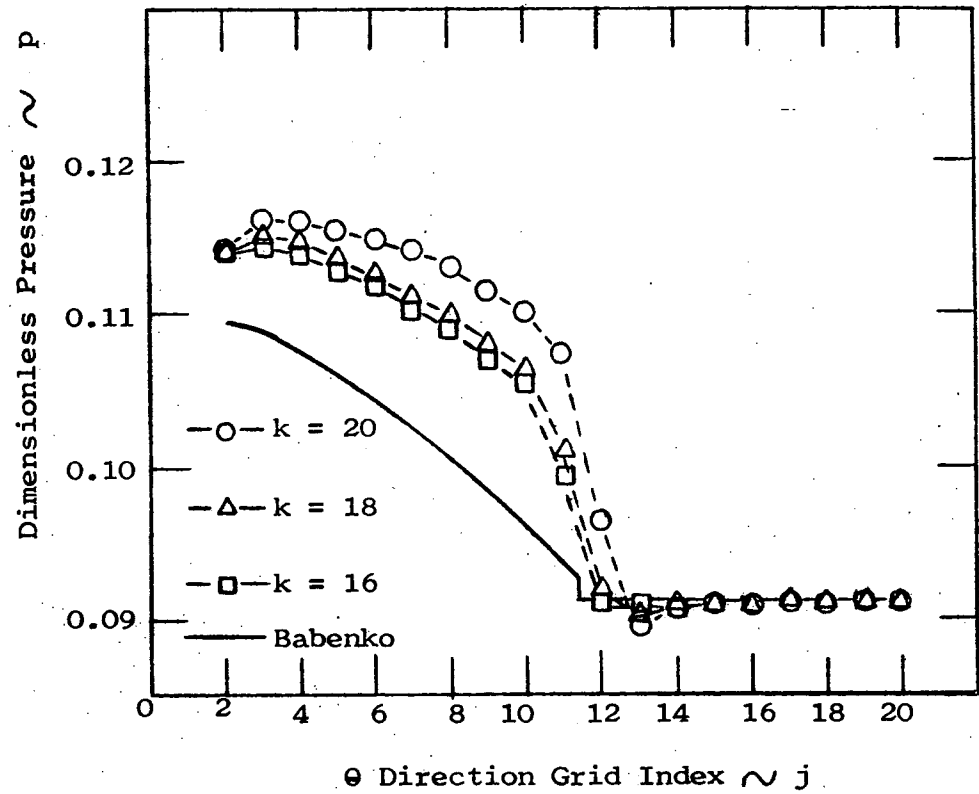


Figure 28. Forebody lower cone region normal pressure distributions for the  $\alpha = 0^\circ$  case.

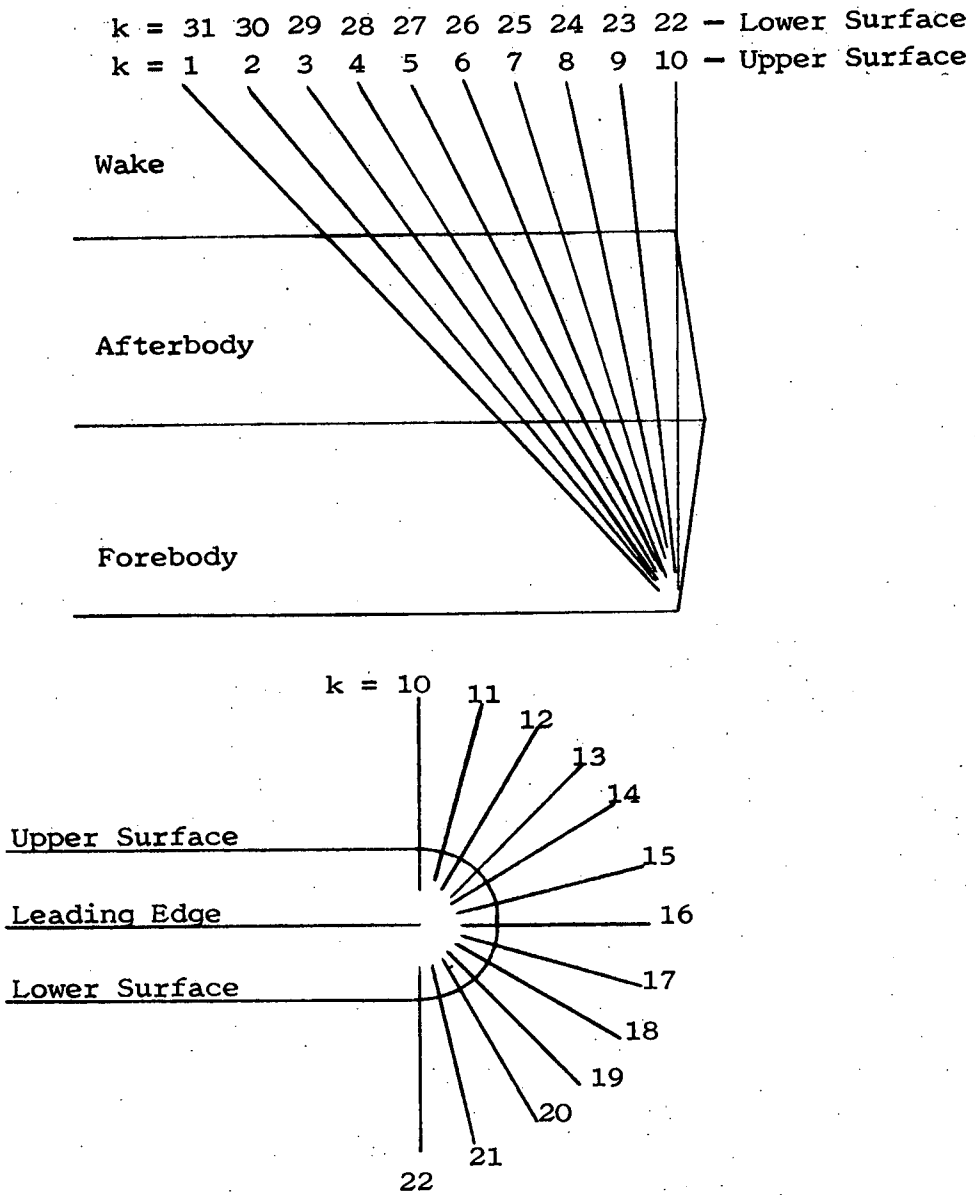


Figure 29. Plan form and frontal view of wing showing the relative location of the  $\phi = \text{constant}$  planes defined by the index parameter  $k$

Table 3. Numerical values for the angular orientations of the  $\theta = \text{constant}$  and  $\phi = \text{constant}$  planes defined by the indicies j and k respectively

k	$\phi$ degrees		j	$\theta$ degrees	
	$\alpha = 0^\circ$	$\alpha = 4^\circ$		$\alpha = 0^\circ$	$\alpha = 4^\circ$
1	-60.07	-53.92	1	5.140	4.939
2	-53.40	-47.93	2	7.500	7.500
3	-46.72	-41.94	3	9.860	10.06
4	-40.05	-35.94	4	12.23	12.62
5	-33.37	-29.95	5	14.59	15.18
6	-26.70	-23.96	6	16.95	17.74
7	-20.02	-17.97	7	19.31	20.30
8	-13.35	-11.98	8	21.68	22.86
9	-6.670	-5.990	9	24.04	25.42
10	0	0	10	26.40	27.99
11	15.0	15.0	11	28.77	30.54
12	30.0	30.0	12	31.13	33.11
13	45.0	45.0	13	33.49	35.67
14	60.0	60.0	14	38.85	38.23
15	75.0	75.0	15	38.21	40.79
16	90.0	90.0	16	40.58	43.35
17	105.0	105.0	17	42.94	45.91
18	120.0	120.0	18	45.31	48.47
19	135.0	135.0	19	47.66	51.03
20	150.0	150.0	20	50.03	53.60
21	165.0	165.0			
22	180.0	180.0			
23	-6.67	-7.450			
24	-13.35	-14.91			
25	-20.02	-22.36			
26	-26.70	-29.81			
27	-33.37	-37.27			
28	-40.05	-44.72			
29	-46.72	-52.17			
30	-53.40	-59.63			
31	-60.07	-67.08			

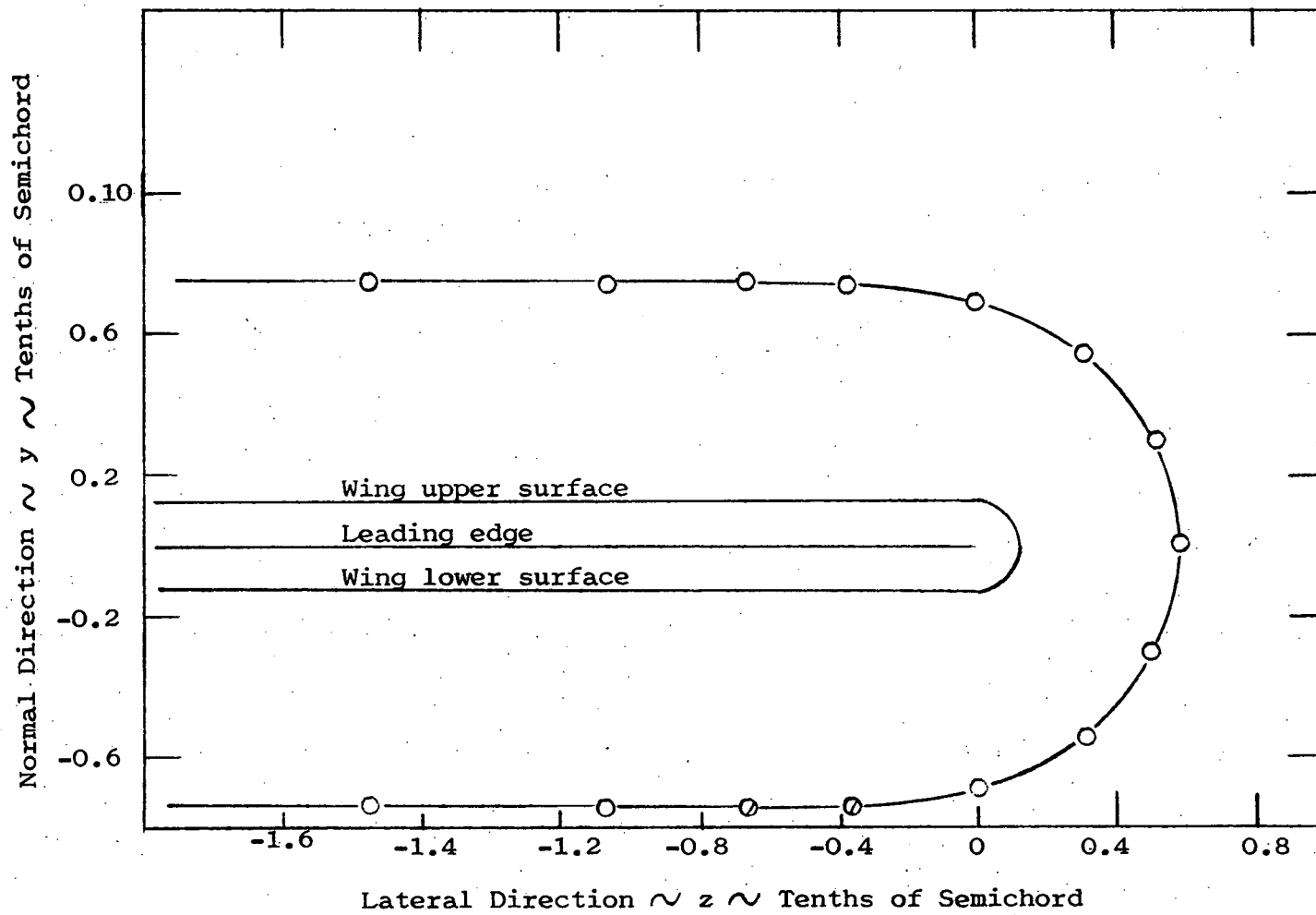


Figure 30. Forebody bow shock shape in the  $\xi = 1.0$  plane for the  $\alpha = 0^\circ$  case

2

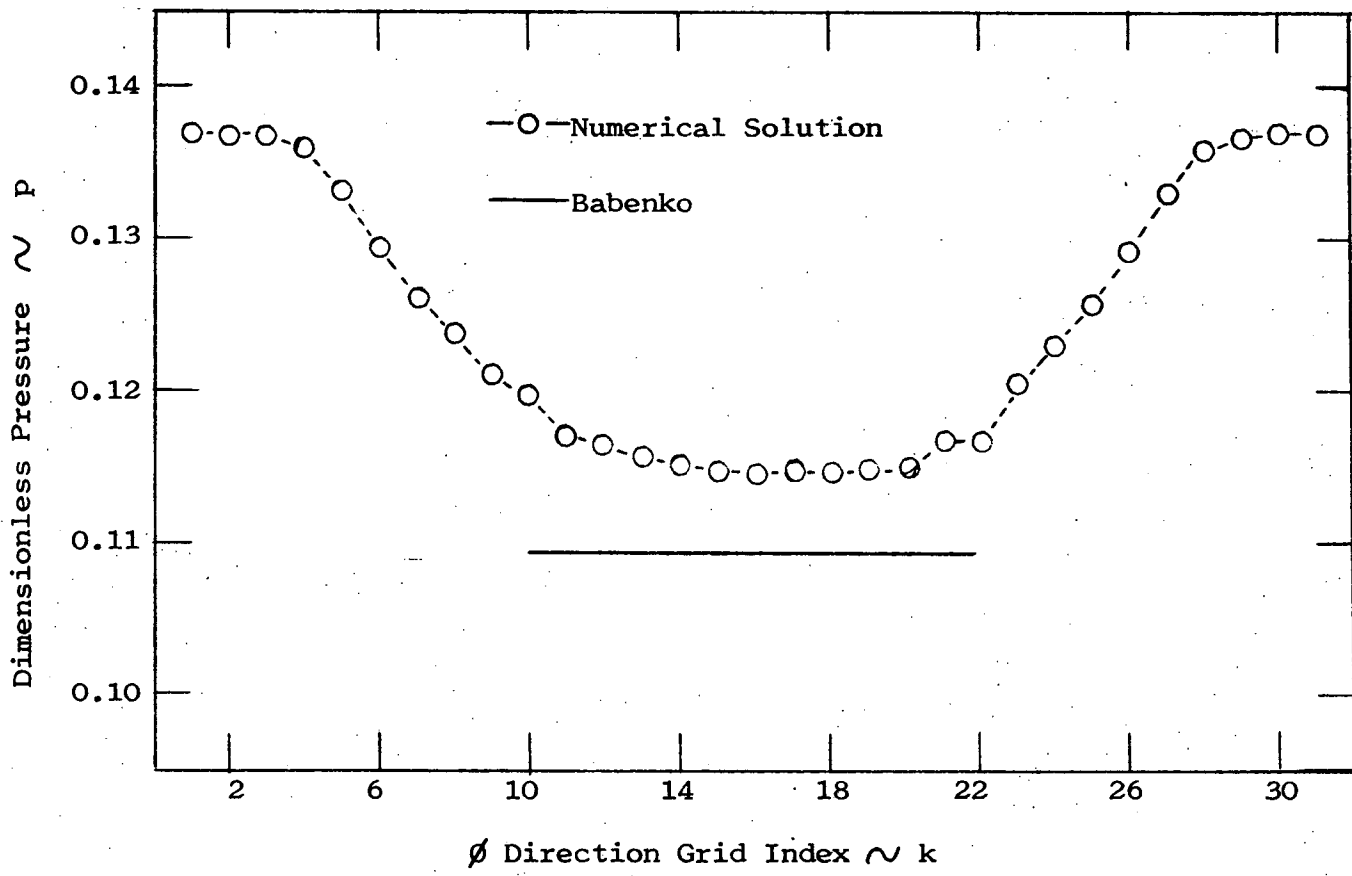


Figure 31. Forebody lateral body surface pressure distribution for the  $\alpha = 0^\circ$  case

wedge 2-D region. Slight pressure oscillations occur along the body surface near the wedge-cone interface planes probably caused by the large values of the mesh ratio  $\Delta\xi/\Delta\phi$ . These are the regions in which crossflow instabilities occur when the  $\Delta\xi$  increment is increased.

In an attempt to demonstrate the reliability of the numerical technique used in this study, a comparison is made with flow fields developed by Babenko<sup>(27)</sup> for a circular cone with a half-angle of 7.5 degrees at a Mach number of 2 at zero degrees angle of attack. The normal pressure distribution in the 90 degree meridian plane is plotted in Figures 27 and 28. The body surface distribution (which is constant) plotted around the cone surface from the 0 to the 180 degree meridional planes is shown in Figure 31. The normal distributions in the 90 degree meridian plane as well as the body surface distribution for both the wedge-cone and the Babenko cone are similar in form with the numerical pressure values associated with the latter somewhat smaller. This is to be expected since the bow shocks associated with wedge shaped bodies are stronger than those associated with those of cones having the same vertex angle.

In general, the numerical technique appears to generate the required flow field symmetry for the zero angle of attack case.

The  $\alpha = 4^\circ$  normal pressure distributions at various spanwise locations on the upper and lower wedge surfaces are shown in Figures 32 and 33 respectively. The distributions for the tip cone region in various meridional planes are depicted in Figures 34 and 35.

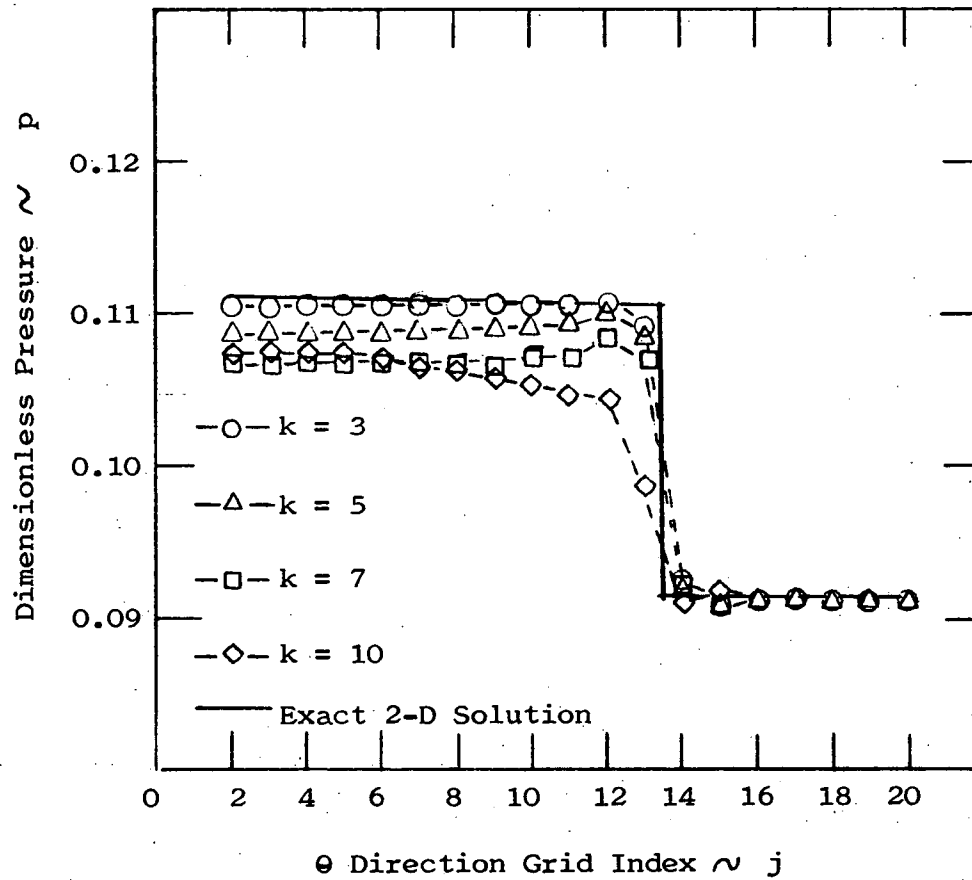


Figure 32. Forebody upper wedge region normal pressure distributions for the  $\alpha = 4^\circ$  case

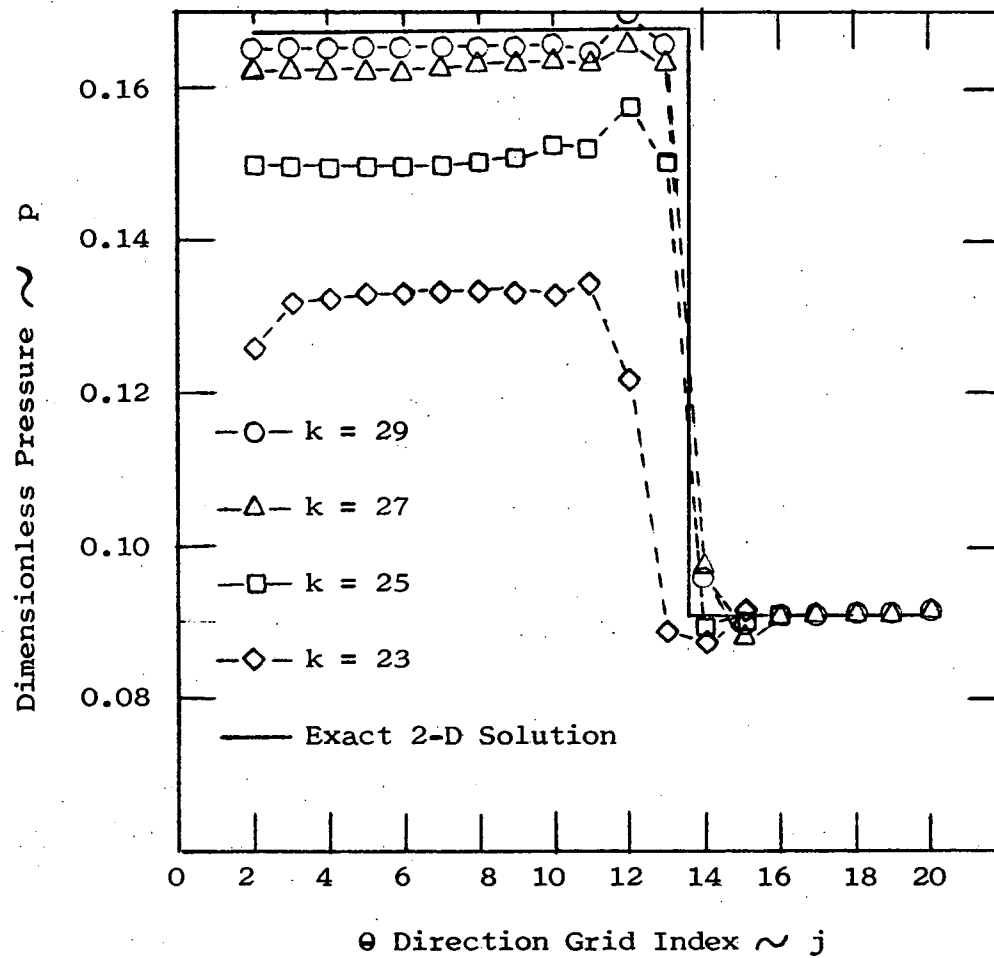


Figure 33. Forebody lower wedge region normal pressure distributions for the  $\alpha = 4^\circ$  case.

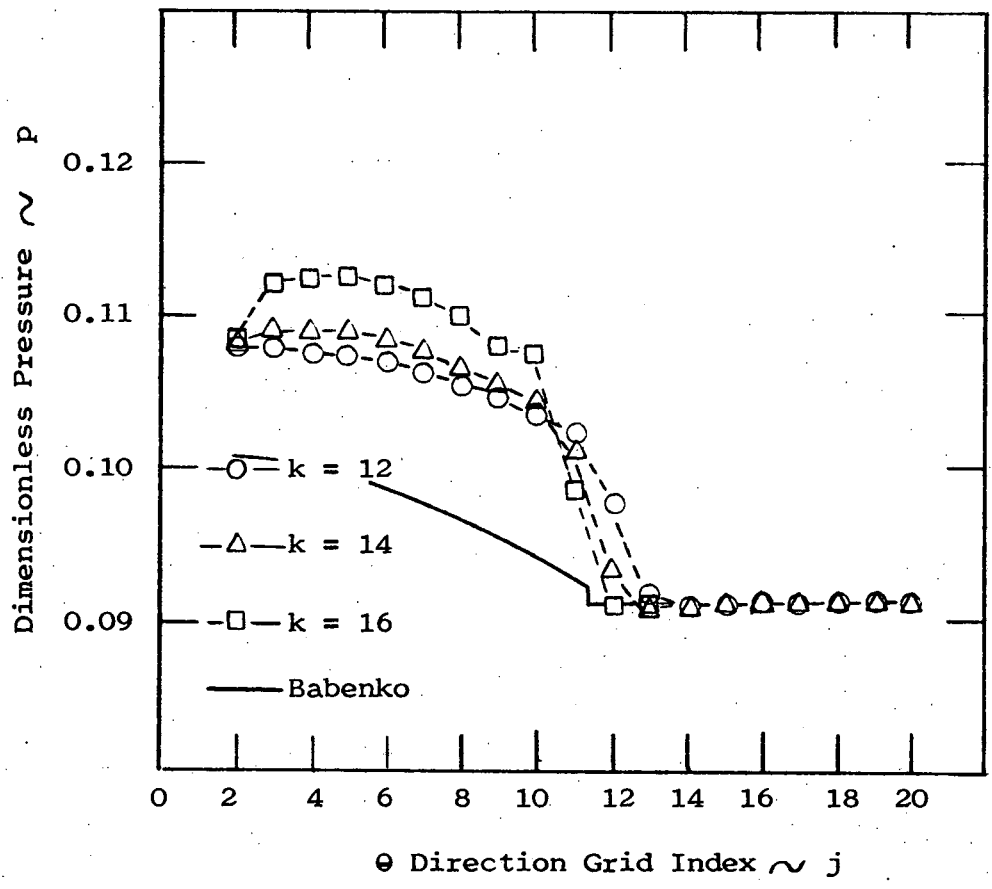


Figure 34. Forebody upper cone region normal pressure distributions for the  $\alpha = 4^\circ$  case

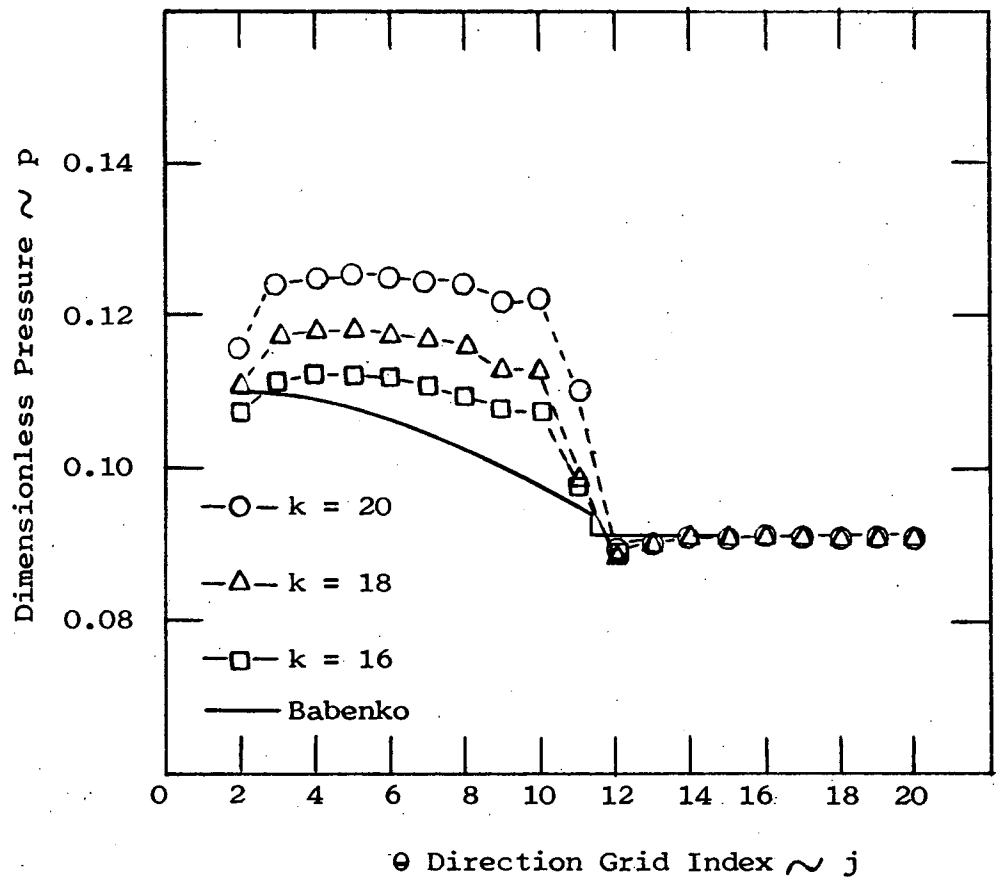


Figure 35. Forebody lower cone region normal pressure distributions for the  $\alpha = 4^\circ$  case

Again the distributions are very smooth with a well defined bow shock contained in one to two intervals.

The normal pressure distribution in the 90 degree meridional plane ( $k = 16$ ) for the Babenko cone at a 4 degree angle of attack is included in Figures 34 and 35. As expected, the pressures in the Babenko cone flow field are generally less than in the wedge-cone field.

The shock shape in the  $\xi = 1$  plane for  $\alpha = 4^\circ$  is shown in Figure 36. The shock angles with respect to the wedge center line in the upper and lower 2-D wedge regions have numerical values 36.95 and 37.0 degrees respectively. In the cone region the bow shock lies generally near the body surface with the smallest center line shock angle (29.5 degrees) occurring in the  $\phi = 113$  degree meridional plane on the lower surface. It is noted that the shock shapes for the  $\alpha = 0^\circ$  and  $\alpha = 4^\circ$  cases are quite similar.

Although the center line shock angles in the upper and lower wedge regions are very nearly the same, the corresponding shock strengths are quite different as noted in the lateral body surface pressure distributions depicted in Figure 37. The surface pressure associated with the weaker upper surface shock is 0.1108 which decreases only slightly around the cone then increases to 0.1681 in the lower 2-D wedge region containing the stronger bow shock. The slight pressure oscillations experienced in the  $\alpha = 0^\circ$  case near the wedge-cone interface planes also appear in the  $\alpha = 4^\circ$  data.

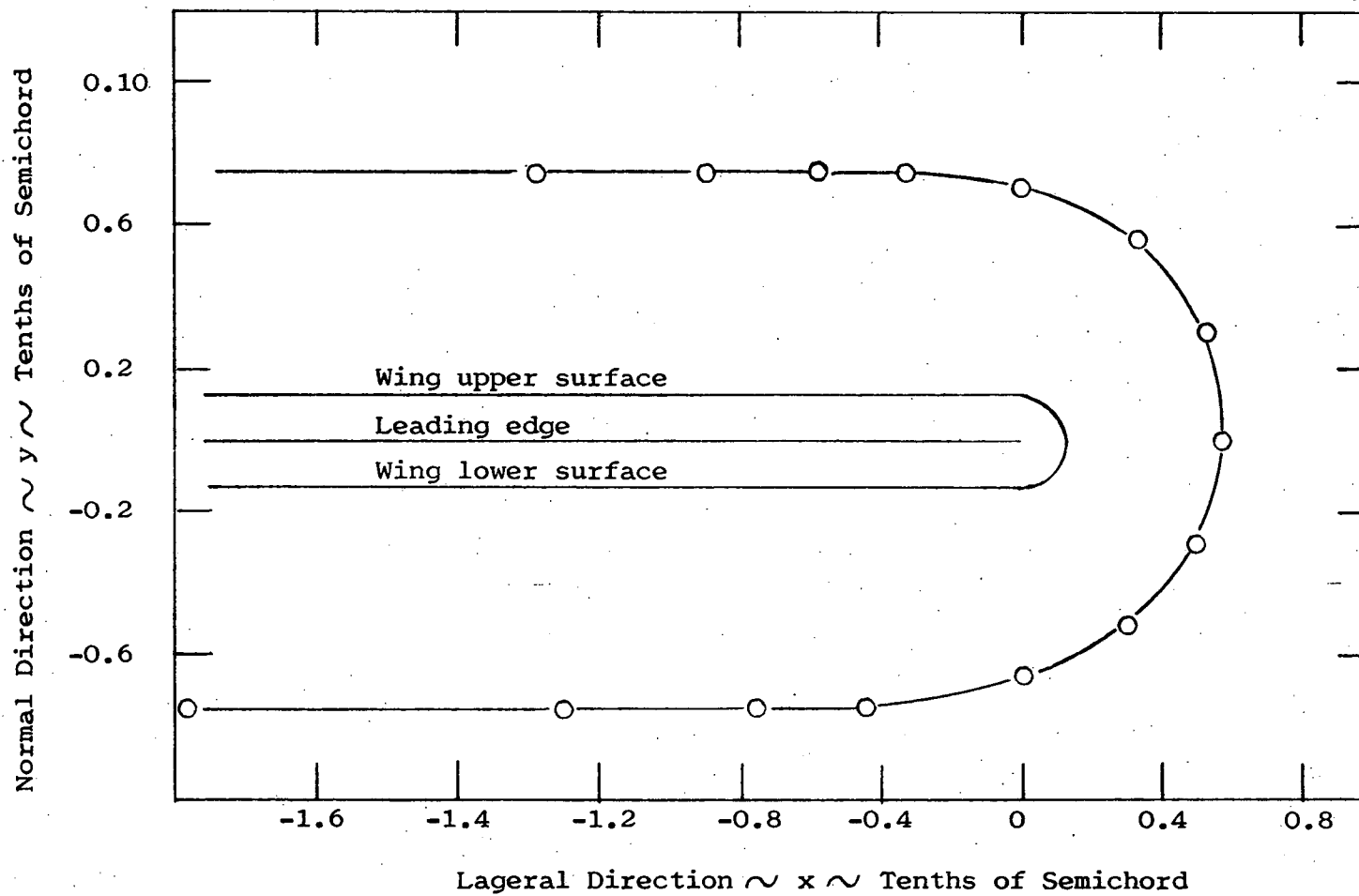


Figure 36. Forebody bow shock shape in the  $\xi = 1.0$  plane for the  $\alpha = 4^\circ$  case

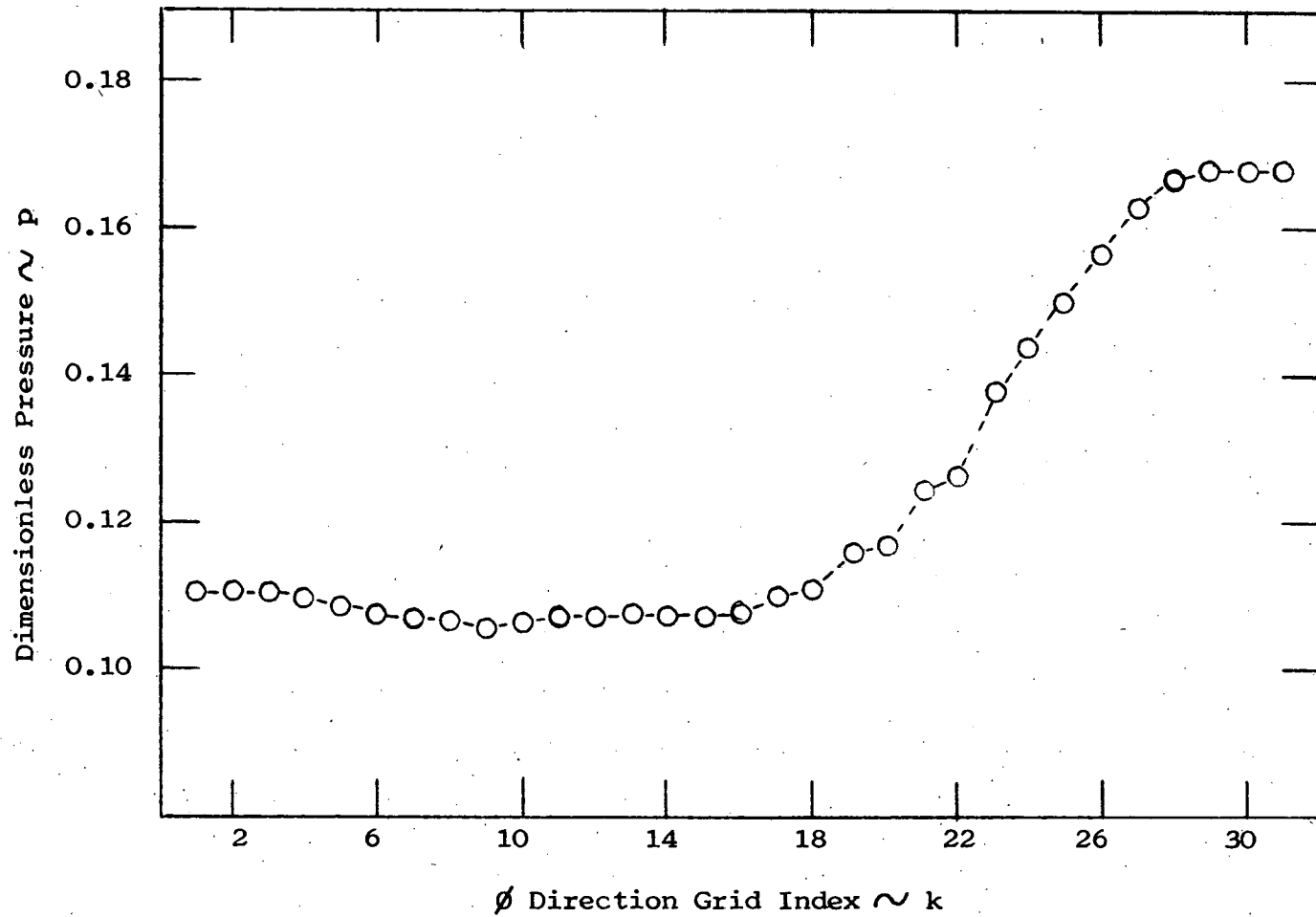


Figure 37. Forebody surface pressure distribution in the  $\xi = 1$  plane for the  $\alpha = 4^\circ$  case

## Region II Flow Field Analysis

### Afterbody geometry and coordinate systems

That portion of the body contained between the mid-chord point and the trailing edge of the wing constitutes the afterbody which is a mirror image of the forebody. As with the forebody, the afterbody is separated into two parts. One part consists of the wedge proper and the other part the tip half-cone.

The coordinate systems defining the afterbody tip cone and surrounding region is depicted in Figure 38. The Cartesian system is the same as that for the forebody. The system into which the equations of motion are cast consists of the  $(\xi, \gamma, \phi)$  system. The coordinate  $\phi$  denotes the angular orientation of the meridian plane containing the point  $(\xi, \gamma, \phi)$  and the axis of the tip half-cone. The coordinate  $\gamma$  (measured in the meridian plane) denotes the angle between the wing chord plane and a line in the meridian plane passing through the point  $(\xi, \gamma, \phi)$  and the circle given by

$$y^2 + z^2 = (2 \tan \theta_c)^2 \quad (74)$$

Note that the circle defined by Equation (74) is the intersection of the  $(y, z)$  plane and the extension of the tip cone. The coordinate  $\xi$  represents simply the x position of the point  $(\xi, \gamma, \phi)$ .

The coordinate system used to define the wedge proper portion of the afterbody flow field is depicted in Figure 39. The coordinate  $\gamma$  is the angle between the wing chord plane and the line that

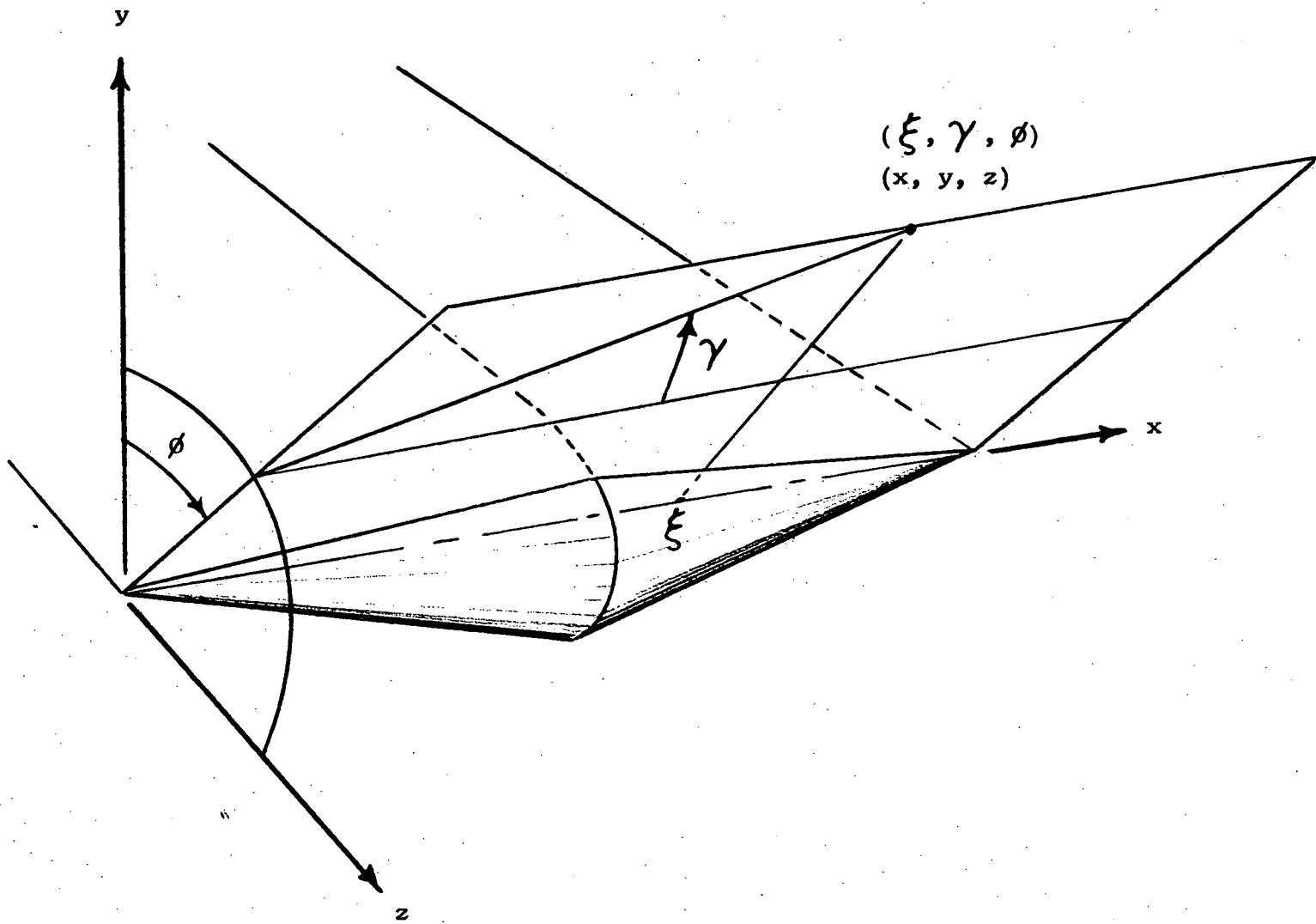


Figure 38. Coordinate system for the afterbody cone flow region

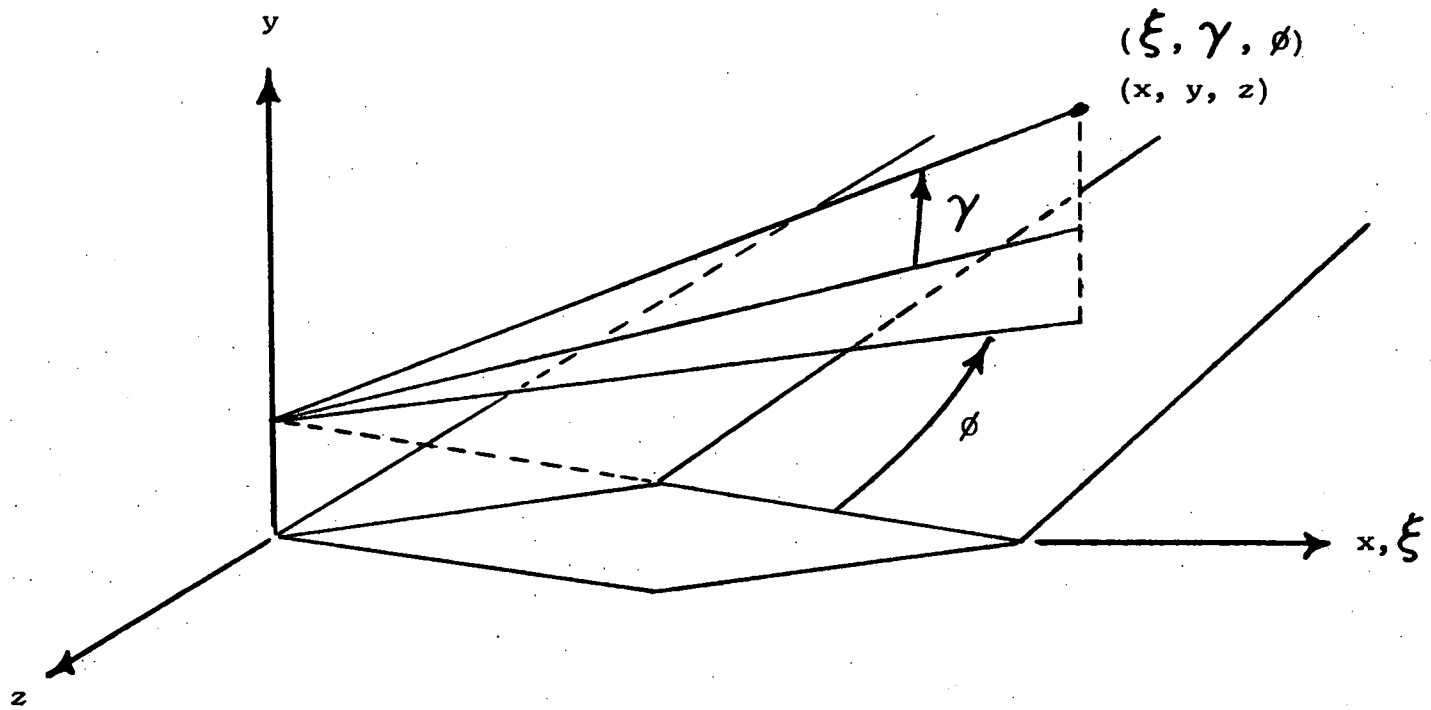


Figure 39. Coordinate system for afterbody wedge region

contains the point  $(\xi, \gamma, \phi)$  and the point  $y = 2 \tan \theta_w$ . The coordinate  $\phi$  represents the angle between the x axis and the plane containing the y axis and the point in question. Again, the coordinate  $\xi$  is simply the x coordinate.

The grid system generated is defined in the tip region by the intersection of a set of  $\phi = \text{constant}$  meridian planes, a set of  $\gamma = \text{constant}$  conical surfaces and a  $\xi = \text{constant}$  plane. In the wedge proper region the grid system is defined by the intersection of a set of  $\gamma = \text{constant}$  wedge planes, a set of  $\phi = \text{constant}$  planes and a  $\xi = \text{constant}$  plane. It is noted that the afterbody surface is represented by a  $\gamma = \text{constant}$  surface, one reason for choosing the particular coordinate systems described. A typical grid network would be similar to that depicted in Figure 23. Once again, the grid points in the wedge-cone interface planes are common to both the wedge and tip half-cone.

#### Afterbody equations of motion

In order to perform the integration in the afterbody region the equations of motion given by Equations (37) must be transformed from the Cartesian form to the  $(\xi, \gamma, \phi)$  system. The transformation is presented in Appendix B.

In the afterbody region the equations of motion for both the wedge proper and the tip half-cone are of the general form

$$\bar{E}'_{\xi} + \bar{F}'_{\gamma} + \bar{G}'_{\phi} + \bar{H}' = 0 \quad (75)$$

The conservative variables  $\bar{E}'$ ,  $\bar{F}'$  and  $\bar{G}'$  and the nonhomogeneous term  $\bar{H}'$  for the wedge proper are given by

$$\begin{aligned}\bar{E}' &= \xi \bar{E} \\ \bar{F}' &= -\sin\gamma \cos\gamma \bar{E} + \cos^2\gamma \bar{F} \\ \bar{G}' &= -\sin\phi \cos\phi \bar{E} + \cos^2\phi \bar{G} \\ \bar{H}' &= (\cos^2\gamma - \sin^2\gamma - 2\sin^2\phi) \bar{E} + 2\sin\phi \cos\phi \bar{G} + 2\sin\gamma \cos\gamma \bar{F}\end{aligned}\quad (76)$$

and for the tip half-cone

$$\begin{aligned}\bar{E}' &= (\xi \tan\gamma + 2\tan\theta_c) \bar{E} \\ \bar{F}' &= -\sin\gamma \cos\gamma \bar{E} + \cos^2\gamma (\cos\phi \bar{F} + \sin\phi \bar{G}) \left( \tan\gamma + \frac{2\tan\theta_c}{\xi} \right) \\ \bar{G}' &= -\bar{F} \sin\phi + \bar{G} \cos\phi \\ \bar{H}' &= -\left( \tan\gamma + \frac{2\tan\theta_c}{\xi} \right) (1 - 2\cos^2\gamma) \bar{E} - 2\cos\gamma \sin\phi (\cos\phi \bar{F} + \sin\phi \bar{G})\end{aligned}\quad (77)$$

As in the forebody case, the variables  $\bar{E}$ ,  $\bar{F}$  and  $\bar{G}$  are the vector conservative variables associated with the Cartesian form of the equations of motion.

#### Evaluation of the gas dynamic variables from conservative variables

The same process is used to obtain the gas dynamic variables in the integration process over the afterbody region as is used in the forebody region. The first of Equations (76) is solved for the vector variable  $\bar{E}$  which is then incorporated in Equations (57) - (61) to evaluate  $v$ ,  $w$ ,  $u$ ,  $\rho$  and  $p$ .

### Boundary conditions

As in the forebody region, the afterbody boundary points must be specified in some fashion since the points along the edges of the grid are not integrated points.

The grid spacing in the  $\gamma$  direction is chosen to be large enough that the outermost of the grid points are always in the free stream outside the shock layer. Hence, the gas dynamic variables along these boundaries are retained at the free stream values.

Two methods are available for the specification of the variables along the 2-D afterbody wedge boundaries. Since the  $\Delta\phi$  increments utilized in the afterbody region are the same as those used in the forebody integration, the boundary grid points as well as those in the three adjacent  $\phi = \text{constant}$  planes are all outside the tip Mach cone and in the 2-D flow region. Hence, the gas dynamic variables at the boundary may be set at the 2-D solution values that are known, a technique that was utilized in the forebody integration.

A reflection technique may also be used at this boundary. The reflection occurs across the  $\phi_2$  plane as shown in Figure 40.

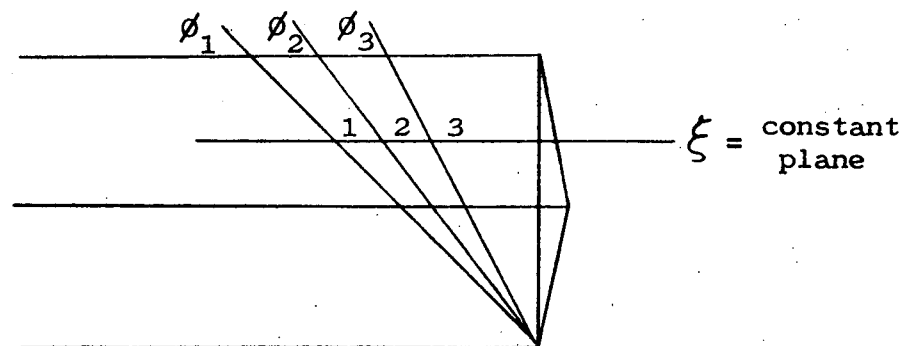


Figure 40. Geometry of the reflection technique

The gas dynamic variables at grid point 1 are set equal to those at grid point 3 as they must be if the points are in the 2-D region of the flow field. In effect, the technique generates its own 2-D solution.

The reflection technique was adopted in this study. It provides a means by which the integration technique can be tested. That is, if the solution in the  $\phi_1$  plane does not correspond to the known 2-D solution, the integration technique is not performing properly.

The boundary conditions along the surface of the afterbody in each  $\xi = \text{constant}$  plane are specified in the same fashion as on the forebody. A sublayer set of grid points is added and the modified Abbett technique is applied at the afterbody surface. It is noted here that the body entropies remain unaltered throughout the expansion at the mid-chord point of the wing. Hence, the entropy values are known from the forebody solution.

#### Initial data

The initial data required to start the afterbody integration are taken from the forebody solution. Since the grid points associated with the forebody and afterbody systems in a specified  $\xi = \text{constant}$  plane do not coincide, point for point, some logical method must be used to transfer the data from the forebody to the afterbody grid system. In this study a scheme is utilized in which the four nearest forebody grid points for each afterbody grid point are located (see Figure 41).

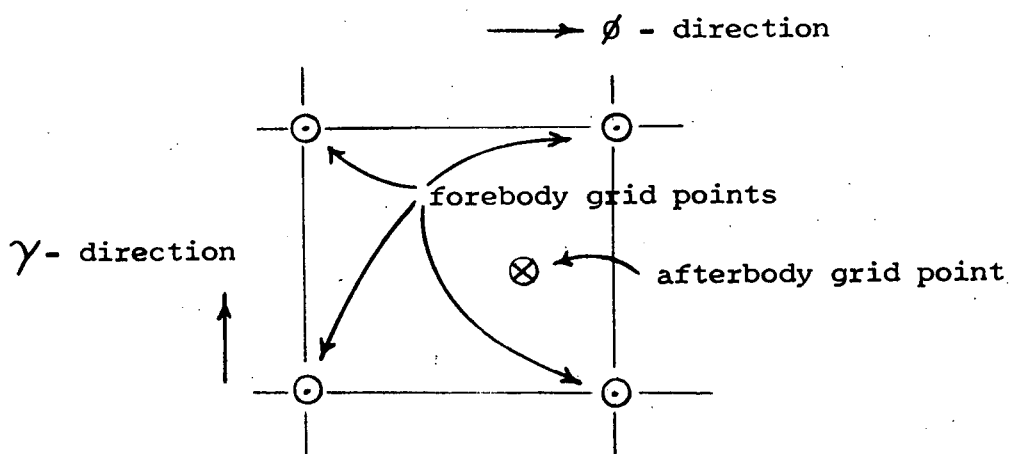


Figure 41. Data transfer technique from the forebody to the afterbody grid

The data are then transferred by means of a simple linear interpolation scheme in both the  $\phi$  direction and  $\gamma$  direction. The specific  $\xi = \text{constant}$  plane in which the data transfer occurs depends upon the particular case under consideration. Even though the data transfer occurs near the mid-chord the exact location of the initial data plane for the afterbody depends upon the step size used in the afterbody integration process.

#### Choice of grid system

The afterbody grid dimensions are established somewhat once the forebody system is defined in that the same  $\Delta\phi$  increments are used. This is to insure that the outer boundary points remain in

the 2-D region of the flow field. The increment  $\Delta\gamma$  is chosen such that at least four grid points always remain in the free stream region outside the shock layer throughout the afterbody region. Numerically, the values associated with  $\Delta\gamma$  for the afterbody and  $\Delta\theta$  for the forebody are very similar in all cases.

### Solution technique

The initial data plane for the afterbody is located such that the first integration step in the  $\xi$  direction contains the mid-chord point at the half-interval. That is, the initial data plane in which the forebody data transfer occurs is located at  $\xi = c/2 - \Delta\xi/2$  where  $\Delta\xi$  is the initial integration step size and  $c$  is the wing chord length. The initial integration step, then, is from the forebody region to the afterbody region. The integration then proceeds along the afterbody to the vicinity of the trailing edge. The magnitude of the integration step size  $\Delta\xi$  is governed by the linear stability criteria.

It was noted in earlier work that the gas dynamic equation coefficient matrices  $A'$  and  $B'$  in the wedge proper region of the afterbody are identical in form to those associated with the forebody. Hence, the same eigenvalues that dictate the maximum mesh ratios in the forebody wedge region now dictate the maximum of  $\Delta\xi/\Delta\theta$  and  $\Delta\xi/\Delta\gamma$  in the afterbody wedge proper region. These eigenvalues remain nearly constant over the afterbody region.

For the tip cone, the eigenvalue structure is quite different in the afterbody region. The maximum eigenvalues for the  $A'$  and  $B'$

matricies are given by Equations (A30) and (A32) respectively. Although the eigenvalues given by Equation (A30) are the same order of magnitude throughout the afterbody region, those defined by Equation (A32) become infinite as the trailing edge is approached. Hence, if constant  $\Delta\xi$  increments based on initial data were used in the integration process one might expect a crossflow instability to develop since the maximum stable value for  $\Delta\xi/\Delta\phi$  decreases rapidly near the trailing edge. In fact, the stable integration step size approaches zero near the trailing edge presenting difficulties in the afterbody integration process.

To insure that the crossflow instability does not occur the increment  $\Delta\xi$  is set equal to the value dictated by the linear stability criteria given in Equations (43) at each step in the integration process. The value  $\Delta\xi$  is given by

$$\Delta\xi = \frac{\Delta\phi_{\text{cone}}}{|\lambda_{B \text{ max}}|} \quad (79)$$

The integration moves quickly initially along the afterbody but slows down radically near the trailing edge. Furthermore, since all other eigenvalues remain nearly constant throughout the afterbody field, one can expect a lower quality flow field solution near the trailing edge as a result of the very suboptimal mesh ratio operation, especially in the vicinity of the shock wave.

### Afterbody numerical solutions

Afterbody solutions are obtained using initial data from both the  $\alpha = 0^\circ$  and  $\alpha = 4^\circ$  forebody solutions at a Mach number of 2.

The grid spacing in each  $\xi = \text{constant}$  plane is quite similar to that of the forebody. The system contains 31 points in the  $\phi$  direction and 20 points in the  $\gamma$  direction. The  $\Delta\phi$  increments for the afterbody region are the same as for the forebody region and are defined in Table 1. The  $\Delta\gamma$  increments, common to all afterbody regions, are 3.0286 degrees and 3.0556 degrees for the  $\alpha = 0^\circ$  and  $\alpha = 4^\circ$  cases respectively. The angular orientation of the various  $\phi = \text{constant}$  planes defined by the index parameter  $k$  are given in Table 3 and the angular orientation of the various  $\gamma = \text{constant}$  planes defined by the index parameter  $j$  are given in Table 4.

An initial integration step size ( $\Delta\xi$ ) of 0.01 is used to move from the forebody region to the afterbody region. Hence, the initial data plane for the afterbody is at  $\xi = 0.995$  with the first integration advancing the data to the  $\xi = 1.005$  plane. The shoulder of the wing ( $\xi = 1.0$ ) occurs at the half-interval of the first integration step.

Subsequent integration step sizes are set to the maximum value dictated by the linear stability analysis given by Equation (79). The resulting numerical values for the mesh ratios  $\Delta\xi/\Delta\phi$  and  $\Delta\xi/\Delta\gamma$  are given in Tables 5 and 6. Included in the tables are the maximum values for the ratios in the various flow field regions as predicted by linear stability theory. Since the cone

Table 4. Angular orientation of the various  $\gamma = \text{constant}$  planes in the afterbody grid system

j	$\gamma$ (degrees)	
	$\alpha = 0^\circ$	$\alpha = 4^\circ$
1	-10.53	-10.56
2	-7.50	-7.50
3	-4.47	-4.44
4	-1.44	-1.39
5	1.59	1.67
6	4.62	4.72
7	7.64	7.78
8	10.67	10.83
9	13.70	13.89
10	16.73	16.95
11	19.76	20.00
12	22.39	23.06
13	25.82	26.11
14	28.84	29.17
15	31.87	32.22
16	34.90	35.28
17	37.93	38.33
18	40.96	41.39
19	43.99	44.44
20	47.02	47.50

Table 5. A comparison of the theoretical maximum values and the actual values of the mesh ratio  $\Delta\xi/\Delta\theta$  used in the afterbody integration

	Theoretical maximum		Value used		Per cent of theoretical maximum	
	$\xi = 0.995$	$\xi = 1.97$	$\xi = 0.995$	$\xi = 1.97$	$\xi = 0.995$	$\xi = 1.97$
Upper wedge ( $\alpha = 0^\circ$ )	1.055	2.185	0.7523	0.0205	71.30	0.940
Tip cone ( $\alpha = 0^\circ$ )	1.129	2.208	0.7523	0.0205	66.60	0.93
Lower wedge ( $\alpha = 0^\circ$ )	1.055	2.185	0.7523	0.0205	71.30	1.16
Upper wedge ( $\alpha = 4^\circ$ )	1.112	1.997	0.7815	0.0397	70.30	1.85
Tip cone ( $\alpha = 4^\circ$ )	1.140	2.011	0.7815	0.0397	68.55	1.97
Lower wedge ( $\alpha = 4^\circ$ )	0.984	2.183	0.7815	0.0397	79.39	1.82

Table 6. A comparison of the theoretical maximum values and the actual values of the mesh ratio  $\Delta\xi/\Delta\theta$  used in the afterbody integration

	Theoretical maximum		Value used		Per cent of theoretical maximum	
	$\xi = 0.995$	$\xi = 1.97$	$\xi = 0.995$	$\xi = 1.97$	$\xi = 0.995$	$\xi = 1.97$
Upper wedge ( $\alpha = 0^\circ$ )	1.015	1.933	0.3414	0.00932	33.64	0.48
Tip cone ( $\alpha = 0^\circ$ )	0.1519	0.00415	0.1519	0.00415	100.0	100.0
Lower wedge ( $\alpha = 0^\circ$ )	1.015	1.933	0.3414	0.00932	33.64	0.480
Upper wedge ( $\alpha = 4^\circ$ )	1.098	1.904	0.3986	0.02024	36.30	1.060
Tip cone ( $\alpha = 4^\circ$ )	0.1592	0.00808	0.1592	0.00808	100.0	100.0
Lower wedge ( $\alpha = 4^\circ$ )	1.053	2.174	0.3204	0.01627	30.43	0.750

cross flow eigenvalues vary extensively throughout the integration, the tables include values in the initial data plane ( $\xi = 0.995$ ) as well as the final integration plane ( $\xi = 1.97$ ).

As noted in Table 5, the ratio  $\Delta\xi/\Delta\gamma$  decreases from about 70 per cent of its theoretical maximum initially to about 1 per cent near the trailing edge in order to satisfy the crossflow stability criteria. Hence, one can expect the flow field solution to degenerate somewhat in the vicinity of the shock as the trailing edge is approached.

Normal pressure distributions at various spanwise locations on both the upper and lower wing surfaces at three different  $\xi =$  constant locations along the afterbody chord are presented in Figures 42 - 65. In particular, Figures 42 - 53 depict the normal pressure distributions for the  $\alpha = 0^\circ$  angle of attack case in the  $\xi = 1.2$ , 1.5 and 1.76 planes along the afterbody. Figures 54 - 65 depict the normal pressure distributions for the  $\alpha = 4^\circ$  angle of attack in the  $\xi = 1.25$ , 1.5 and 1.76 planes. The relative locations of the points on the wing surface (defined by the index parameter  $k$ ) at which the normal distributions are displayed can be obtained in Figure 29 with the exact locations defined in Table 3.

The exact 2-D solution for a symmetric double wedge afterbody is included on each set of upper and lower wedge surface pressure distributions. The exact solutions are used as the standard with which the numerical solutions in the 2-D region ( $k = 3$ ) are compared to test the behavior of the numerical technique.

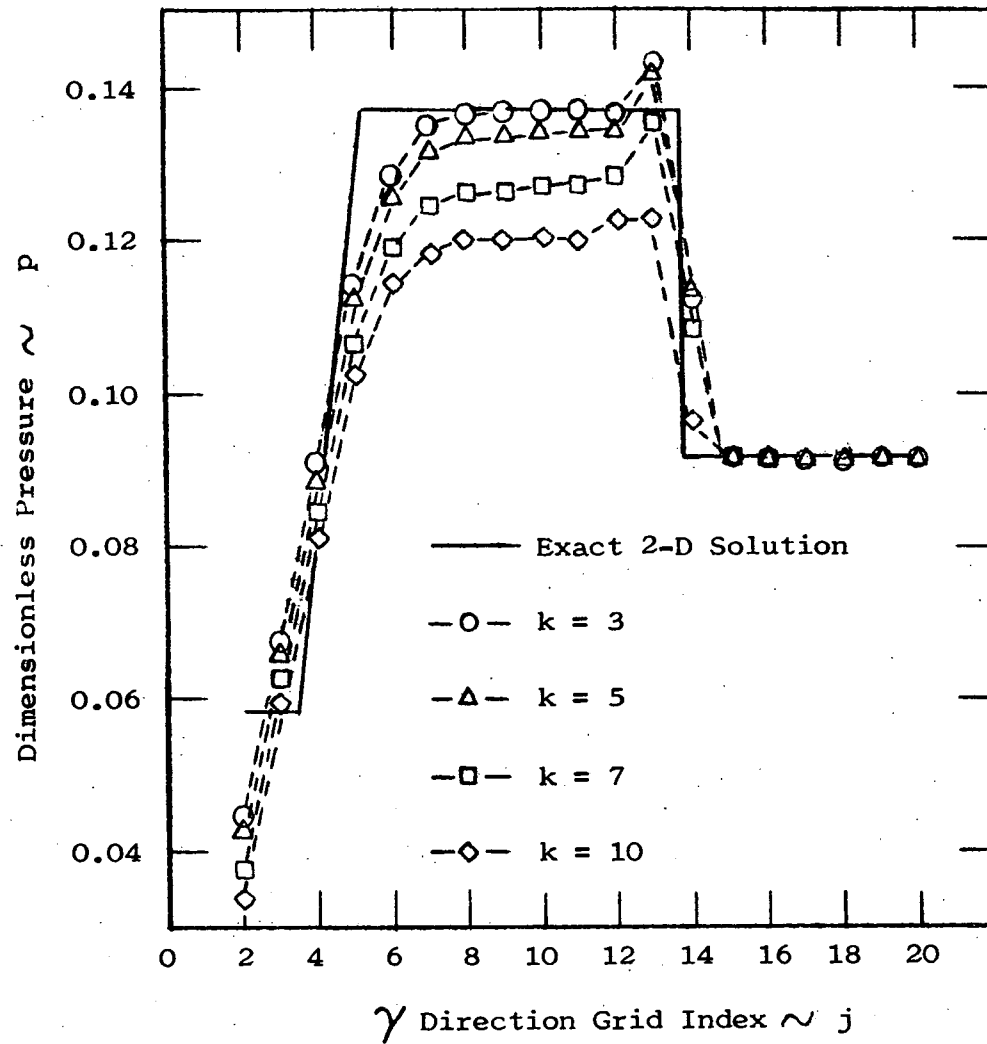


Figure 42. Afterbody upper wedge normal pressure distribution in the  $\xi = 1.2$  plane for the  $\alpha = 0^\circ$  case

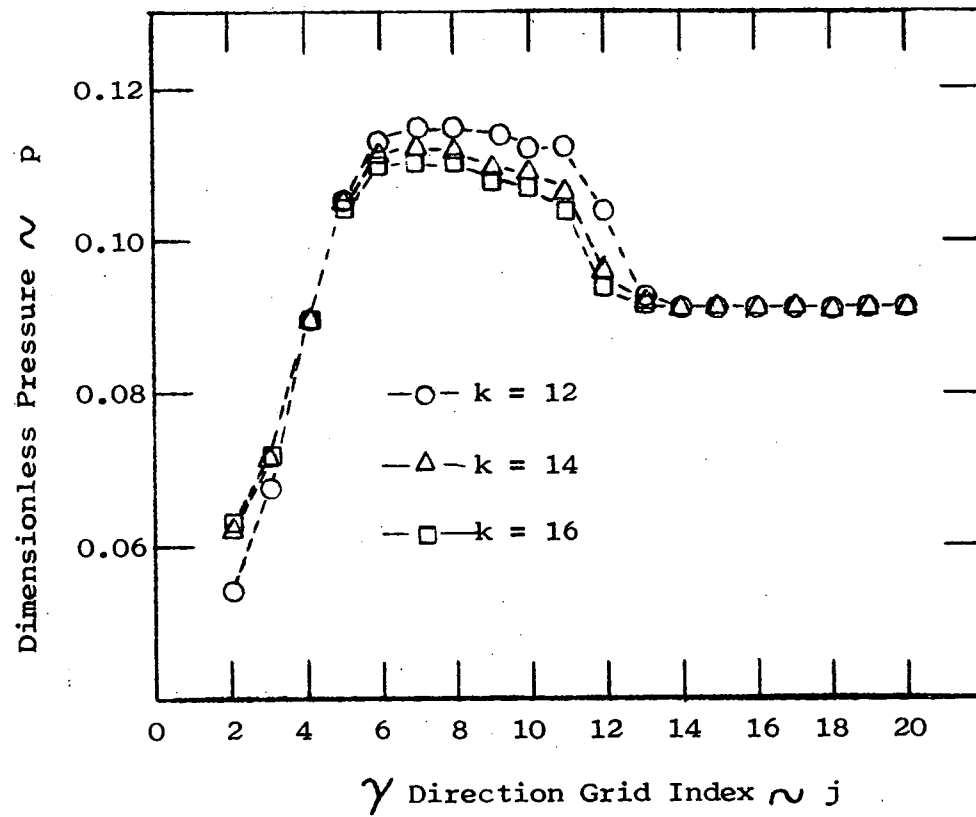


Figure 43. Afterbody upper cone region normal pressure distribution in the  $\xi = 1.2$  plane for the  $\alpha = 0^\circ$  case

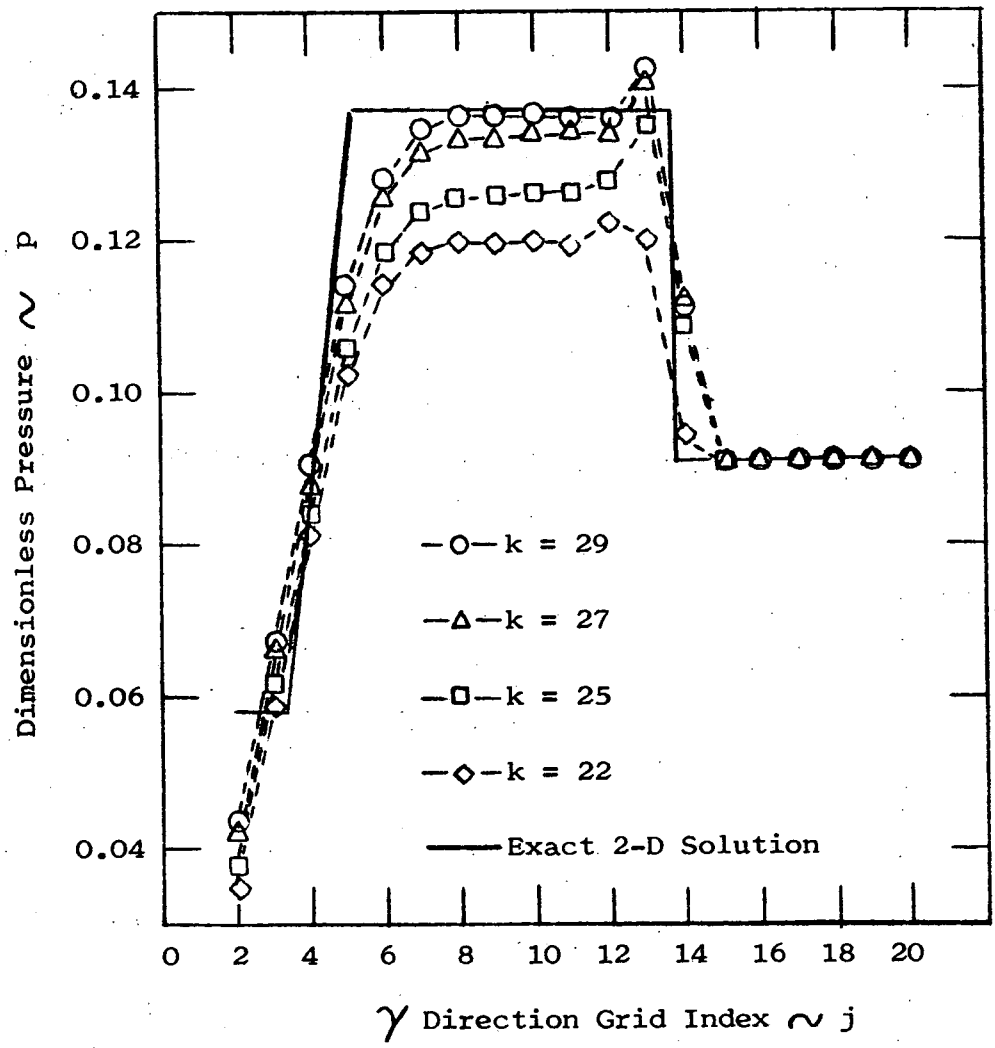


Figure 44. Afterbody lower wedge region normal pressure distribution in the  $\xi = 1.2$  plane for the  $\alpha = 0^\circ$  case

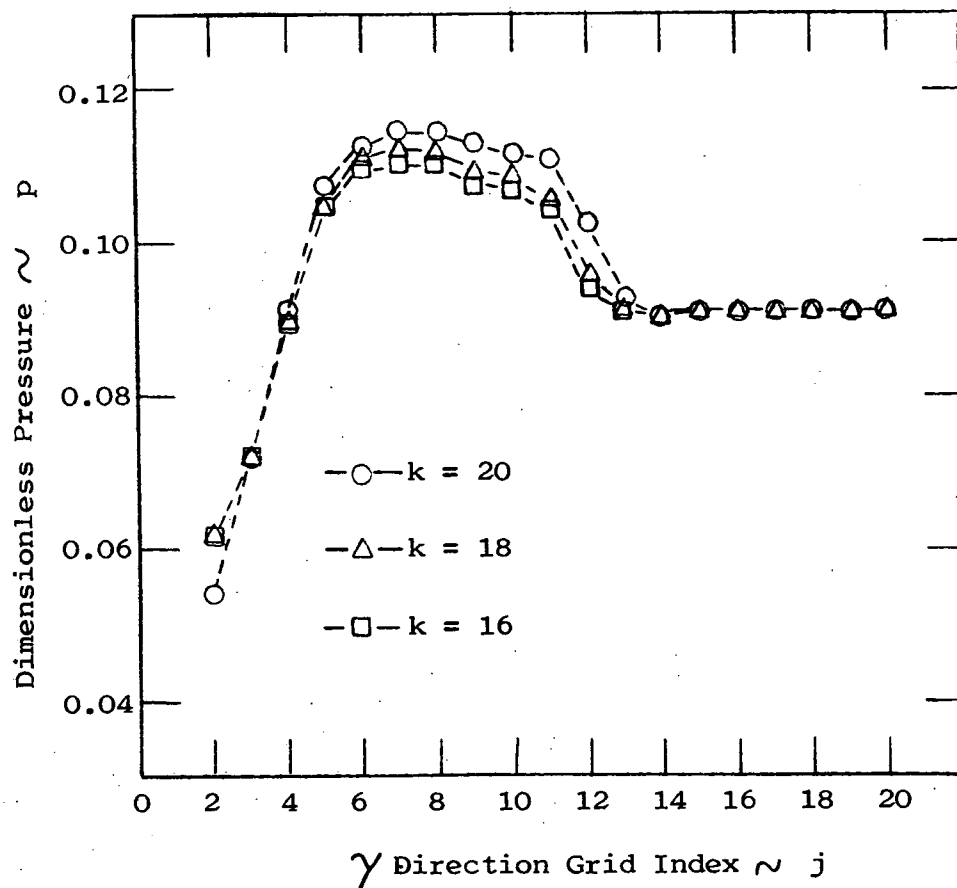


Figure 45. Afterbody lower cone region normal pressure distribution in the  $\xi = 1.2$  plane for the  $\alpha = 0^\circ$  case

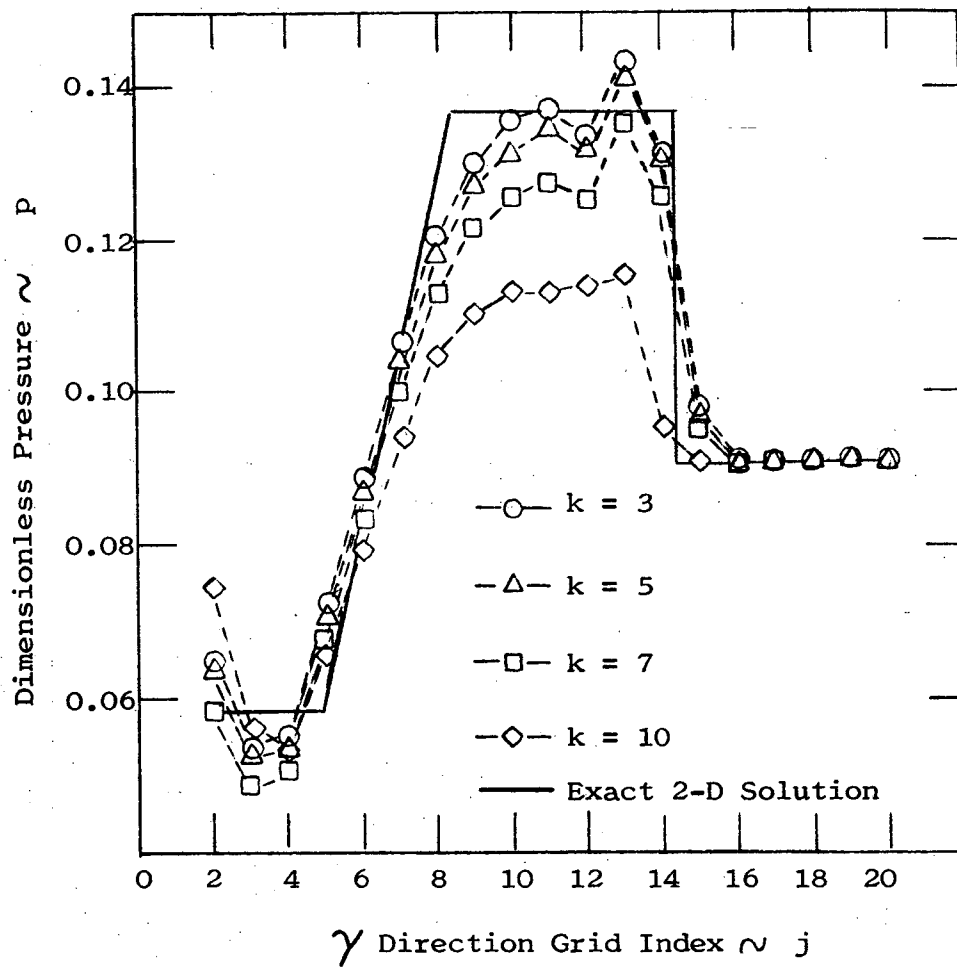


Figure 46. Afterbody upper wedge region normal pressure distribution in the  $\xi = 1.5$  plane for the  $\alpha = 0^\circ$  case

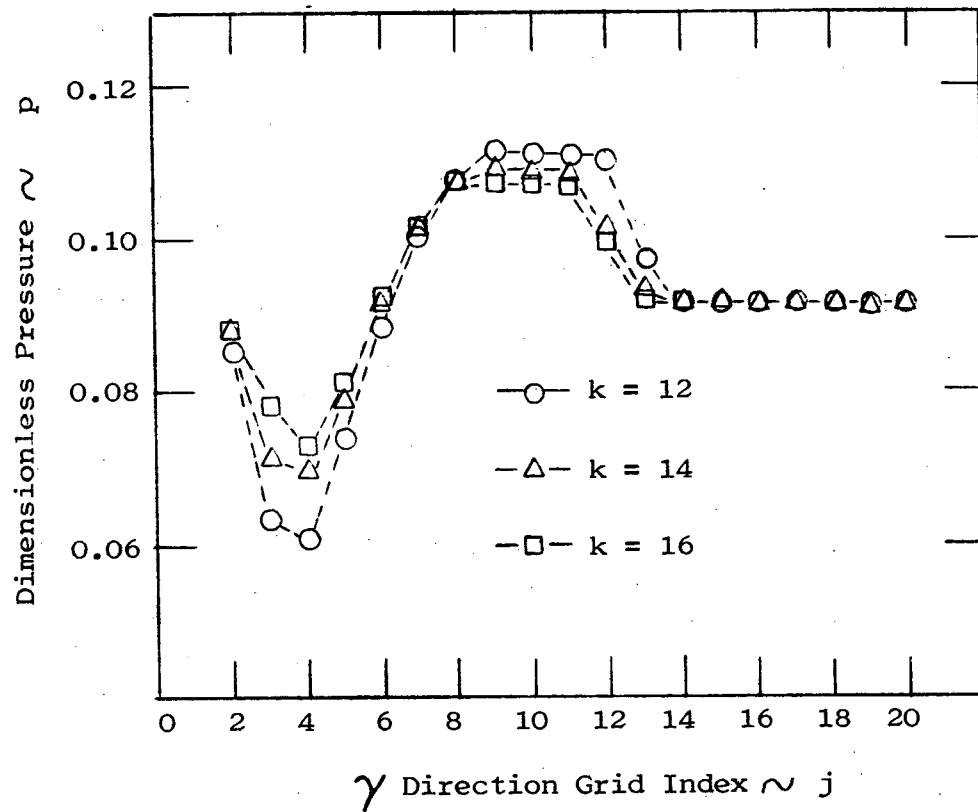


Figure 47. Afterbody upper cone region normal pressure distributions in the  $\xi = 1.5$  plane for the  $\alpha = 0^\circ$  case

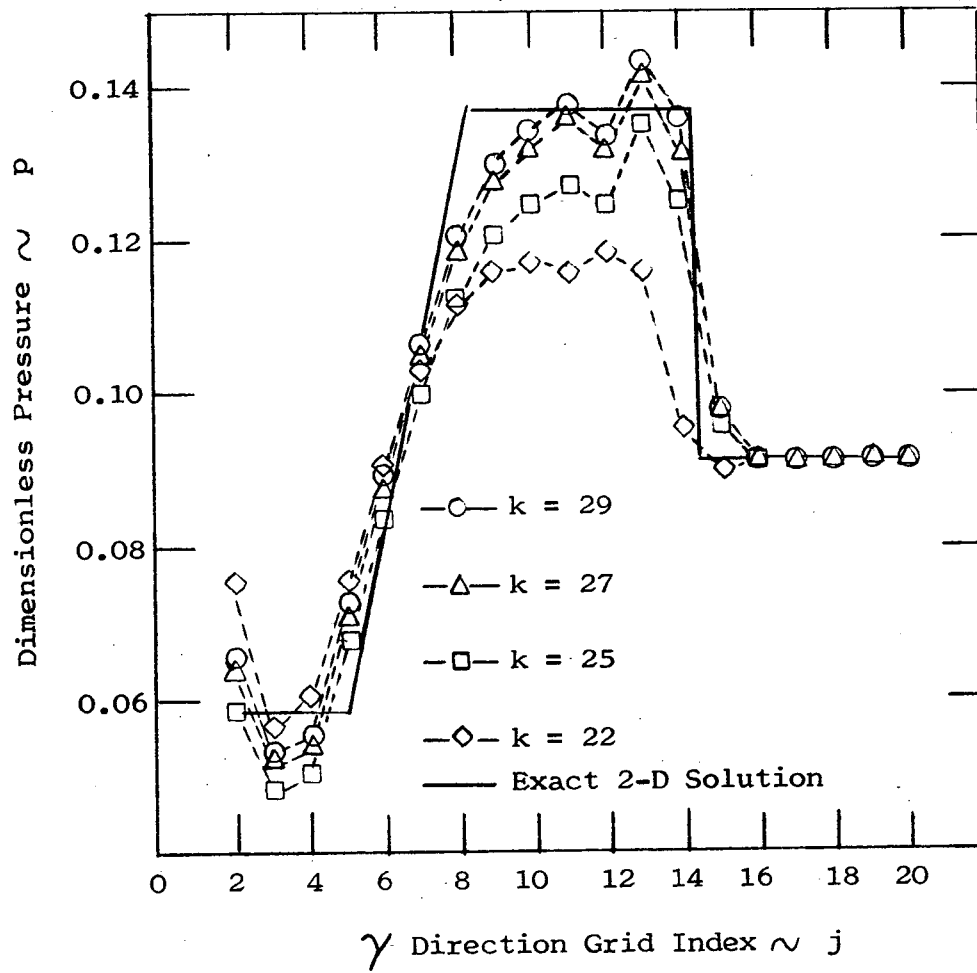


Figure 48. Afterbody lower wedge region normal pressure distributions in the  $\xi = 1.5$  plane for the  $\alpha = 0^\circ$  case

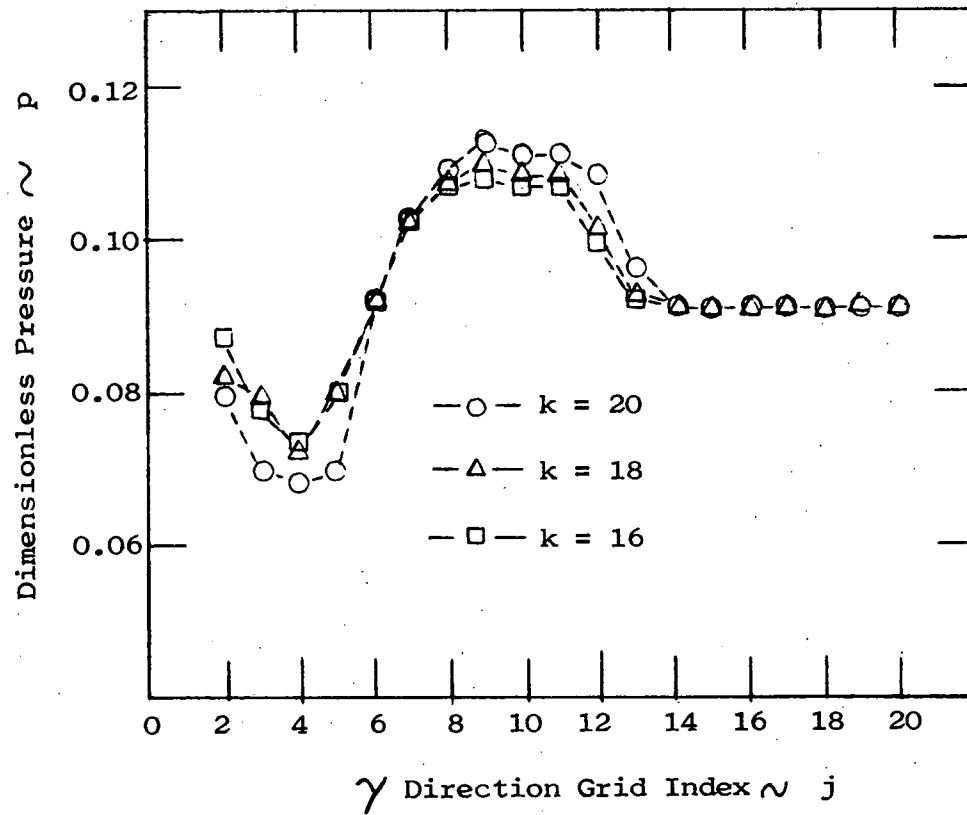


Figure 49. Afterbody lower cone region normal pressure distributions in the  $\xi = 1.5$  plane for the  $\alpha = 0^\circ$  case

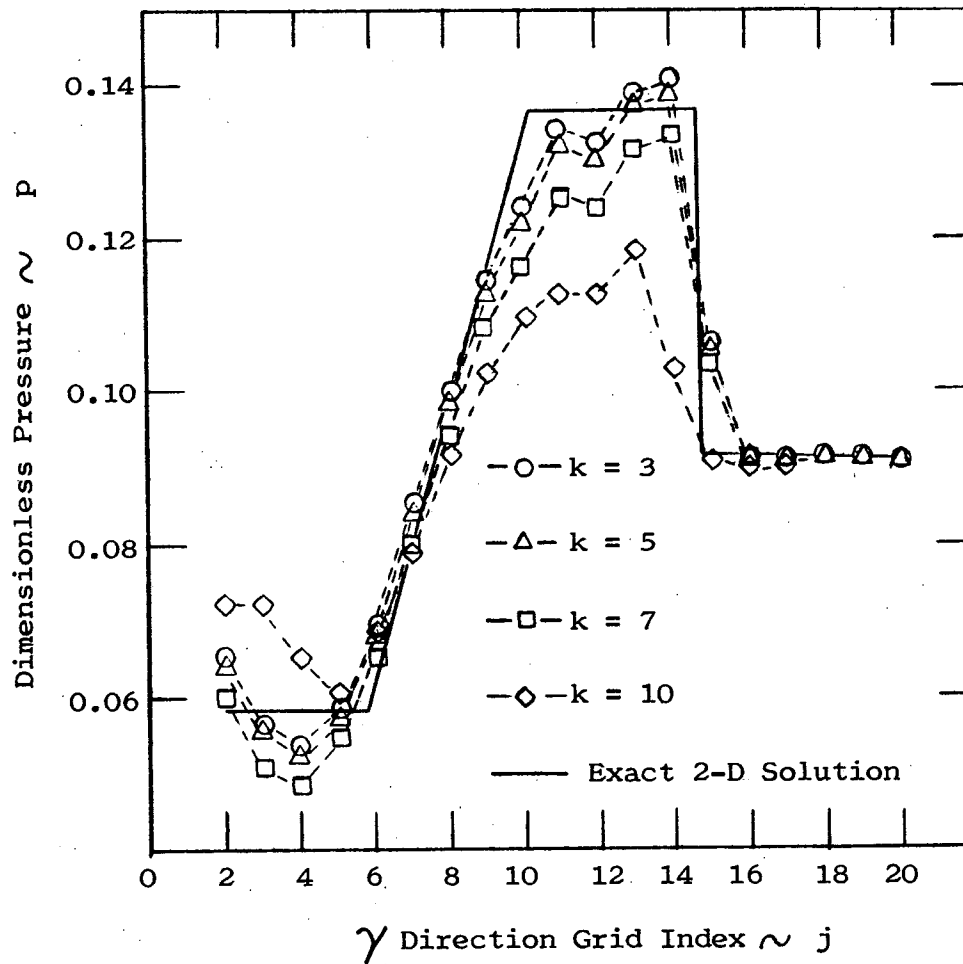


Figure 50. Afterbody upper wedge region normal pressure distributions in the  $\xi = 1.76$  plane for the  $\alpha = 0^\circ$  case

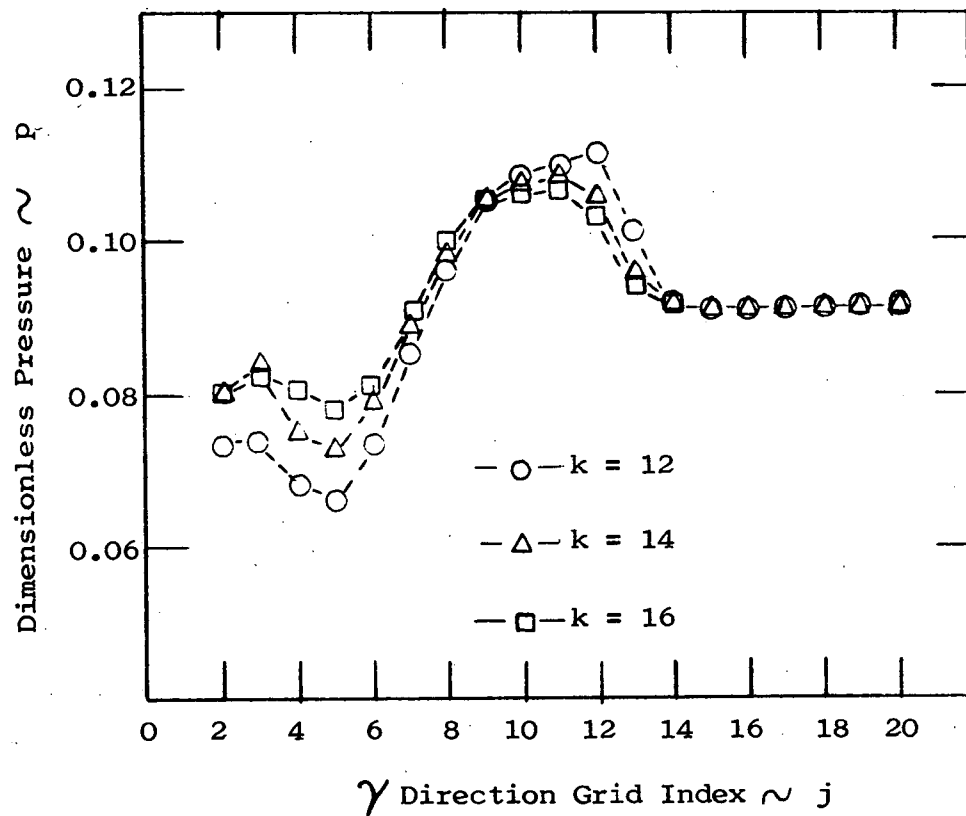


Figure 51. Afterbody upper cone region normal pressure distributions in the  $\xi = 1.76$  plane for the  $\alpha = 0^\circ$  case

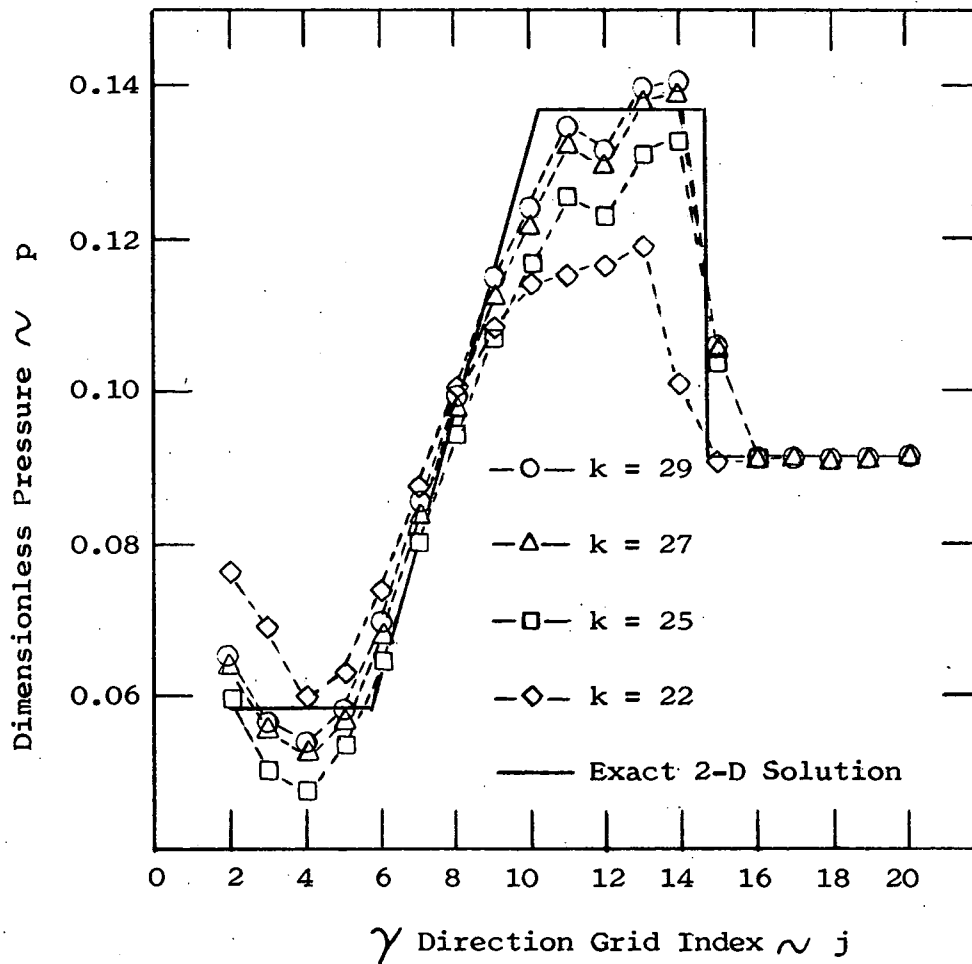


Figure 52. Afterbody lower wedge region normal pressure distributions in the  $\xi = 1.76$  plane for the  $\alpha = 0^\circ$  case

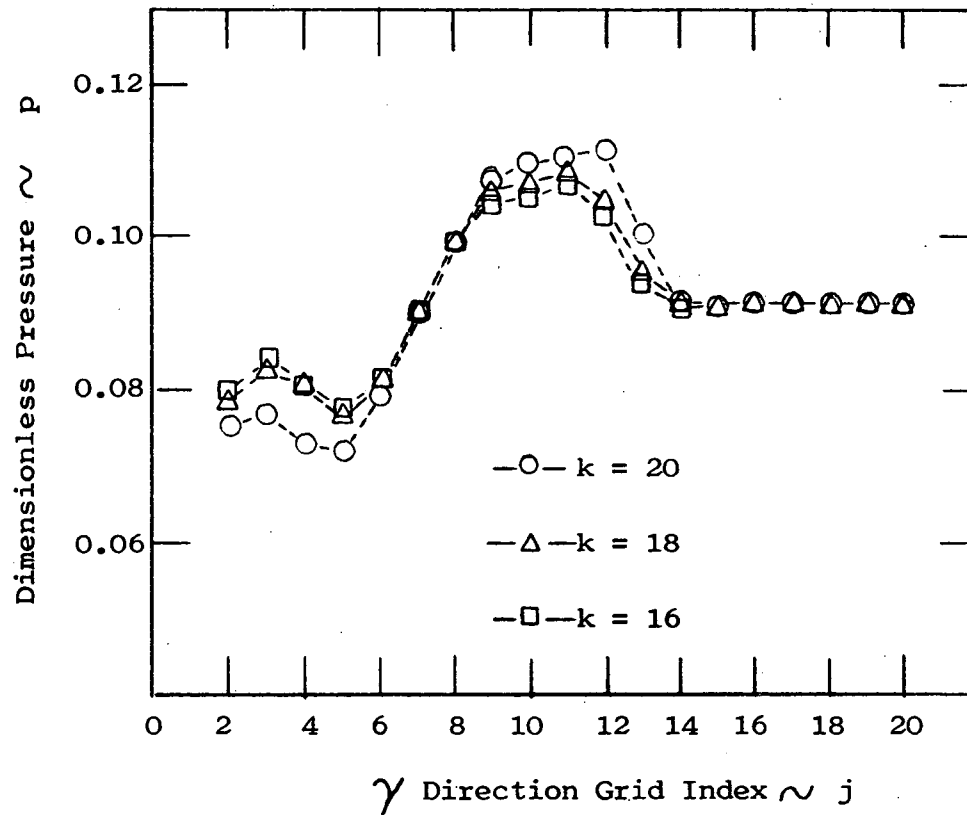


Figure 53. Afterbody lower cone region normal pressure distributions in the  $\xi = 1.76$  plane for the  $\alpha = 0^\circ$  case

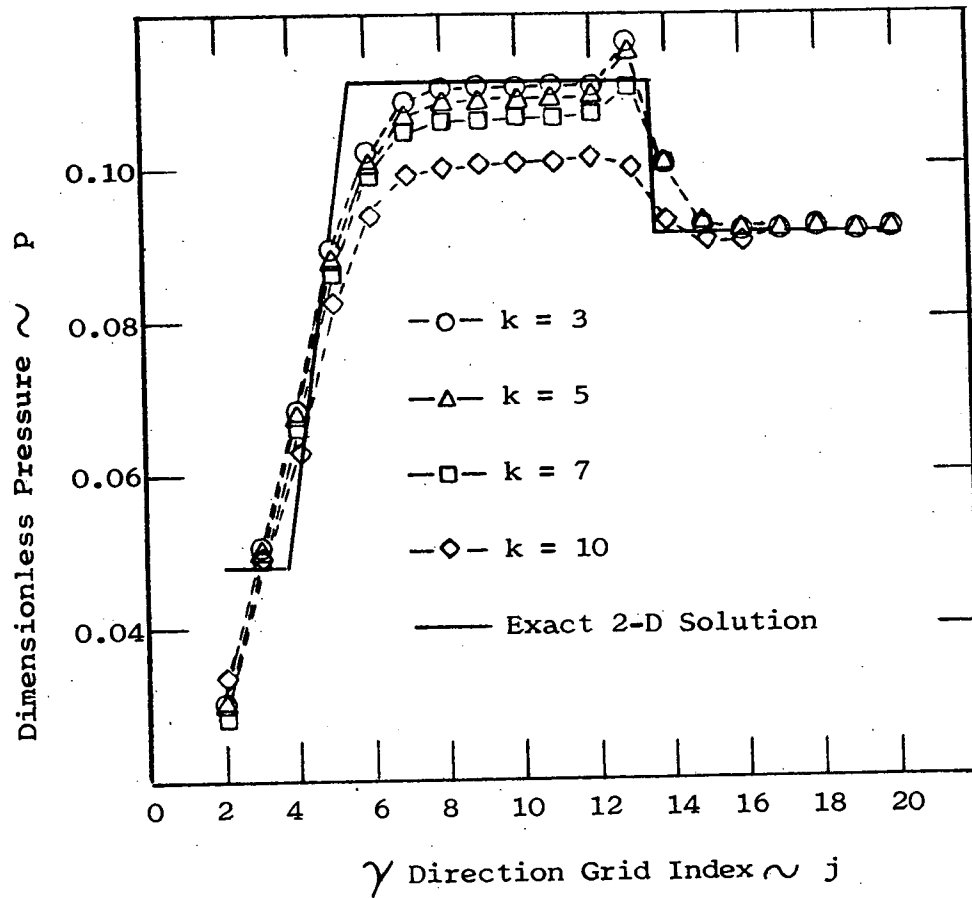


Figure 54. Afterbody upper wedge region normal pressure distributions in the  $\xi = 1.25$  plane for the  $\alpha = 4^\circ$  case

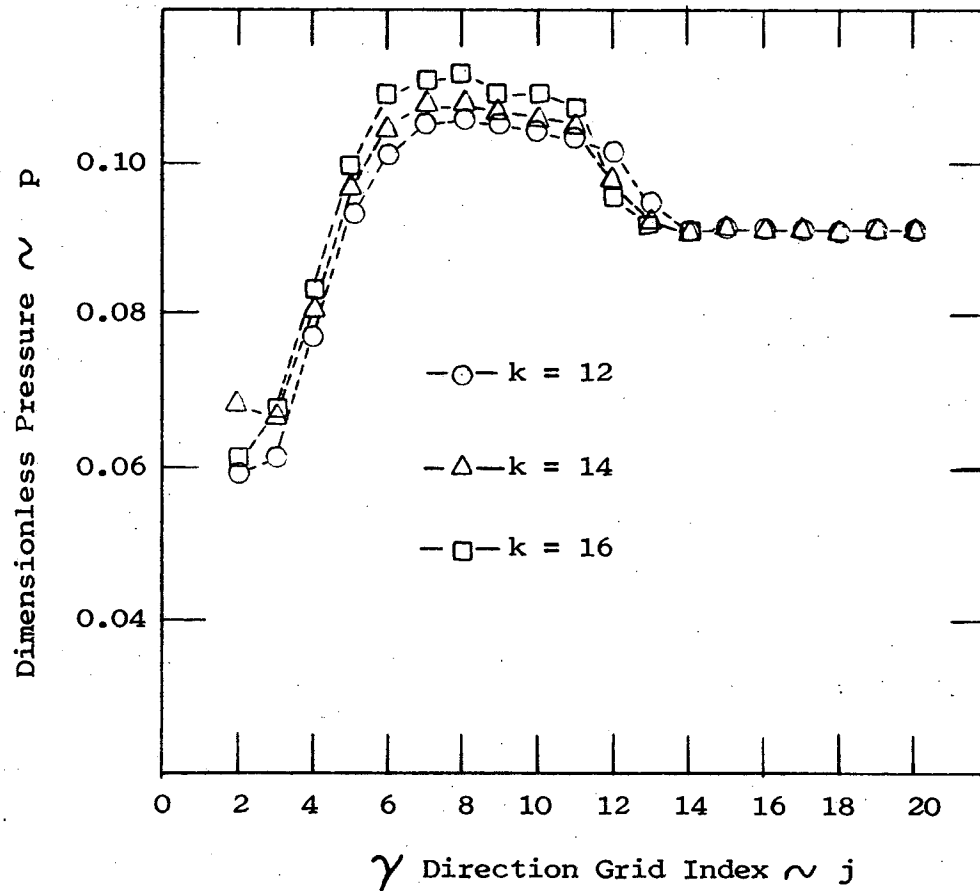


Figure 55. Afterbody upper cone region normal pressure distributions in the  $\xi = 1.25$  plane for the  $\alpha = 4^\circ$  case

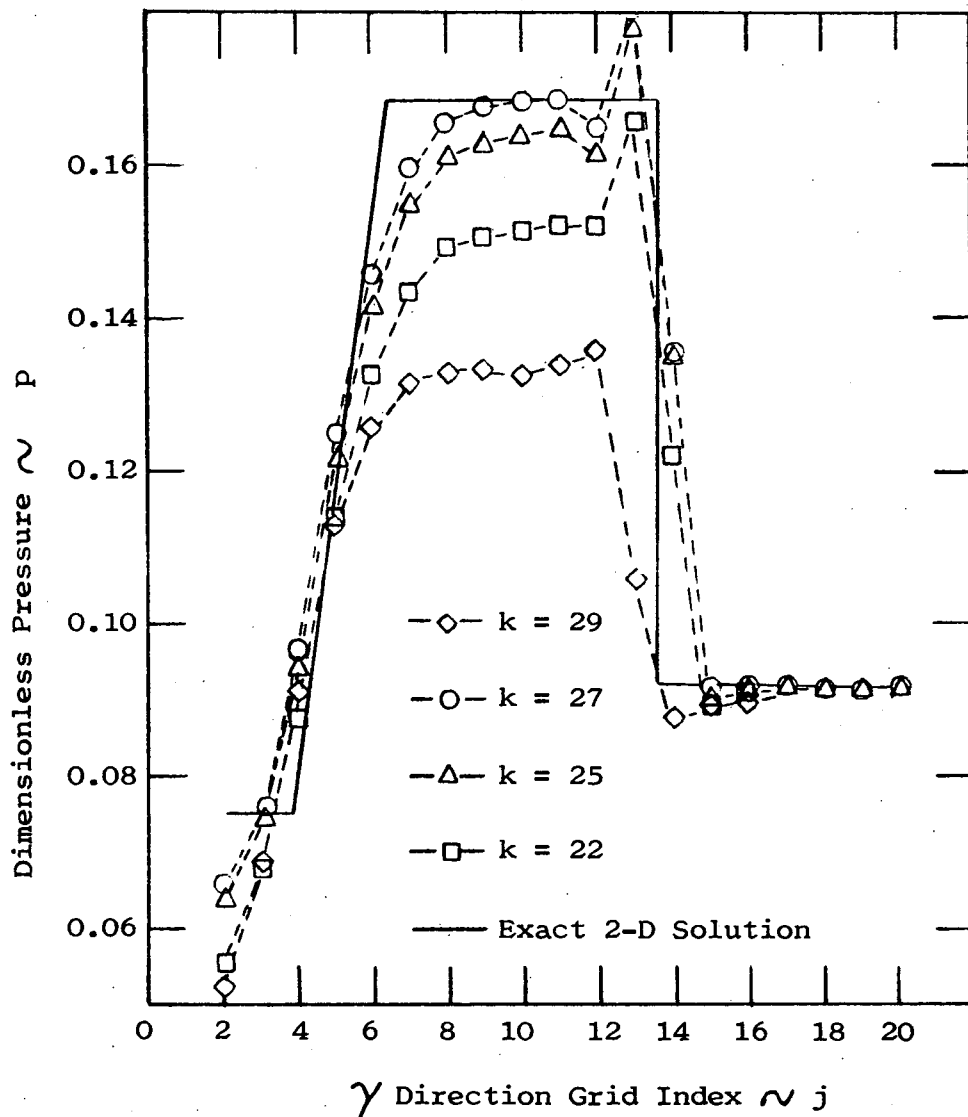


Figure 56. Afterbody lower wedge region normal pressure distributions in the  $\xi = 1.25$  plane for the  $\alpha = 4^\circ$  case

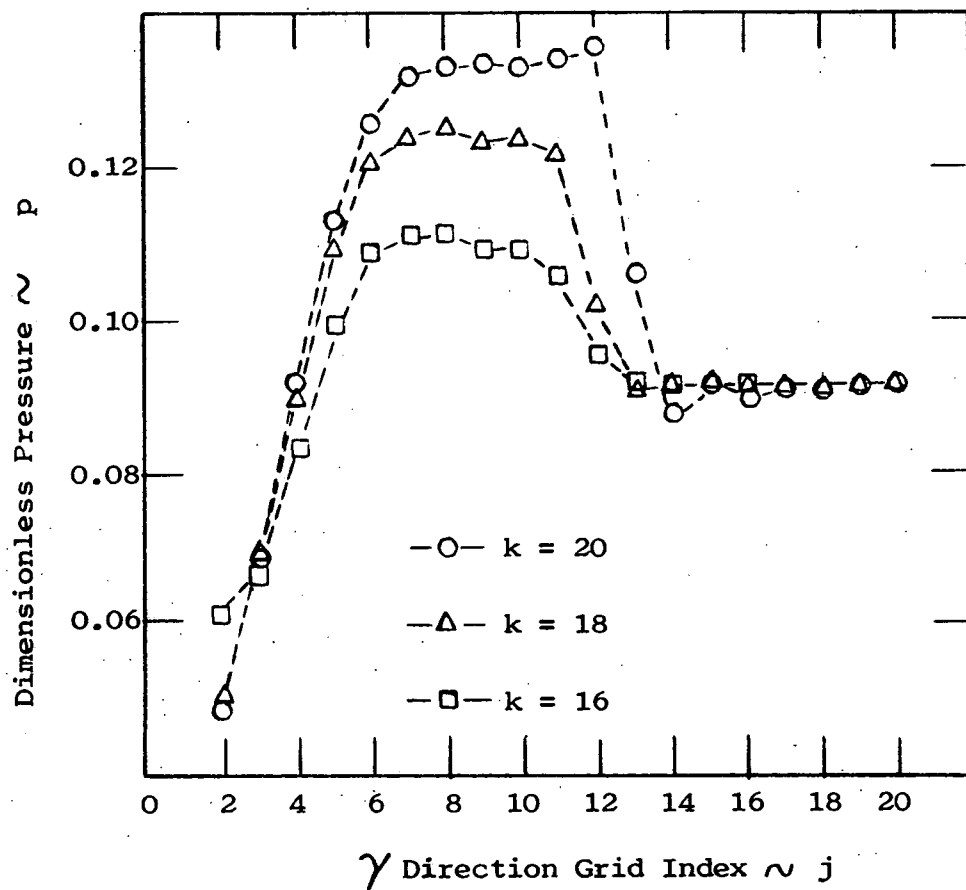


Figure 57. Afterbody lower cone region pressure distributions in the  $\xi = 1.25$  plane for the  $\alpha = 4^\circ$  case

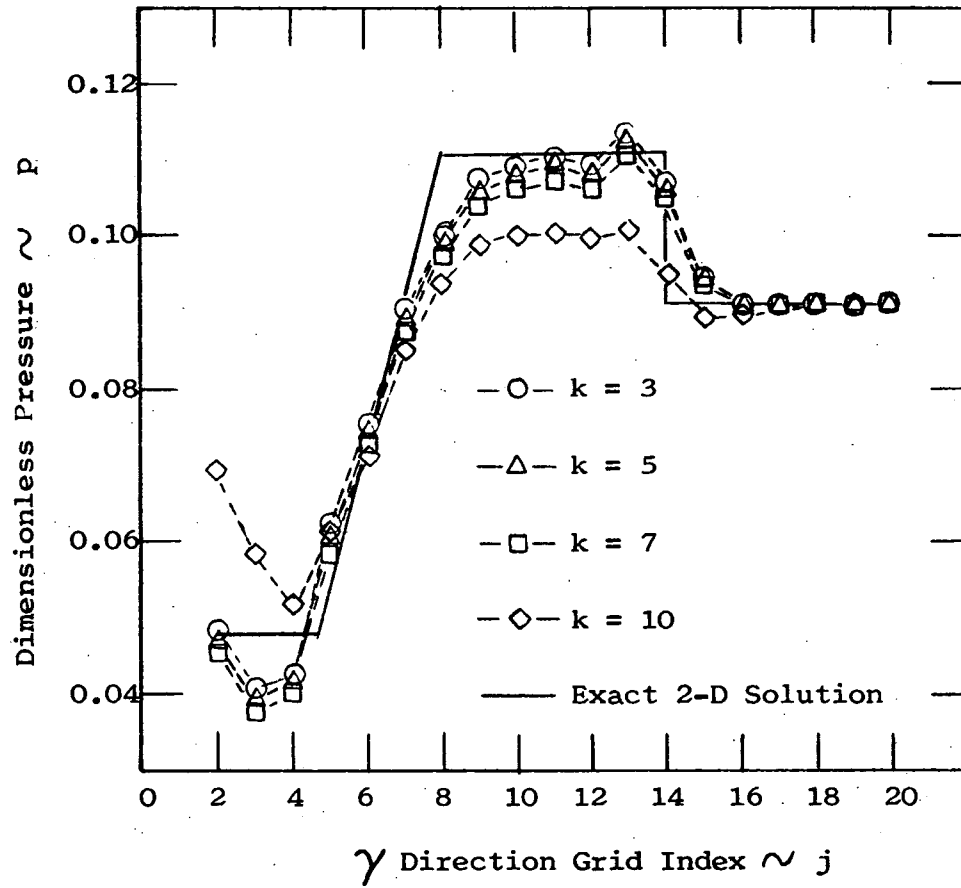


Figure 58. Afterbody upper wedge region normal pressure distributions in the  $\xi = 1.5$  plane for the  $\alpha = 4^\circ$  case

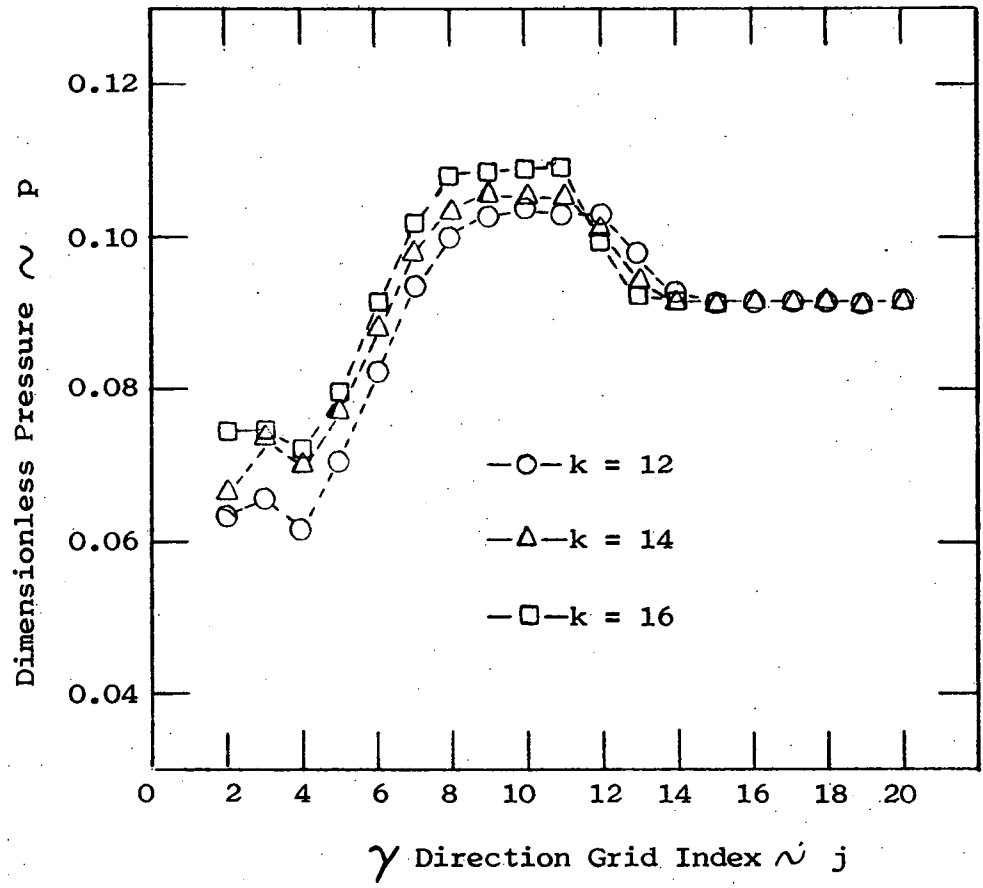


Figure 59. Afterbody upper cone region normal pressure distributions in the  $\xi = 1.5$  plane for the  $\alpha = 4^\circ$  case

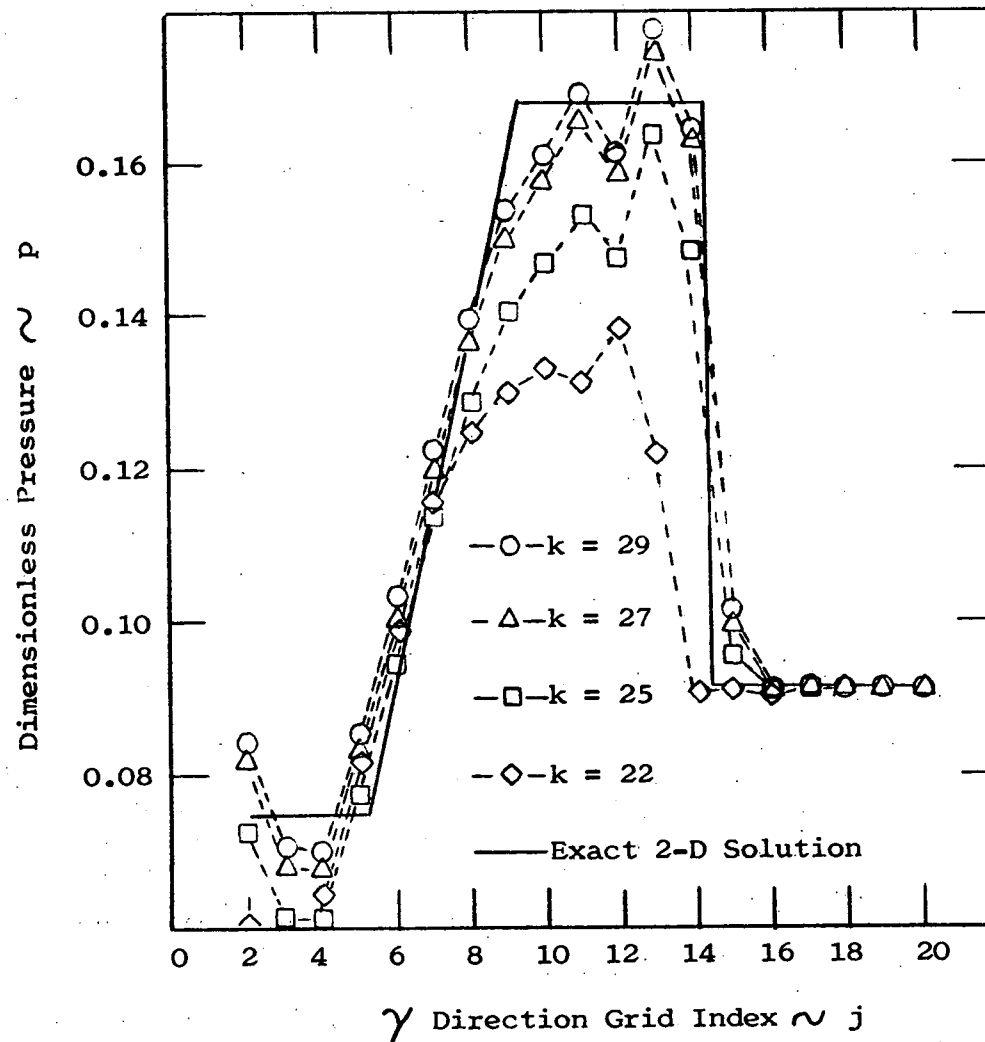


Figure 60. Afterbody lower wedge region normal pressure distributions in the  $\xi = 1.5$  plane for the  $\alpha = 4^\circ$  case

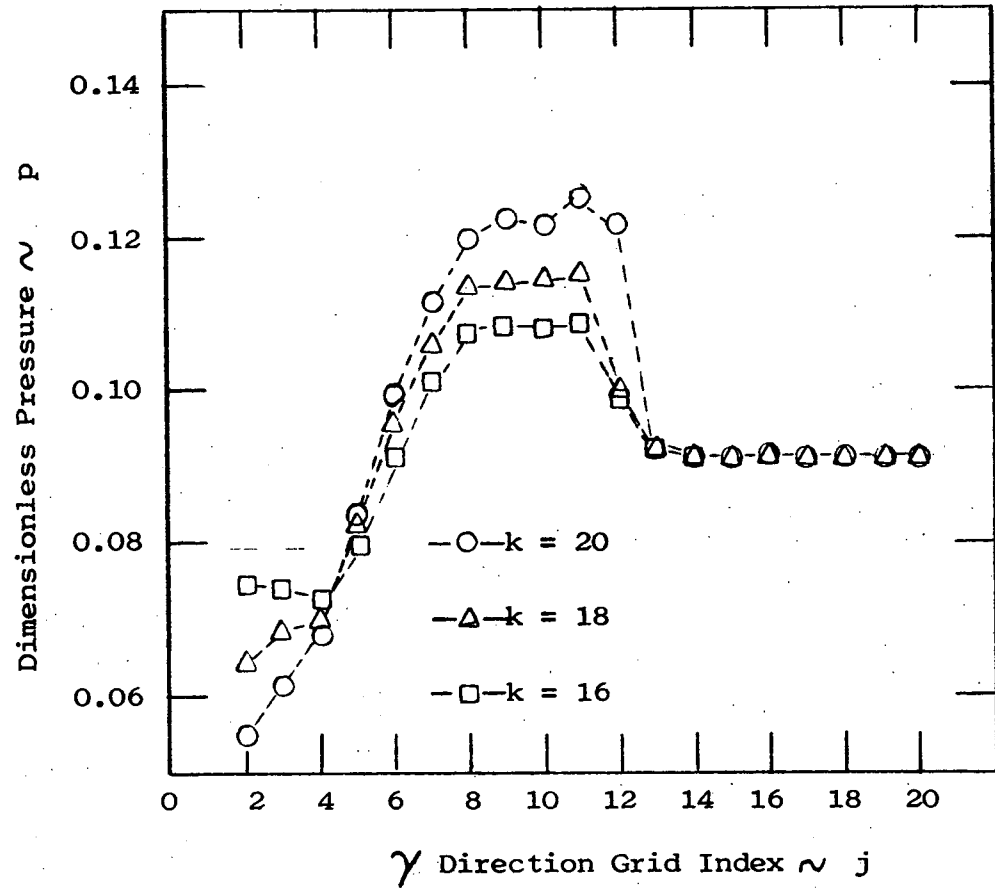


Figure 61. Afterbody lower cone region normal pressure distributions in the  $\xi = 1.5$  plane for the  $\alpha = 4^\circ$  case

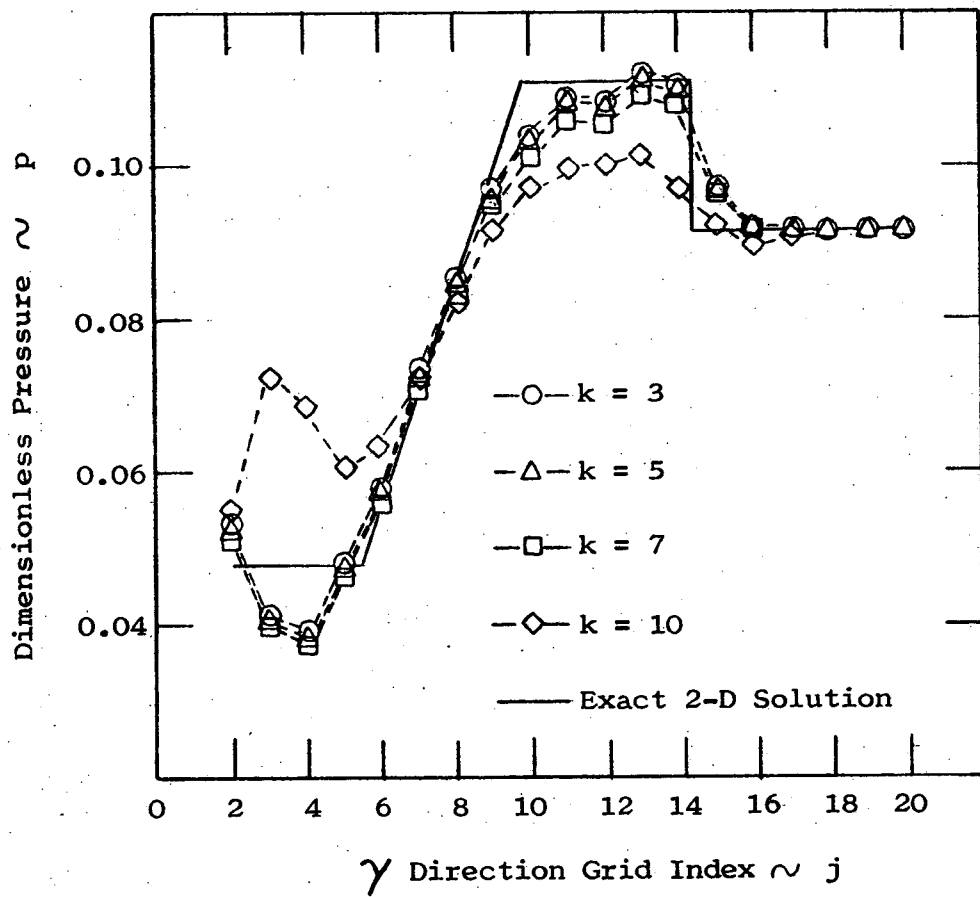


Figure 62. Afterbody upper wedge region normal pressure distributions in the  $\xi = 1.76$  plane for the  $\alpha = 4^\circ$  case

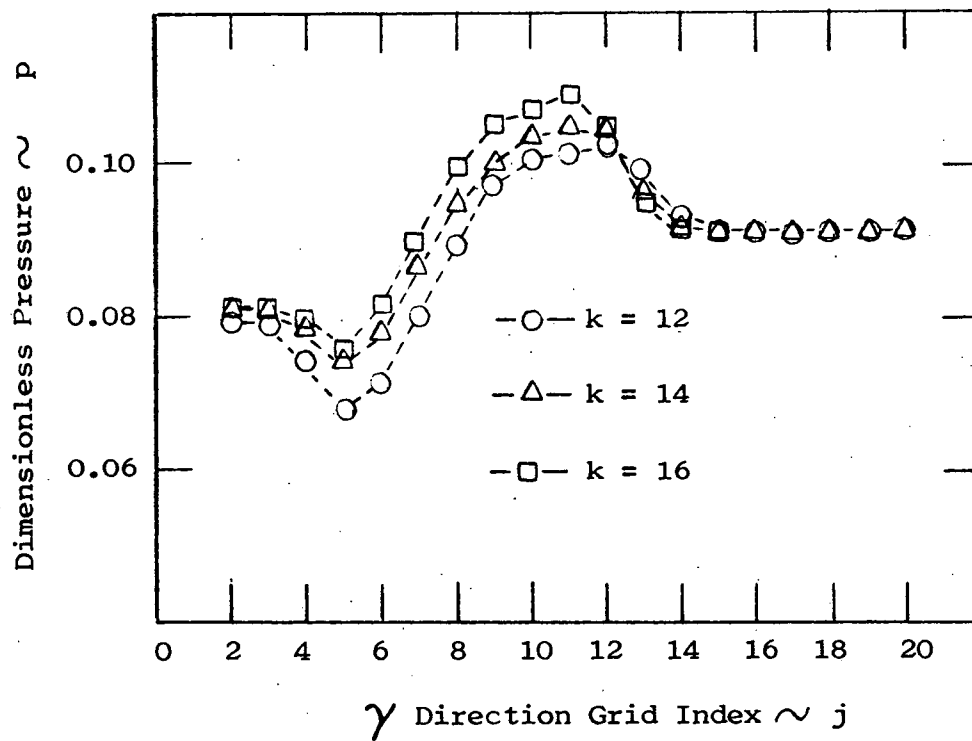


Figure 63. Afterbody upper cone region normal pressure distributions in the  $\xi = 1.76$  plane for the  $\alpha = 4^\circ$  case

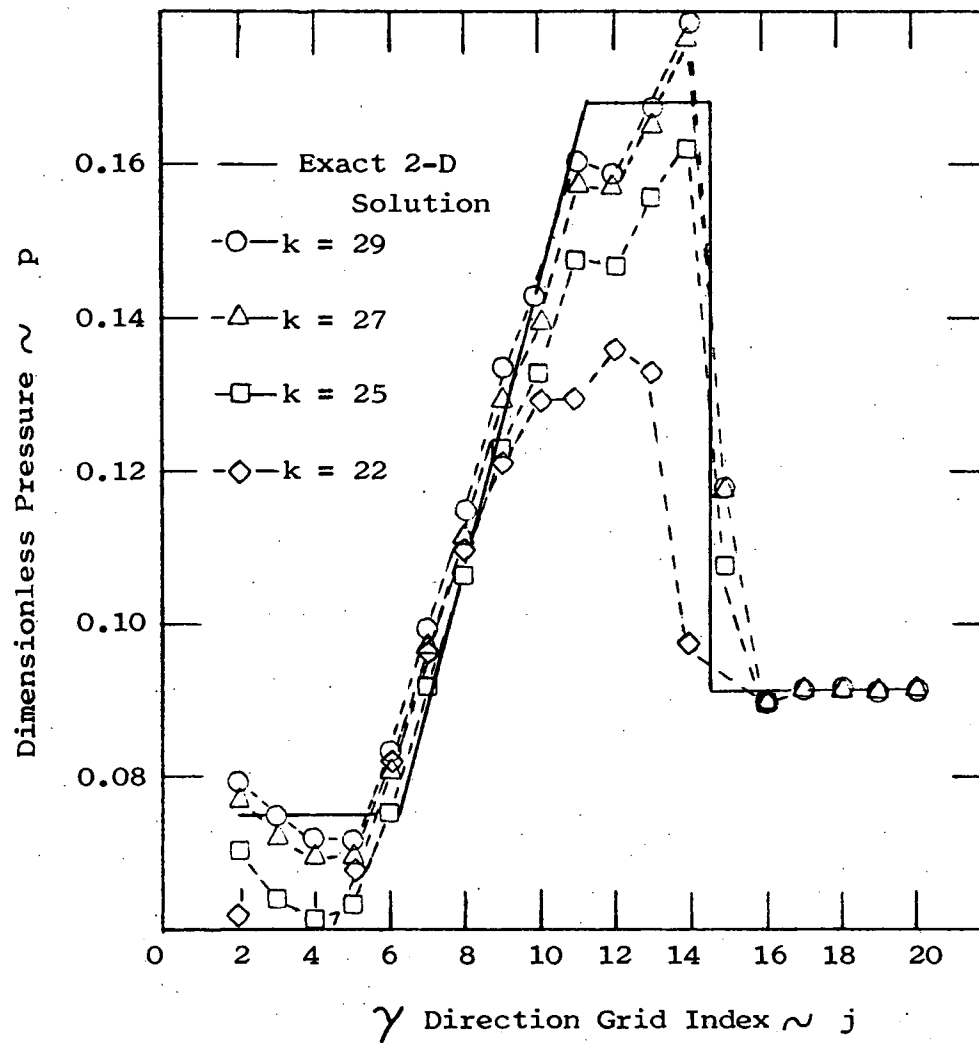


Figure 64. Afterbody lower wedge region normal pressure distributions in the  $\xi = 1.76$  plane for the  $\alpha = 4^\circ$  case

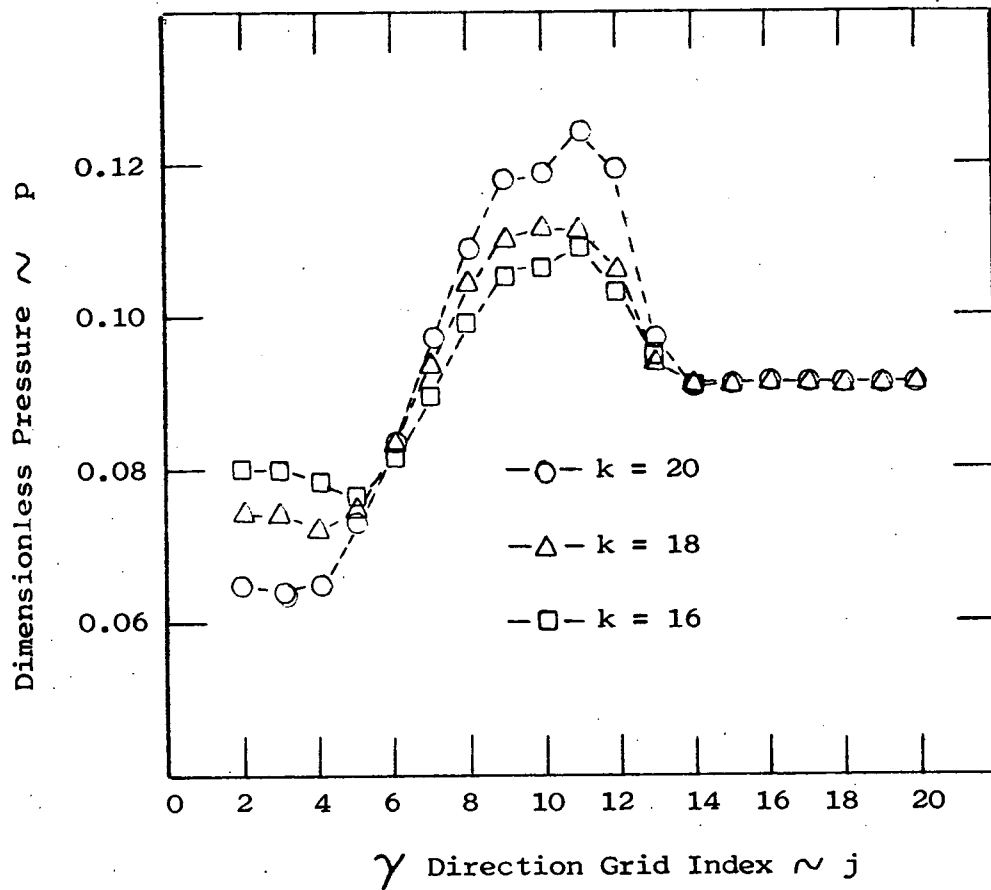


Figure 65. Afterbody lower cone region normal pressure distributions in the  $\xi = 1.76$  plane for the  $\alpha = 4^\circ$  case

The distributions, which now contain an expansion region as well as a bow shock, appear to be fairly smooth except in the vicinity of the shock where mild oscillations develop early in the integration process and become quite severe in the trailing edge region where the very low mesh ratios are used to satisfy the cross flow stability criteria. The shock waves in all distributions, however, are quite well defined and usually contained in one to two intervals. The expansions are quite smooth and in the 2-D wedge regions follow the exact solutions quite closely. The numerical technique does, however, appear to overexpand the flow in both the wedge regions and cone regions on the body surface. The 2-D wedge body pressure for the  $\alpha = 0^\circ$  case is 0.0588, and for the  $\alpha = 4^\circ$  case the upper and lower 2-D wedge body pressures are 0.048 and 0.075 respectively. The numerical solution values are initially somewhat lower. However, as the integration proceeds to the trailing edge the 2-D body pressures increase again to nearly their proper values. The overexpansion also propagates into the flow field normal to the wing chord plane.

With the exception of the overexpansion situation near the body surface, the numerical technique generates a 2-D solution that compares favorably with the exact solution. In addition, the pressure distributions for the  $\alpha = 0^\circ$  case indicate that the proper flow field symmetry is generated.

### Region III Flow Field Analysis

#### Afterbody geometry, coordinate system and equations of motion

That portion of the flow field aft of the trailing edge of the wing is termed the wake. This region, void of any solid boundaries, is bounded on three sides by the free stream and on the fourth side by the 2-D flow field associated with the wake of a symmetric double wedge.

The coordinate system used to define the wake flow field is a Cartesian system with the origin centered at the forebody cone apex. The same frame was used to describe the body geometry associated with the forebody and the afterbody. The grid in each  $x = \text{constant}$  plane is defined by the intersection of a set of  $y = \text{constant}$  and  $z = \text{constant}$  planes, resulting in a rectangular arrangement of mesh points.

The equations of motion in the Cartesian frame are given by Equations (38) with the conservative variables  $\bar{E}$ ,  $\bar{F}$  and  $\bar{G}$  given in Equations (39) - (41).

#### Initial and boundary conditions

The boundary conditions applied at the outer extremes of the grid are similar to those used in the afterbody integration. The grid dimensions are chosen large enough such that the outer grid points always lie in the free stream along the upper and lower grid boundaries as well as on the boundary off the wing tip. Along the 2-D flow region boundary the reflection technique is used to

determine the flow variables. Hence, as long as the flow along this boundary remains two-dimensional the numerical solution may be compared with the known 2-D exact solution in an attempt to evaluate the performance of the numerical technique. It is noted here that if the tip Mach cone intersects this boundary the flow will no longer be two-dimensional and the 2-D exact solution no longer applies. However, the 3-D solution generated by the numerical technique in this case is still legitimate with the  $z = \text{constant}$  plane about which the reflection occurs representing the center of the 3-D wing.

The initial data used in the wake integration are generated in the afterbody integration and are contained in the final integration plane of the afterbody. Since the grid points associated with the afterbody and wake systems do not, in general, coincide the data must be transferred from the afterbody grid to the wake grid. The linear interpolation scheme used in the forebody-afterbody data shift is used here.

#### Grid system and solution technique

The wake grid in each  $x = \text{constant}$  plane contains 40 mesh points in both the  $y$  and  $z$  directions. The grid is positioned in the wake region with the  $j = 20$  and  $21$  mesh points at  $y = \Delta y/2$  and  $-\Delta y/2$  respectively (see Figure 66). Hence, half the grid points lie above the wing chord plane and half below.

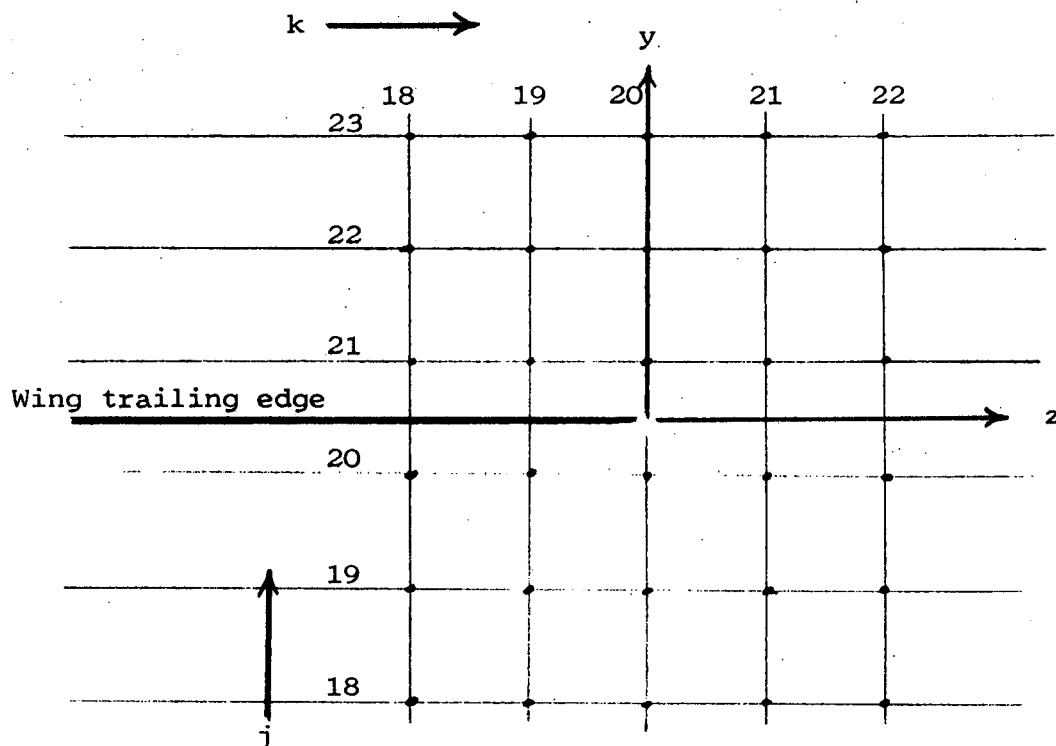


Figure 66. A portion of the wake grid system showing the relative location of the wing

The numerical values for  $\Delta y$  and  $\Delta z$  used in the wake integration are 0.195 and 0.176 respectively for the  $\alpha = 0^\circ$  case and 0.195 and 0.1584 respectively for the  $\alpha = 4^\circ$  case. The incremental magnitudes were chosen such that in the wake initial data plane the 3-D portion of the wing flow field is contained within a region bounded on the lower and upper sides by grid points with indicies  $j = 10$  and  $30$  respectively and on the left and right by grid points with indicies  $k = 10$  and  $30$  respectively. Hence, the outermost 10 grid points in the system lie either in the free stream or in the

2-D double-wedge flow field. However, as the integration proceeds into the wake the 3-D flow field propagates throughout the grid to the grid boundaries.

The afterbody integration was terminated at  $x = 1.97$ . Hence, the flow variables at the grid points in the  $x = 1.97$  plane provide the initial data for the wake integration. The data are transferred from the afterbody grid to the wake grid, and a single integration step of magnitude  $\Delta x = 0.06$  generates the data in the first  $x =$  constant plane in the wake behind the wing. It is noted that the wing trailing edge is located at the half-interval of the first integration step.

Subsequent integration step sizes were chosen to be the maximum allowed as predicted by the linear stability theory. The eigenvalues associated with the equations of motion for the wake are developed in Appendix A. Equations (A6) and (A9) represent the maximum eigenvalues of the A and B matrices respectively and, as a result, are used in conjunction with Equations (43) to determine the maximum step size  $\Delta x$ . For both cases considered the integration was terminated well before the shock wave intersects the grid boundaries which occurs at about one chord length behind the wing.

### Numerical solutions

Figures 67 and 68 show various pressure distributions normal to the wing chord plane for the  $\alpha = 0^\circ$  case in the  $x = 2.57$  and  $x = 3.0$  planes respectively. Figures 69 and 70 show similar

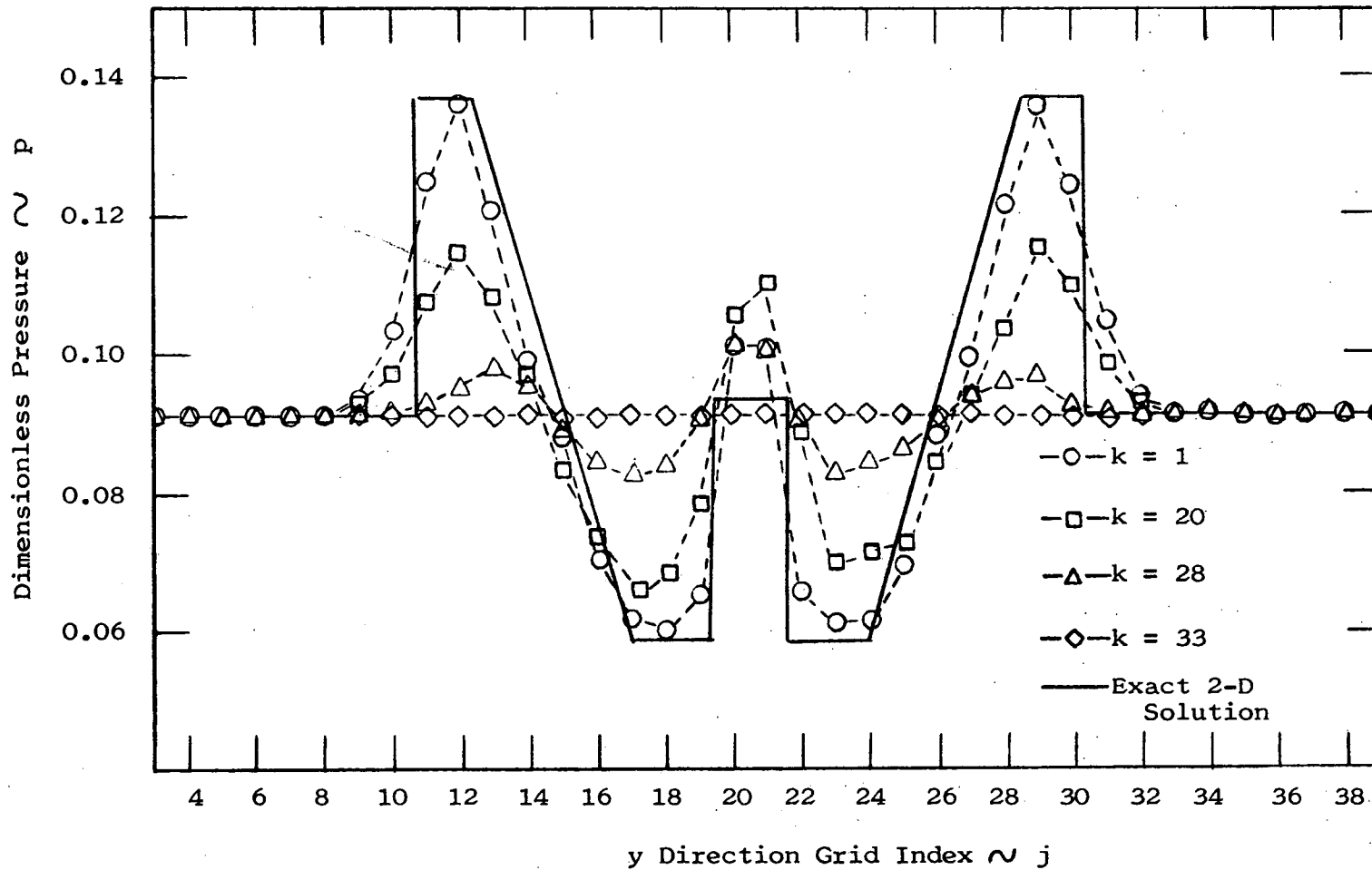


Figure 67. Pressure distributions normal to the wing chord plane for the  $\alpha = 0^\circ$  case in the  $x = 2.57$  plane

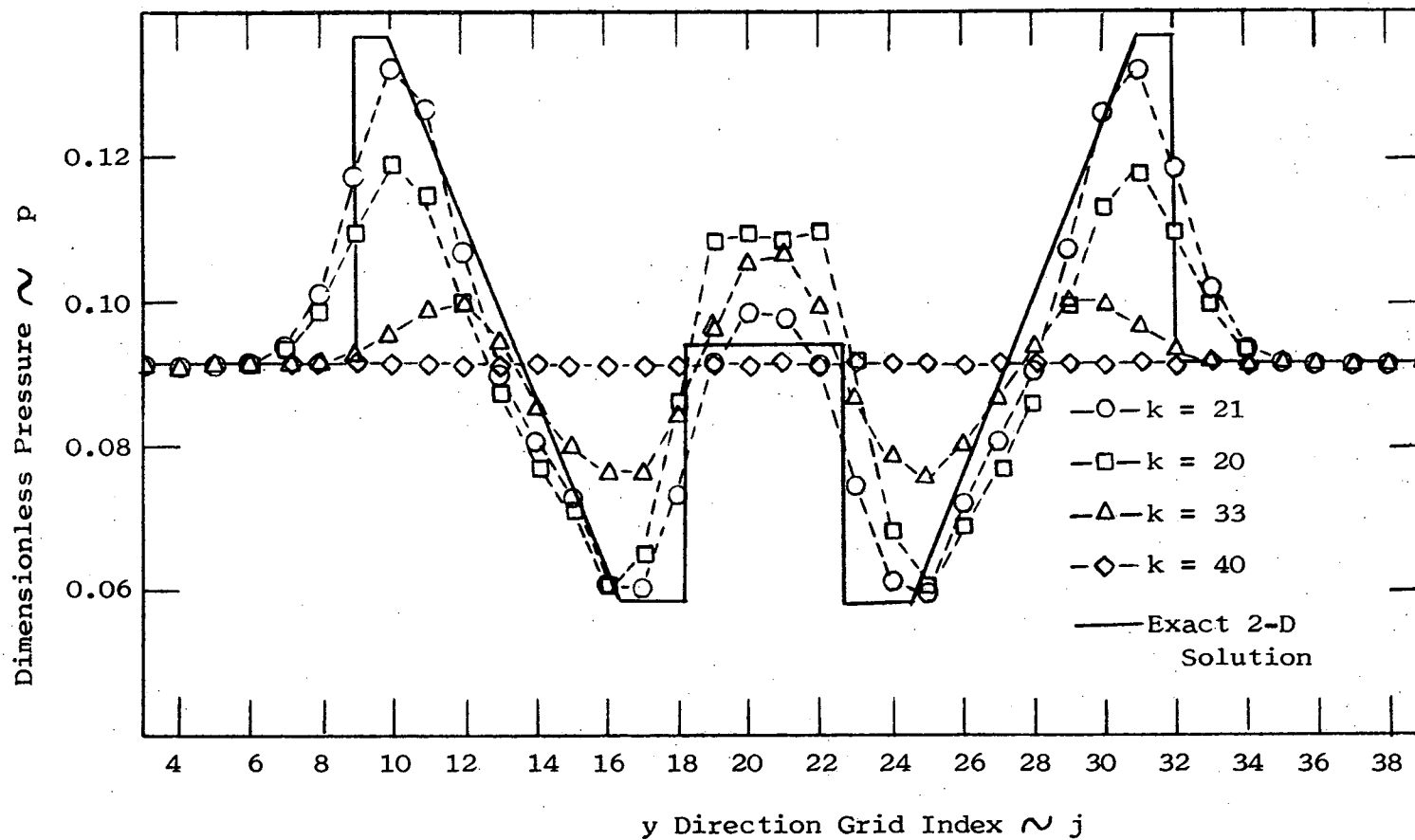


Figure 68. Pressure distributions normal to the wing chord plane for the  $\alpha = 0^\circ$  case in the  $x = 3.0$  plane

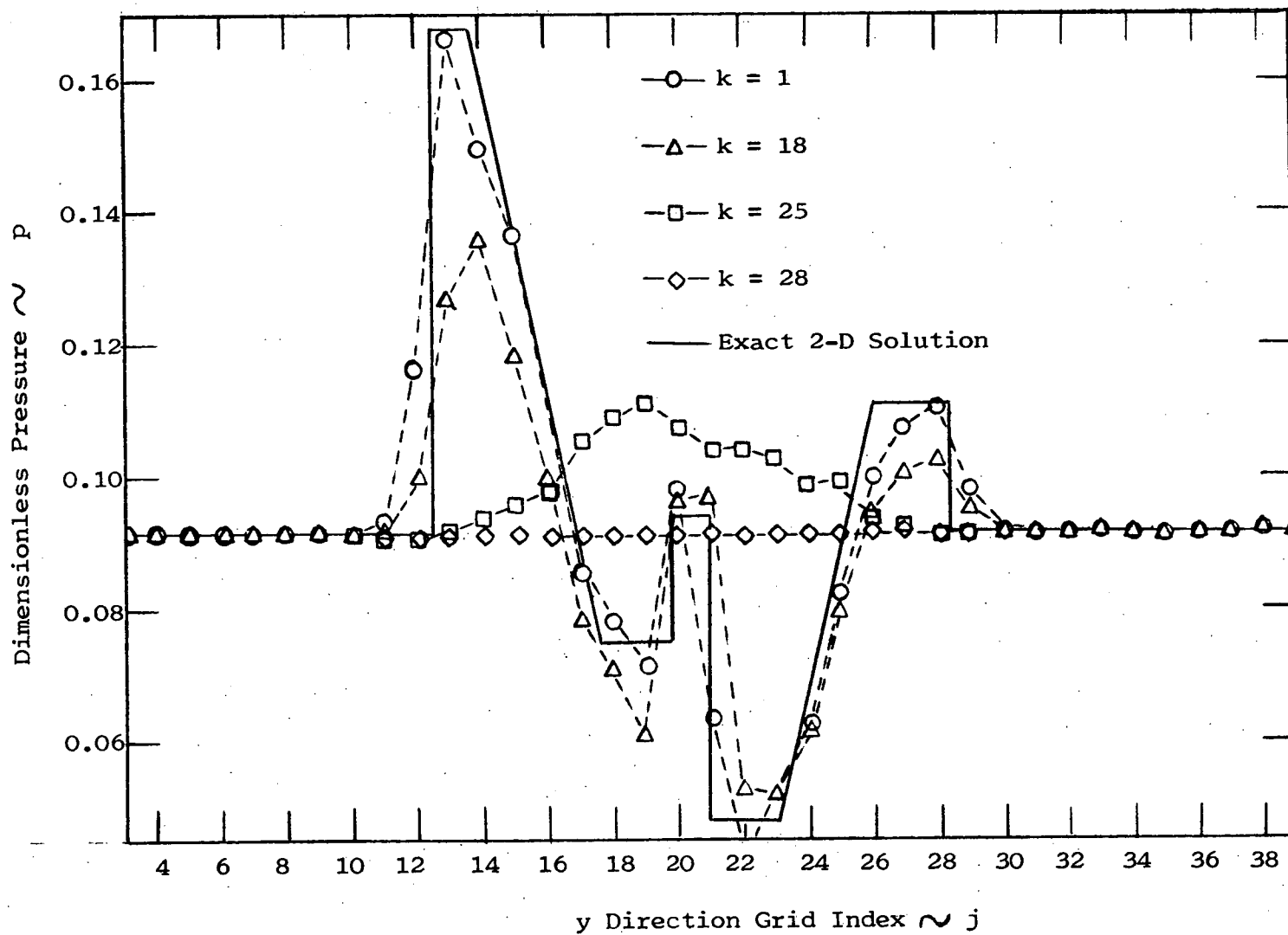


Figure 69. Pressure distributions normal to the wing chord plane for the  $\alpha = 4^\circ$  case in the  $x = 2.12$  plane

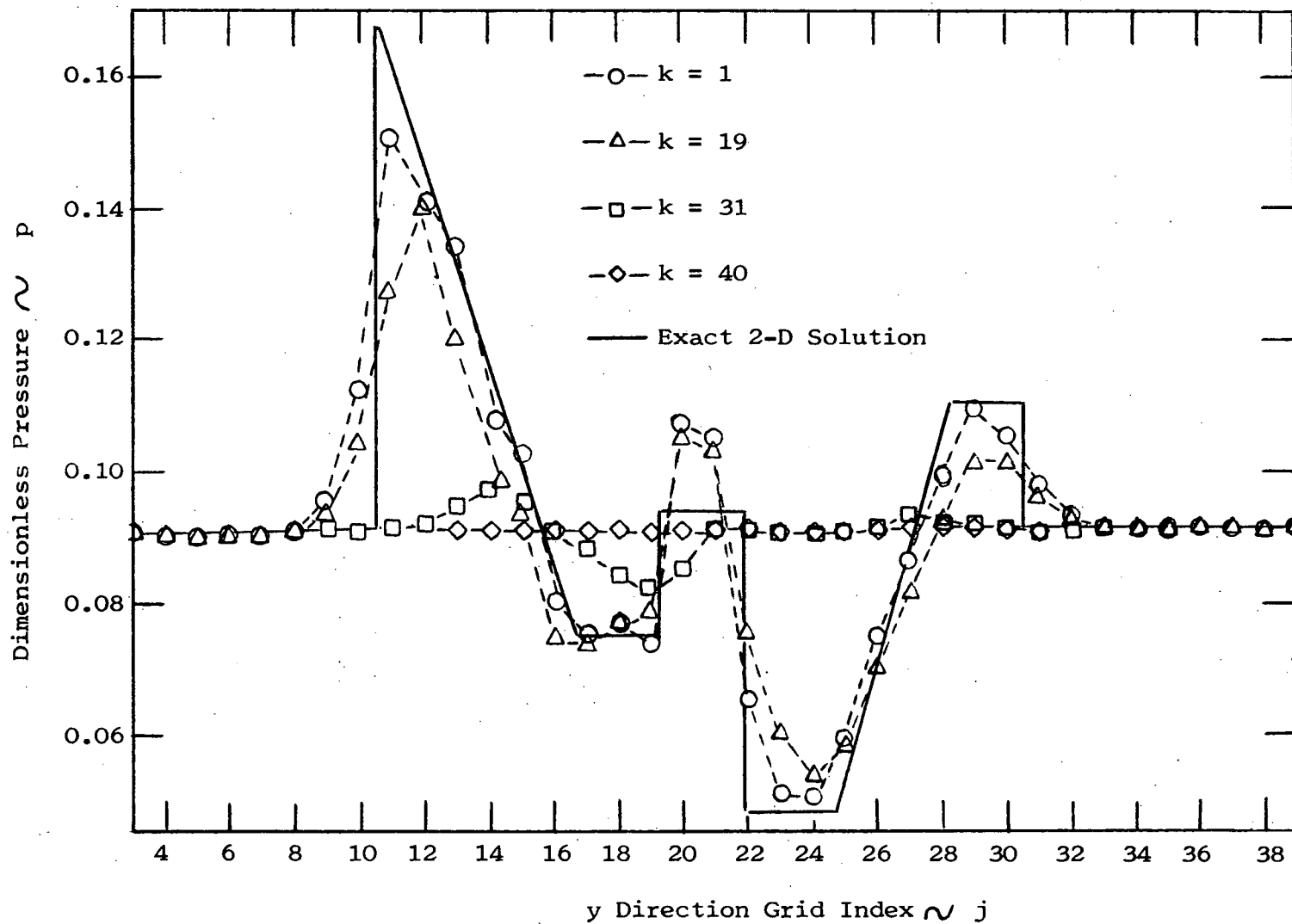


Figure 70. Pressure distributions normal to the wing chord plane for the  $\alpha = 4^\circ$  case in the  $x = 2.6$  plane

distributions for the  $\alpha = 4^\circ$  case in the  $x = 2.12$  and  $x = 2.6$  planes respectively. Each contains an exact 2-D solution for comparison. It is noted again here that the index values  $k = 1, 20$  and  $40$  define grid points in the 2-D double-wedge wake flow region, the wing tip and free stream region off the wing tip respectively.

In moving along the pressure distributions point to point from  $j = 1$  to  $j = 40$  one encounters a bow shock, an expansion and a recompression shock all associated with the lower surface flow, then another recompression shock, an expansion and a bow shock associated with the upper surface flow.

The distributions appear to be smooth with well defined shocks as in the forebody and afterbody solutions. The numerical 2-D solution ( $k = 1$ ) appears to agree quite well with the exact 2-D solution. The bow shocks have proper strengths as well as locations. However, the strengths of the recompression shocks as predicted by the numerical method appear to be excessive. For the  $\alpha = 0^\circ$  case the pressure behind the recompression shock should be 0.0935 with the worst numerical solution yielding 0.101, resulting in an 8.02 per cent error. For the  $\alpha = 4^\circ$  case the exact and worst numerical values are 0.94 and 0.1075 respectively, yielding a 14.4 per cent error. The recompression shock locations in the 2-D region seem to be well predicted by the numerical method in all cases.

## RECOMMENDATIONS FOR FURTHER STUDY

One of the major difficulties associated with the wake region analysis is that the Cartesian coordinate system used to generate the wake grid system severely limits the distance into the wake that the integration can proceed. Once the shock intersects the grid boundary the integration must be terminated for lack of proper boundary conditions. To proceed farther into the wake the grid system must be enlarged. This increases the computer storage requirements and quickly becomes prohibitive in terms of computer capacity.

This problem can be eliminated by changing the wake coordinate system to a conical system with an origin at the apex of the forebody cone. Then a grid system can then be developed such that the 3-D flow field is contained within the grid boundaries regardless of distance behind the wing.

The analysis could also be extended to include a variety of wing cross-sections such as parabolic or circular arc sections, cambered as well as uncambered. In addition, a wider variety of tip geometries could be investigated.

Although exact solutions are available for comparison with the numerical solution in the 2-D regions of the flow field no such standards exist for the 3-D flow regions. Hence, the performance of the numerical technique can only be extrapolated from the 2-D results. It would be quite desirable to have experimental evidence to verify the numerical results in the 3-D regions.

Although in so far as the author knows no experimental investigations have been made on the particular wing configuration used in this analysis, experimental studies have been made on rectangular wings of other cross sections. In particular, Davis<sup>(28)</sup> conducted experimental tests on various nonlifting rectangular planform wings with parabolic cross-sections. The numerical technique used in this investigation could be easily adapted to the Davis wing configurations. Hence, the 3-D region performance of the numerical technique could be checked.

The recommendations suggested above are based on the experience gained in applying the MacCormack technique to the wing configuration used in this study. The method yielded satisfactory results in most cases and, as a result, appears to represent a powerful tool which could be used to investigate flow fields about various other configurations.

## REFERENCES

1. Lax, P. D., "Weak Solutions of Nonlinear Hyperbolic Equations and Their Numerical Computation," Communications on Pure and Applied Mathematics, Vol. 7, 1954, pp. 159-193.
2. Bohachevsky, I. O. and Mates, R. E., "A Direct Method for Calculation of the Flow About an Axisymmetric Blunt Body at Angle of Attack," American Institute of Aeronautics and Astronautics Journal, Vol. 4, 1966, pp. 776-782.
3. Bohachevsky, I. O. and Rubin, E. L., "A Direct Method for Computation of Nonequilibrium Flows with Detached Shock Waves," American Institute of Aeronautics and Astronautics Journal, Vol. 4, 1966, pp. 600-607.
4. DeJarnette, F. R., Application of Lax's Finite Difference Method to Nonequilibrium Hypersonic Flow Problems, National Aeronautics and Space Administration, Tech. Rep. NASA R-234, 1966.
5. Kutler, P., Application of Selected Finite Difference Techniques to the Solution of Conical Flow Problems, Ph.D. Thesis, Iowa State University, 1969.
6. MacCormack, R. W., The Effect of Viscosity in Hypervelocity Impact Cratering, American Institute of Aeronautics and Astronautics Paper No. 69-354, 1969, pp. 1-7.
7. Rusanov, V. V., "On Difference Schemes of Third Order Accuracy for Nonlinear Hyperbolic Systems," Journal of Computational Physics, Vol. 5, 1970, pp. 507-516.
8. Burstein, S. Z. and Murin, A. A., "Third Order Difference Methods for Hyperbolic Equations," Journal of Computational Physics, Vol. 5, 1970, pp. 547-571.
9. Lax, P. D. and Wendroff, B., "Difference Schemes for Hyperbolic Equations with High Order of Accuracy," Communications on Pure and Applied Mathematics, Vol. 17, 1964, pp. 381-398.
10. Leith, C. E., "Numerical Simulation of the Earth's Atmosphere," Methods in Computational Physics, Vol. 4, edited by Alder, B., Fernbach, S. and Rotenberg, M., Academic Press, New York, 1965, pp. 1-28.

11. Fromm, J. E., "A Method for Reducing Dispersion in Convective Difference Schemes," Journal of Computational Physics, Vol. 3, 1968, pp. 176-189.
12. Richtmeyer, R. D., "A Survey of Difference Methods for Non-Steady Fluid Dynamics," National Center for Atmospheric Research Technical Note 63-2, 1962.
13. Burstein, S. Z., "Finite-Difference Calculations for Hydrodynamic Flows Containing Discontinuities," Journal of Computational Physics, Vol. 2, 1967, pp. 198-222.
14. Strang, G., "Accurate Partial Difference Methods. I: Linear Cauchy Problem," Archive for Rational Mechanics and Analysis, Vol. 12, 1963, pp. 392-402.
15. Gourlay, A. R. and Morris, J. L., "Finite-Difference Methods for Nonlinear Hyperbolic Systems," Mathematics of Computation, Vol. 22, 1968, pp. 28-39.
16. Lomax, H., Kutler, P., and Fuller, F. B., The Numerical Solution of Partial Differential Equations Governing Convection, North Atlantic Treaty Organization, AGARDograph No. 146, Oct. 1970.
17. Richtmeyer, R. D. and Morton, K. W., "Difference Methods for Initial-Value Problems," John Wiley and Sons, Inc., New York, 1967.
18. Lomax, H., An Operational Unification of Finite Difference Methods for the Numerical Integration of Ordinary Differential Equations, National Aeronautics and Space Administration, Tech. Rep. NASA R-262, 1967.
19. Kutler, P., and Lomax, H., The Computation of Supersonic Flow Fields about Wing-Body Combinations by "Shock-Capturing" Finite Difference Techniques, Proceedings of the Second International Conference on Numerical Methods in Fluid Dynamics, University of California, Berkeley, 1970.
20. Hopf, E., "The Partial Differential Equation  $u_t + uu_x = u_{xx}$ ," Communications on Pure and Applied Mathematics, Vol. 3, 1950, pp. 201-230.
21. Anderson, D. A., and Vogel, J. M., Numerical Calculations of Flow Fields, Engineering Research Institute, Ames, Iowa, Tech. Rep. ERI-71133, July, 1971.

22. Liepmann, H. W. and Roshko, A., Elements of Gasdynamics, John Wiley and Sons, Inc., New York, 1957.
23. Kutler, P. and Lomax, H., A Systematic Development of the Supersonic Flow Fields Over and Behind Wings and Wing-Body Configurations Using a Shock-Capturing Finite-Difference Approach, American Institute of Aeronautics and Astronautics Paper No. 71-99, 1971, pp. 1-11.
24. Abbett, M. J., Boundary Condition Computational Procedures for Inviscid, Supersonic Steady Flow Field Calculations, Aerotherm Acurex Corporation, Mt. View, Calif., Aerotherm Report 71-41, Nov. 1971.
25. Ames Research Staff, Equations, Tables, and Charts for Compressible Flow, NACA Report 1135, National Advisory Committee for Aeronautics, 1953.
26. Ferri, A., Supersonic Flow around Circular Cones at Angles of Attack, NACA Technical Note 2236, National Advisory Committee for Aeronautics, 1950.
27. Babenko, K. I., Three-Dimensional Flow of Ideal Gas Past Smooth Bodies, National Aeronautics and Space Administration, Tech. Translation NASA TT F-380, 1966.
28. Davis, S. S., A Near- and Far-Field Analysis of the Sonic Boom Emitted by Nonlifting Rectangular Wings, Proceedings of the Third Conference on Sonic Boom Research, NASA Headquarters, 1970.

## ACKNOWLEDGMENTS

The author wishes to express his sincere gratitude to Dr. E. W. Anderson for his guidance and encouragement during my entire graduate study; to Dr. D. A. Anderson for his guidance, motivation and many helpful suggestions throughout my graduate school career; to Dr. Paul Kutler and Mr. Harvard Lomax for their creative suggestions; to Mrs. Anita Serovy for the typing of the manuscript; and to my wife, Arlene, for her patience and moral support throughout my graduate study.

Finally, the author would like to thank the National Aeronautics and Space Administration for the financial support during this study.

## APPENDIX A

## Eigenvalue Evaluation for Cartesian System

The stable range of mesh ratios contained in the finite difference equations can be theoretically predicted using amplification matrix theory. Application of this theory requires an evaluation of the eigenvalues associated with the coefficient matrices of the gas dynamic equations of motion.

Kutler<sup>(5)</sup> shows that the steady equations in a Cartesian frame can be written in the form

$$U_x + AU_y + BU_z + C = 0 \quad (A1)$$

where U represents a vector of state variables

$$U = \begin{pmatrix} u \\ v \\ w \\ p \\ \rho \end{pmatrix} \quad (A2)$$

and where A and B are square matrices given by

$$A = \begin{bmatrix} \frac{-uv}{c^2 - u^2} & \frac{c^2}{c^2 - u^2} & 0 & \frac{v}{\rho(c^2 - u^2)} & 0 \\ 0 & v/u & 0 & 1/\rho u & 0 \\ 0 & 0 & v/u & 0 & 0 \\ \frac{\rho v c^2}{c^2 - u^2} & \frac{-uc^2 \rho}{c^2 - u^2} & 0 & \frac{uv}{c^2 - u^2} & 0 \\ \frac{\rho v}{c^2 - u^2} & \frac{-u\rho}{c^2 - u^2} & 0 & \frac{v}{u(c^2 - u^2)} & v/u \end{bmatrix} \quad (A3)$$

$$B = \begin{bmatrix} \frac{-uw}{c^2 - u^2} & 0 & \frac{c^2}{c^2 - u^2} & \frac{w}{\rho(c^2 - u^2)} & 0 \\ 0 & w/u & 0 & 0 & 0 \\ 0 & 0 & w/u & 1/\rho u & 0 \\ \frac{\rho w c^2}{c^2 - u^2} & 0 & \frac{-c^2 u \rho}{c^2 - u^2} & \frac{-wu}{c^2 - u^2} & 0 \\ \frac{\rho w}{c^2 - u^2} & 0 & \frac{-u\rho}{c^2 - u^2} & \frac{-w}{u(c^2 - u^2)} & w/u \end{bmatrix} \quad (A4)$$

In the development of the matrices A and B the energy equation was used in the differential form

$$\bar{q} \cdot \left[ \nabla p - \left( \frac{\partial p}{\partial \rho} \right)_s \nabla \rho \right] = 0 \quad (A5)$$

For the A matrix, three of the eigenvalues are identical and given by

$$\lambda_{1, 2, 3} = v/u \quad (A6)$$

while the remaining two are given by

$$\lambda_{4, 5} = \frac{-uv \pm c \sqrt{u^2 + v^2 - c^2}}{u^2 - c^2} \quad (A7)$$

In a similar fashion, three of the eigenvalues of the B matrix are identical and given by

$$\lambda_{1, 2, 3} = w/u \quad (A8)$$

whereas the remaining two are given by

$$\lambda_{4, 5} = \frac{-uw \pm c \sqrt{u^2 + w^2 - c^2}}{u^2 - c^2} \quad (A9)$$

### Forebody Eigenvalues

The steady gas dynamic equations for the forebody wedge proper and the tip half-cone can be developed by a simple transformation of independent variables in Equations (A1) using the Jacobian elements in Table B2. In terms of the  $(\xi, \theta, \phi)$  system the equations become

$$\begin{aligned}
& U_{\xi} \xi_x + U_{\theta} \theta_x + U_{\phi} \phi_x \\
& + A (U_{\xi} \xi_y + U_{\theta} \theta_y + U_{\phi} \phi_y) \\
& + B (U_{\xi} \xi_z + U_{\theta} \theta_z + U_{\phi} \phi_z) + C = 0
\end{aligned} \tag{A10}$$

Substituting for the Jacobian elements yields a set of equations given by

$$U_{\xi} + A' U_{\theta} + B' U_{\phi} + C = 0 \tag{A11}$$

where, for the wedge proper

$$A' = \frac{A \cos^2 \theta}{\xi} - \frac{I \sin \theta \cos \theta}{\xi} \tag{A12}$$

$$B' = \frac{B \cos^2 \phi}{\xi} - \frac{I \sin \phi \cos \phi}{\xi} \tag{A13}$$

and for the tip half-cone

$$A' = \frac{A \cos^2 \theta \cos \phi}{\xi} + \frac{B \cos^2 \theta \sin \phi}{\xi} - \frac{I \sin \theta \cos \theta}{\xi} \tag{A14}$$

$$B' = \frac{B \cos \phi \cos \theta}{\xi} - \frac{A \sin \phi \cos \theta}{\xi} \tag{A15}$$

The matrix I is the identity matrix. In their fully expanded form showing all the elements the matrices defined by Equations (A12) - (A15) are presented on the following four pages, Equations (A12a) - (A15a).

Each of the four matrices contain at least one row or column in which all but one of the elements are zero. Hence, one of the eigenvalues in each matrix is immediately available. In all cases

A' =

$\frac{-\sin\theta\cos\theta}{\xi}$ $\frac{-uvcos^2\theta}{\xi(c^2-u^2)}$	$\frac{c^2\cos^2\theta}{\xi(c^2-u^2)}$	0	$\frac{vcos^2\theta}{\rho\xi(c^2-u^2)}$	0
0	$\frac{-\sin\theta\cos\theta}{\xi}$ $\frac{+vcos^2\theta}{\xi u}$	0	$\frac{cos^2\theta}{\rho\xi u}$	0
0	0	$\frac{-\sin\theta\cos\theta}{\xi}$ $\frac{+vcos^2\theta}{\xi u}$	0	0
$\frac{vc^2\cos^2\theta\rho}{\xi(c^2-u^2)}$	$\frac{-uc^2\cos^2\theta\rho}{\xi(c^2-u^2)}$	0	$\frac{-\sin\theta\cos\theta}{\xi}$ $\frac{+uvcos^2\theta}{\xi(c^2-u^2)}$	0
$\frac{vcos^2\theta\rho}{\xi(c^2-u^2)}$	$\frac{-ucos^2\theta\rho}{\xi(c^2-u^2)}$	0	$\frac{vcos^2\theta}{\xi u(c^2-u^2)}$	$\frac{-\sin\theta\cos\theta}{\xi}$ $\frac{+vcos^2\theta}{\xi u}$

(A12a)

B' =

$$\begin{array}{cccc}
 \frac{-\sin\theta\cos\theta}{\xi} & 0 & \frac{c^2\cos^2\theta}{\xi(c^2-u^2)} & \frac{w\cos^2\theta}{\rho\xi(c^2-u^2)} \\
 \frac{-u\cos^2\theta}{\xi(c^2-u^2)} & & & \\
 0 & \frac{-\sin\theta\cos\theta}{\xi} & 0 & 0 \\
 & \frac{+w\cos^2\theta}{\xi u} & & \\
 0 & 0 & \frac{-\sin\theta\cos\theta}{\xi} & \frac{\cos^2\theta}{\rho\xi u} \\
 & & \frac{+w\cos^2\theta}{\xi u} & \\
 \frac{w^2\cos^2\theta\rho}{\xi(c^2-u^2)} & 0 & \frac{c^2u\cos^2\theta\rho}{\xi(c^2-u^2)} & \frac{-\sin\theta\cos\theta}{\xi} \\
 & & \frac{-u\cos^2\theta}{\xi(c^2-u^2)} & 0 \\
 \frac{w\cos^2\theta\rho}{\xi(c^2-u^2)} & 0 & \frac{u\cos^2\theta\rho}{\xi(c^2-u^2)} & \frac{-\sin\theta\cos\theta}{\xi} \\
 & & \frac{-w\cos^2\theta}{\xi u(c^2-u^2)} & \frac{+w\cos^2\theta}{\xi u}
 \end{array}$$

(A13a)

A' =

$\frac{-\sin\theta\cos\theta}{\xi(c^2-u^2)}$	$\frac{c^2\cos^2\theta\cos\theta}{\xi(c^2-u^2)}$	$\frac{c^2\cos^2\theta\sin\theta}{\xi(c^2-u^2)}$	$\frac{v\cos^2\theta\cos\theta}{\rho\xi(c^2-u^2)}$	0
$\frac{-uvcos^2\theta\cos\theta}{\xi(c^2-u^2)}$	$\frac{-\sin\theta\cos\theta}{\xi}$		$\frac{+w\cos^2\theta\sin\theta}{\rho\xi(c^2-u^2)}$	
0	$\frac{+v\cos^2\theta\cos\theta}{\xi u}$	0	$\frac{\cos^2\theta\cos\theta}{\rho\xi u}$	0
	$\frac{+w\cos^2\theta\sin\theta}{\xi u}$			
0	0	$\frac{-\sin\theta\cos\theta}{\xi}$	$\frac{\cos^2\theta\sin\theta}{\rho\xi u}$	0
		$\frac{+v\cos^2\theta\cos\theta}{\xi u}$		
		$\frac{+w\cos^2\theta\sin\theta}{\xi u}$		
$\frac{\rho v c^2 \cos^2 \theta \cos \theta}{\xi(c^2-u^2)}$	$\frac{-\rho u c^2 \cos^2 \theta \cos \theta}{\xi(c^2-u^2)}$	$\frac{-\rho u c^2 \cos^2 \theta \sin \theta}{\xi(c^2-u^2)}$	$\frac{+uvcos^2\theta\cos\theta}{\xi(c^2-u^2)}$	0
$\frac{+\rho w c^2 \cos^2 \theta \sin \theta}{\xi(c^2-u^2)}$			$\frac{-uvcos^2\theta\sin\theta}{\xi(c^2-u^2)}$	
$\frac{\rho v \cos^2 \theta \cos \theta}{\xi(c^2-u^2)}$	$\frac{-\rho u \cos^2 \theta \cos \theta}{\xi(c^2-u^2)}$	$\frac{-\rho \cos^2 \theta \sin \theta}{\xi(c^2-u^2)}$	$\frac{v\cos^2\theta\cos\theta}{\xi u(c^2-u^2)}$	$\frac{-\sin\theta\cos\theta}{\xi}$
$\frac{+\rho w \cos^2 \theta \sin \theta}{\xi(c^2-u^2)}$			$\frac{+v\cos^2\theta\cos\theta}{\xi u}$	$\frac{+v\cos^2\theta\cos\theta}{\xi u}$
			$\frac{-w\cos^2\theta\sin\theta}{\xi u(c^2-u^2)}$	$\frac{+w\cos^2\theta\sin\theta}{\xi u}$

(A14a)

B' =

$\frac{-uwc\cos\theta\cos\phi}{\xi(c^2-u^2)}$	$\frac{-c^2\cos\theta\sin\phi}{\xi(c^2-u^2)}$	$\frac{c^2\cos\theta\cos\phi}{\xi(c^2-u^2)}$	$\frac{wc\cos\theta\cos\phi}{\rho\xi(c^2-u^2)}$	0
$\frac{+uvc\cos\theta\sin\phi}{\xi(c^2-u^2)}$	0	0	$\frac{-\cos\theta\sin\phi}{\rho\xi u}$	0
0	$\frac{-vc\cos\theta\sin\phi}{\xi u}$	$\frac{-vc\cos\theta\sin\phi}{\xi u}$	$\frac{\cos\theta\cos\phi}{\rho\xi u}$	0
0	0	$\frac{+wc\cos\theta\cos\phi}{\xi u}$	$\frac{\cos\theta\cos\phi}{\rho\xi u}$	0
$\frac{-\rho vc^2\cos\theta\sin\phi}{\xi(c^2-u^2)}$	$\frac{\rho uc^2\cos\theta\sin\phi}{\xi(c^2-u^2)}$	$\frac{-\rho uc^2\cos\theta\cos\phi}{\xi(c^2-u^2)}$	$\frac{-uvc\cos\theta\sin\phi}{\xi(c^2-u^2)}$	0
$\frac{+\rho wc^2\cos\theta\cos\phi}{\xi(c^2-u^2)}$			$\frac{-uwc\cos\theta\cos\phi}{\xi(c^2-u^2)}$	
$\frac{-\rho vc\cos\theta\sin\phi}{\xi(c^2-u^2)}$	$\frac{\rho uc\cos\theta\sin\phi}{\xi(c^2-u^2)}$	$\frac{-\rho uc\cos\theta\cos\phi}{\xi(c^2-u^2)}$	$\frac{-vc\cos\theta\sin\phi}{\xi(c^2-u^2)}$	$\frac{-vc\cos\theta\sin\phi}{\xi u}$
$\frac{+\rho wc\cos\theta\cos\phi}{\xi(c^2-u^2)}$			$\frac{-wc\cos\theta\cos\phi}{\xi(c^2-u^2)}$	$\frac{+wc\cos\theta\cos\phi}{\xi u}$

(A15a)

it can be shown that the first eigenvalue is a triple repeated eigenvalue. The remaining two eigenvalues are then determined by solving the appropriate quadratic expression.

For the wedge proper the eigenvalues of the  $A'$  matrix are given by Equations (A16) - (A17).

$$\lambda_{1, 2, 3} = \frac{-\sin\theta\cos\theta}{\xi} + \frac{v\cos^2\theta}{\xi} \quad (\text{A16})$$

$$\lambda_{4,5} = \frac{-\sin\theta\cos\theta}{\xi} \pm \frac{\cos^2\theta}{\xi(c^2-u^2)} \left[ u^2v^2 - c^2 + c^2u^2 - v^2c^2 \right]^{\frac{1}{2}} \quad (\text{A17})$$

For the  $B'$  matrix the eigenvalues are given by

$$\lambda_{1, 2, 3} = \frac{-\sin\phi\cos\phi}{\xi} + \frac{w\cos^2\phi}{\xi u} \quad (\text{A18})$$

$$\lambda_{4, 5} = \frac{-\sin\phi\cos\phi}{\xi} - \frac{uw\cos^2\phi}{\xi(c^2-u^2)} \pm \frac{c\cos^2\phi}{\xi(c^2-u^2)} \left[ u^2 - c^2 - w^2 \right]^{\frac{1}{2}} \quad (\text{A19})$$

For the tip half-cone the eigenvalues of the  $A'$  matrix are given by

$$\lambda_{1, 2, 3} = \frac{-\sin\theta\cos\theta}{\xi} + \frac{v\cos^2\theta\cos\phi}{\xi u} + \frac{w\cos^2\theta\sin\phi}{\xi u} \quad (\text{A20})$$

$$\lambda_{4, 5} = \frac{-\sin\theta\cos\theta(c^2-u^2) + uw(\cos^2\theta\sin\phi)}{\xi(c^2-u^2)} \pm \frac{c\cos^2\theta}{\xi(c^2-u^2)} \left[ \frac{u^2v^2}{c^2} \cos^2\phi + u^2 - c^2 + (v\cos\phi + w\sin\phi)^2 \right]^{\frac{1}{2}} \quad (\text{A21})$$

and for the B' matrix

$$\lambda_{1, 2, 3} = \frac{-v \cos \theta \sin \phi + w \cos \theta \cos \phi}{\xi u} \quad (\text{A22})$$

$$\lambda_{4, 5} = \frac{-uw \cos \theta \cos \phi}{\xi (c^2 - u^2)} \pm \frac{c \cos \theta}{\xi (c^2 - u^2)} \left[ u^2 - c^2 + \frac{v^2 u^2 \sin^2 \phi}{c^2} - \frac{u^2 w^2 \cos^2 \phi}{c^2} + (v \sin \phi w \cos \phi)^2 \right]^{\frac{1}{2}} \quad (\text{A23})$$

#### Afterbody Eigenvalues

For the afterbody, the transformed equations of motion using the Jacobian elements of Table B4 in the Cartesian equations of motion, Equations (A1), are given by

$$U_{\xi} + A' U_{\gamma} + B' U_{\phi} + C = 0 \quad (\text{A24})$$

Where for the wedge proper

$$A' = \frac{A \cos^2 \gamma}{\xi} - \frac{I \sin \gamma \cos \gamma}{\xi} \quad (\text{A25})$$

$$B' = \frac{B \cos^2 \phi}{\xi} - \frac{I \sin \phi \cos \phi}{\xi} \quad (\text{A26})$$

and for the tip half-cone

$$A' = \frac{A \cos^2 \gamma \cos \phi}{\xi} + \frac{B \cos^2 \gamma \sin \phi}{\xi} - \frac{I \sin \gamma \cos \gamma}{\xi} \quad (\text{A27})$$

$$B' = \frac{B \cos \phi}{\xi \tan \gamma + 2 \tan \theta_c} - \frac{A \sin \phi}{\xi \tan \gamma + 2 \tan \theta_c} \quad (\text{A28})$$

The  $A'$  and  $B'$  matrices for the afterbody wedge proper are the same as those for the forebody with the  $\gamma$  parameter replacing the  $\theta$  parameter. Hence, the matrices  $A'$  and  $B'$  for the afterbody are given by Equations (A12a) and (A13a) respectively and the resulting eigenvalues are given by Equations (A16) - (A19) with the  $\gamma$  parameter replacing the  $\theta$  parameter.

The fully expanded form of the  $A'$  and  $B'$  matrices for the tip half-cone, as defined in Equations (A27) and (A28), are given by Equations (A27a) and (A28a) on the following two pages. The matrices are similar to the corresponding matrices in the forebody region in that three of the  $A'$  eigenvalues for the tip cone, (A29), are triple repeated. The remaining two eigenvalues are given by Equation (A30). For the  $B'$  matrix the eigenvalues are given by Equations (A31) and (A32).

$$\lambda_{1, 2, 3} = \frac{-\sin\gamma \cos\gamma}{\xi} + \frac{v}{u} \frac{\cos^2\gamma \cos\phi}{\xi} + \frac{w}{u} \frac{\cos^2\gamma \sin\phi}{\xi} \quad (\text{A29})$$

$$\lambda_{4, 5} = \frac{-\sin \cos (c^2 - u^2) - uw \cos^2 \sin\phi}{\xi (c^2 - u^2)} \quad (\text{A30})$$

$$\pm \frac{\cos^2\gamma c \left[ v^2 \cos^2(u^2/c^2 + 1) + 2vw \cos\phi \sin\phi + w \sin\phi - c^2 + u^2 \right]^{1/2}}{\xi (c^2 - u^2)}$$

$$\lambda_{1, 2, 3} = \frac{-v \sin\phi}{u(\xi \tan\gamma + 2 \tan\theta_c)} + \frac{w \cos\phi}{u(\xi \tan\gamma + 2 \tan\theta_c)} \quad (\text{A31})$$

$$\lambda_{4, 5} = \frac{-uw \cos\phi \pm c \left[ (w \cos\phi - v \sin\phi)^2 - c^2 + u^2 + u^2 v^2 / c^2 \sin^2\phi \right]^{1/2}}{(c^2 - u^2)(\xi \tan\gamma + 2 \tan\theta_c)} \quad (\text{A32})$$

A' =

$\frac{-\sin\gamma \cos\gamma}{\xi(c^2-u^2)}$	$\frac{c^2 \cos^2\gamma \cos\phi}{\xi(c^2-u^2)}$	$\frac{c^2 \cos^2\gamma \sin\phi}{\xi(c^2-u^2)}$	$\frac{v \cos^2\gamma \cos\phi}{\rho \xi(c^2-u^2)}$	$\frac{+w \cos^2\gamma \sin\phi}{\rho \xi(c^2-u^2)}$	$0$
$0$	$\frac{-\sin\gamma \cos\gamma}{\xi u}$	$0$	$\frac{\cos^2\gamma \cos\phi}{\rho \xi u}$	$0$	$0$
$0$	$0$	$\frac{-\sin\gamma \cos\gamma}{\xi u}$	$\frac{+v \cos^2\gamma \cos\phi}{\xi u}$	$\frac{+w \cos^2\gamma \sin\phi}{\xi u}$	$0$
$\frac{+v c^2 \cos^2\gamma \cos\phi}{\xi(c^2-u^2)}$	$\frac{-\rho u c^2 \cos^2\gamma \cos\phi}{\xi(c^2-u^2)}$	$\frac{-\rho u c^2 \cos^2\gamma \sin\phi}{\xi(c^2-u^2)}$	$\frac{-\sin\gamma \cos\gamma}{\xi(c^2-u^2)}$	$\frac{+u v \cos^2\gamma \cos\phi}{\xi(c^2-u^2)}$	$0$
$\frac{+w c^2 \cos^2\gamma \sin\phi}{\xi(c^2-u^2)}$	$\frac{-\rho u \cos^2\gamma \cos\phi}{\xi(c^2-u^2)}$	$\frac{-\rho u \cos^2\gamma \sin\phi}{\xi(c^2-u^2)}$	$\frac{v \cos^2\gamma \cos\phi}{\xi u(c^2-u^2)}$	$\frac{-u w \cos^2\gamma \sin\phi}{\xi(c^2-u^2)}$	$\frac{-\sin\gamma \cos\gamma}{\xi u}$
$\frac{+w \cos^2\gamma \sin\phi}{\xi(c^2-u^2)}$	$\frac{-\rho u \cos^2\gamma \cos\phi}{\xi(c^2-u^2)}$	$\frac{-\rho u \cos^2\gamma \sin\phi}{\xi(c^2-u^2)}$	$\frac{v \cos^2\gamma \cos\phi}{\xi u(c^2-u^2)}$	$\frac{-w \cos^2\gamma \sin\phi}{\xi u(c^2-u^2)}$	$\frac{+v \cos^2\gamma \cos\phi}{\xi u}$
$\frac{+w \cos^2\gamma \sin\phi}{\xi(c^2-u^2)}$	$\frac{-\rho u \cos^2\gamma \cos\phi}{\xi(c^2-u^2)}$	$\frac{-\rho u \cos^2\gamma \sin\phi}{\xi(c^2-u^2)}$	$\frac{v \cos^2\gamma \cos\phi}{\xi u(c^2-u^2)}$	$\frac{-w \cos^2\gamma \sin\phi}{\xi u(c^2-u^2)}$	$\frac{+w \cos^2\gamma \sin\phi}{\xi u}$

(A27a)

B' =

$\frac{uv \sin \theta}{\mu(c^2 - u^2)}$	$\frac{-c^2 \sin \theta}{\mu(c^2 - u^2)}$	$\frac{c^2 \cos \theta}{\mu(c^2 - u^2)}$	$\frac{-v \sin \theta}{\mu(c^2 - u^2) \rho}$	0
$\frac{-uw \cos \theta}{\mu(c^2 - u^2)}$			$\frac{+w \cos \theta}{\mu(c^2 - u^2) \rho}$	
0	$\frac{-v \sin \theta}{\mu + w \cos \theta}$	0	$\frac{-\sin \theta}{\mu u \rho}$	0
0	0	$\frac{-v \sin \theta}{\mu u + w \cos \theta}$	$\frac{\cos \theta}{\mu u \rho}$	0
$\frac{-\rho v c^2 \sin \theta}{\mu(c^2 - u^2)}$	$\frac{\rho u c^2 \sin \theta}{\mu(c^2 - u^2)}$	$\frac{-\rho c^2 u \cos \theta}{\mu(c^2 - u^2)}$	$\frac{-u v \sin \theta}{\mu(c^2 - u^2)}$	0
$\frac{+\rho w c^2 \cos \theta}{\mu(c^2 - u^2)}$			$\frac{-u w \cos \theta}{\mu(c^2 - u^2)}$	
$\frac{-\rho v \sin \theta}{\mu(c^2 - u^2)}$	$\frac{\rho u \sin \theta}{\mu(c^2 - u^2)}$	$\frac{-\rho u \cos \theta}{\mu(c^2 - u^2)}$	$\frac{-v \sin \theta}{\mu u (c^2 - u^2)}$	$\frac{-v \sin \theta}{\mu u + w \cos \theta}$
$\frac{+\rho w \cos \theta}{\mu(c^2 - u^2)}$			$\frac{-w \cos \theta}{\mu u (c^2 - u^2)}$	$\frac{\mu u}{\mu u}$

$$\mu = \tan \theta + 2 \tan \theta_c$$

(A28a)

## APPENDIX B - FLOW EQUATION TRANSFORMATIONS

## Introduction

Integration of the equations of motion via MacCormack's technique requires that the equations be cast in a conservative form using the independent variables associated with the various coordinate systems describing the body and flow field. Hence, the Cartesian conservative form presented in Equations (37) must be transformed in Regions I and II to the various systems defining the forebody and afterbody. The Jacobian elements of the transformations as well as the transformed equations of motion and resulting conservative forms are presented in subsequent sections.

## Forebody Equations of Motion

The coordinate systems used to describe the forebody are given in Figures 21 and 22. Although the coordinate labels ( $\xi, \phi, \theta$ ) are identical their definitions are, in general, different.

In the Cartesian system it has been shown that the equations of motion can be written in the form

$$\bar{E}_x + \bar{F}_y + \bar{G}_z = 0 \quad (B1)$$

where the vector conservative variables  $\bar{E}$ ,  $\bar{F}$ , and  $\bar{G}$  are given by Equations (39), (40) and (41). Noting that

$$\begin{aligned}
 x &= x(\xi, \phi, \theta) \\
 y &= y(\xi, \phi, \theta) \\
 z &= z(\xi, \phi, \theta)
 \end{aligned}
 \tag{B2}$$

the equations of motion (A1) can be written as

$$\begin{aligned}
 \bar{E} \xi_x + \bar{E}_\phi \phi_x + \bar{E}_\theta \theta_x \\
 + \bar{F} \xi_y + \bar{F}_\phi \phi_y + \bar{F}_\theta \theta_y \\
 + \bar{G} \xi_z + \bar{G}_\phi \phi_z + \bar{G}_\theta \theta_z = 0
 \end{aligned}
 \tag{B3}$$

where the terms  $\xi_x, \xi_y, \xi_z, \phi_x, \phi_y, \phi_z, \theta_x, \theta_y,$  and  $\theta_z$  represent the Jacobian elements of the transformation.

The transformation equations for the wedge proper and the half-cone are given in Table B1. The resulting Jacobian elements are given in Table B2.

Substitution of the Jacobian elements of Table B2 into Equations (A1) yields for the wedge proper

$$\begin{aligned}
 \left[ \xi \bar{E} \right]_\xi + \left[ -\sin\theta \cos\theta \bar{E} + \cos^2\theta \bar{F} \right]_\theta \\
 + \left[ -\sin\phi \cos\phi \bar{E} + \cos^2\phi \bar{G} \right]_\phi \\
 + \left[ (-\sin^2\theta - \sin^2\phi + \cos^2\phi) \bar{E} + 2\sin\theta \cos\theta \bar{F} + 2\sin\phi \cos\phi \bar{G} \right] = 0
 \end{aligned}
 \tag{B4}$$

and for the half-cone

$$\begin{aligned}
 & \left[ \xi \tan \theta \bar{E} \right]_{\xi} + \left[ -\bar{E} \sin^2 \theta + \bar{F} \sin \theta \cos \phi + \bar{G} \sin \theta \cos \theta \sin \phi \right]_{\theta} \\
 & + \left[ -\bar{F} \sin \phi + \bar{G} \cos \phi \right]_{\phi} \quad (B5) \\
 & + \left[ (2 \sin \theta \cos \theta - \tan \theta) \bar{E} + 2 \bar{F} \cos \phi \sin^2 \theta + 2 \bar{G} \sin^2 \theta \sin \phi \right] = 0
 \end{aligned}$$

Equations (B4) and (B5) represent the conservative form of the equations of motion in the forebody region.

Table B1. Forebody transformation equations

	Wedge proper	Half-cone
$\xi$	x	x
$\phi$	$\tan^{-1} z/x$	$\tan^{-1} z/y$
$\theta$	$\tan^{-1} y/x$	$\tan^{-1} \frac{\sqrt{y^2+z^2}}{x}$

Table B2. Jacobian elements for forebody transformation

	Wedge proper	Half-cone
$\xi_x$	1	1
$\xi_y$	0	0
$\xi_z$	0	0
$\theta_x$	$\frac{-\sin\theta\cos\theta}{\xi}$	0
$\theta_y$	0	$\frac{-\sin\theta\cos\theta}{\xi}$
$\theta_z$	$\frac{\cos^2\theta}{\xi}$	$\frac{\cos\theta\cos\theta}{\xi}$
$\theta_x$	$\frac{-\sin\theta\cos\theta}{\xi}$	$\frac{-\sin\theta\cos\theta}{\xi}$
$\theta_y$	$\frac{\cos^2\theta}{\xi}$	$\frac{\cos^2\theta\cos\theta}{\xi}$
$\theta_z$	0	$\frac{\cos^2\theta\sin\theta}{\xi}$

## Afterbody Equations of Motion

The coordinate systems used to describe the afterbody are given in Figures 38 and 39. The equations of motion in the Cartesian form are given by Equation (B1) and in the  $(\xi, \phi, \gamma)$  system by Equation (B3) with the  $\theta$  variable replaced by the variable. The transformation equations

$$\begin{aligned} x &= x(\xi, \phi, \gamma) \\ y &= y(\xi, \phi, \gamma) \\ z &= z(\xi, \phi, \gamma) \end{aligned} \tag{B6}$$

are given in Table B3 for the wedge proper and the tip half-cone with the resulting Jacobian elements  $\xi_x, \xi_y, \xi_z, \phi_x, \phi_y, \phi_z, \gamma_x, \gamma_y,$  and  $\gamma_z$  given in Table B4.

Table B3. Coordinate transformation equations for the afterbody region equations of motion

	Wedge proper	Half-cone
$\xi$	$x$	$x$
$\phi$	$\tan^{-1}(z/x)$	$\tan^{-1}(z/y)$
$\gamma$	$\tan^{-1}\left[\frac{y-2\tan\theta_w}{\sqrt{x^2-z^2}}\right]$	$\tan^{-1}\left[\frac{y^2+z^2-2\tan\theta_c}{x}\right]$

Table B4. Jacobian elements for the afterbody transformation

	Wedge proper	Half-cone
$\xi_x$	1	1
$\xi_y$	0	0
$\xi_z$	0	0
$\phi_x$	$\frac{-\sin\phi\cos\phi}{\xi}$	0
$\phi_y$	0	$\frac{-\sin\phi}{\xi\tan\gamma + 2\tan\theta_c}$
$\phi_z$	$\frac{\cos^2\phi}{\xi}$	$\frac{\cos\phi}{\xi\tan\gamma + 2\tan\theta_c}$
$\gamma_x$	$\frac{-\cos\gamma\sin\gamma}{\xi}$	$\frac{-\sin\gamma\cos\gamma}{\xi}$
$\gamma_y$	$\frac{\cos^2\gamma}{\xi}$	$\frac{\cos^2\gamma\cos\phi}{\xi}$
$\gamma_z$	0	$\frac{\cos^2\gamma\sin\phi}{\xi}$

Substitution of the Jacobian elements of Table B4 into Equations (A1) yields for the afterbody wedge proper

$$\begin{aligned}
 & \left[ \begin{array}{c} \xi \\ \bar{E} \end{array} \right]_{\xi} + \left[ \begin{array}{c} -\sin\phi\cos\phi\bar{E} + \cos^2\phi\bar{G} \end{array} \right]_{\phi} \\
 & + \left[ \begin{array}{c} -\sin\gamma\cos\gamma\bar{E} + \cos^2\gamma\bar{F} \end{array} \right]_{\gamma} + \left[ \begin{array}{c} -2\sin^2\phi\bar{E} \\ -\sin^2\gamma\bar{E} + \cos^2\gamma\bar{E} + 2\sin\phi\cos\phi\bar{G} + 2\sin\gamma\cos\gamma\bar{F} \end{array} \right] = 0
 \end{aligned} \tag{B7}$$

and for the tip half-cone

$$\begin{aligned}
 & \left[ \begin{array}{c} (\xi\tan\gamma + 2\tan\theta_c)\bar{E} \end{array} \right]_{\xi} \\
 & + \left[ \begin{array}{c} -\sin\gamma\cos\gamma\bar{E} + \cos^2\gamma(\cos\phi\bar{F} + \sin\phi\bar{G}) \end{array} \right]_{\gamma} \left( \tan\gamma + \frac{2\tan\theta_c}{\xi} \right) \\
 & + \left[ \begin{array}{c} -\bar{F}\sin\phi + \bar{G}\cos\phi \end{array} \right]_{\phi} \\
 & - \left( \tan\gamma + \frac{2\tan\theta_c}{\xi} \right) \left[ \begin{array}{c} (1-2\cos^2\gamma)\bar{E} - 2\cos\gamma\sin\gamma(\cos\phi\bar{F} + \sin\phi\bar{G}) \end{array} \right] = 0
 \end{aligned} \tag{B8}$$